Alma Mater Studiorum · University of Bologna

School of Science
Department of Physics and Astronomy 'Augusto Righi'
Master Degree in Astrophysics and Cosmology

N-body simulations of the Sextans dwarf spheroidal galaxy: accretion at small scales?

Supervisor:

Prof. Carlo Nipoti

Co-supervisors:

Dr. Raffaele Pascale
Dr. Giuseppina Battaglia

Submitted by:

Morgana Maria Elena Pederzoli

Academic Year 2023/2024

Abstract

In this thesis I produce models based on N-body simulations of the dwarf spheroidal galaxy Sexants, which exhibits a peculiar ring-like feature in its line-of-sight (l.o.s.) velocity and pseudo-equivalent widths of the Mg-triplet absorption feature distributions, as identified by Cicuéndez and Battaglia (2018) using spectroscopic data. Cicuéndez and Battaglia (2018) suggested that these anomalies may be attributed to the accretion of a smaller satellite system, prompting us to conduct N-body simulations to test this hypothesis. The project comprises three main components: the development of a Python software to generate initial conditions (ICs) for the simulations, the execution of simulations under two scenarios (one with a satellite composed only of stars and another satellite composed also of dark matter (DM) halo), and the creation of mock datasets for comparison with observational data.

Sextans is modelled with two components—stars and a DM halo—based on literature values. When the satellite is only composed of stars, it is intended to represent a sort of disrupted nuclear star cluster, when it is composed also of DM it is intended to mirror a dwarf satellite galaxy. The simulations are run using the state-of-the-art hydrodynamical N-body code Arepo, exploring different sets of orbital ICs.

The results show that, for a satellite initially set in the outskirts of the galaxy, only the simulations involving a satellite with a DM halo successfully replicate, at the same time, the observed ring-like structure and peculiar kinematics in the velocity map. In contrast, simulations without DM failed to reproduce the observed structures. These findings support the hierarchical merging theory at the scale of dwarf galaxies, suggesting that the peculiar features of Sextans can indeed be attributed to an accretion of a smaller system.

Contents

Introduction

The current cosmological framework suggests that galaxies form in part through the accretion and merging of smaller systems. This mechanism is believed to operate at all scales, including those of dwarf galaxies (DGs), which are typically satellites of larger galaxies such as the Milky Way and M31. For this reason, DGs play a crucial role to our understanding of both galaxy formation and small-scale cosmology.

In this thesis, I study the case of Sextans, a local dwarf spheroidal galaxy (dSph), where Cicuéndez and Battaglia (2018) uncovered a peculiar ring-like feature in both spatial distributions of line-of-sight (l.o.s.) heliocentric velocities and pseudo-equivalent widths of the Mg-triplet absorption feature (ΣMg), primarily using spectroscopic data from Walker et al. (2009b). By means of N-body simulations, the aim of this thesis is to investigate whether the observed peculiar ring-like velocity feature can be a signature of a merger between Sextans and a much smaller satellite.

The thesis is organised as follows.

In chapter §§ 1, I will present an introduction to DGs, discussing their importance in the context of galaxy formation and evolution. After illustrating the various types of DGs, the chapter will primarily focus on dSphs, including Sextans. I will discuss their defining properties, such as low luminosity, stellar populations, dark matter (DM) content and lack of gas. I will conclude by illustrating how the current cosmological model is encountering problems at the scales of DGs.

Chapter §§ 2 will focus specifically on the Sextans dwarf spheroidal galaxy. I will present a detailed analysis of its morphological and kinematic properties, including its stellar distribution, chemical composition, and dynamics. This chapter will explore the observational evidence supporting the presence of disturbances and possible traces of minor merger events. Special attention will be given to the peculiar ring-like feature identified by Cicuéndez and Battaglia (2018), and the presence of a possible relic star cluster by Kim et al. (2019). These observations motivate the simulation work presented in the subsequent chapters.

In chapter §§ 3, I will introduce the theoretical framework of collisionless systems, which is used to model the dynamical interactions within galaxies. This chapter will delve into the fundamental concept of the distribution function (DF), highlighting its role in relation to observables and its connection to key equations like the collisionless Boltzmann and Jeans equations. A particular focus will be placed on deriving the functional form of the DF under conditions of spherical symmetry, isotropy and steady-state, resulting in the Eddington formula. This formula will play a crucial role in constructing physically motivated N-body models, which are central to the presented simulations in this thesis.

All the simulations are conducted using the N-body code Arepo (Springel, 2010; Weinberger et al., 2020), a state-of-the-art code widely applied across various astrophysical problems. Therefore, in chapter §§ 4, I will detail the characteristics of Arepo, its core

algorithms, features, and the significant advantages it offers for simulating complex systems. Additionally, I will outline the methodologies I used to develop a custom Python software for generating N-body realisations for the simulations, i.e. samples of particles with known positions, velocities, and masses, of equilibrium stellar systems to model Sextans and its satellite. In all the simulations presented, Sextans is represented by two components: stars that follow a Plummer (1911) profile and the DM halo that follows a truncated (Navarro et al., 1996, NFW) profile. The structural parameters, masses and scale radii are chosen according to the literature (Cicuéndez et al., 2018; Battaglia et al., 2011).

In the following chapters, I will analyse the outcomes of the various simulations exploring two distinct families of scenarios, depending of whether the satellite possessed or not a DM halo.

In chapter §§ 5 I will analyse the simulations in which the satellite is only made of stars, but no DM, which is intended to reproduce a globular cluster or a nuclear star cluster originally belonging to a now disrupted galaxy. In this case, the satellite is modelled following a Plummer profile. In chapter §§ 6, I will analyse the simulations in which the satellite is embedded in a dominant DM halo, which is intended to resemble an interacting dwarf satellite galaxy. In this case, the satellite is a scaled-down version of Sextans, a stellar Plummer population embedded in a dominant NFW DM halo. In both cases, I will explore different sets of initial conditions (ICs) for the satellite system, mainly aiming to replicate the observed l.o.s. velocity map. The latter is, indeed, the most critical feature to reproduce, because it depends on both the orientation of the galaxy and particle velocities. I will then create several mock datasets of positions on the plane of the sky and l.o.s. velocities from the simulations to be compared with the observed data of Cicuéndez and Battaglia (2018), in order to find the best configuration.

In summary, this thesis investigates the possibility that Sextans' peculiar l.o.s. velocity structure could result from an accretion event involving a smaller satellite.

I

Dwarf Spheroidal Galaxies

Dwarf spheroidal galaxies are known to be satellites of both the Milky Way and M31, the nearest major galaxy in the Local Group.
In this chapter, it will be introduced the concept of dwarf galaxies and how they have been categorised in the Local Group based on their luminosity and gas content. The chapter will then focus on the main properties of the gas-poor ones, the so-called dwarf spheroidals, describing their morphology (§ 1.2), kinematics (§ 1.3), mass content (§ 1.4) and possible evolution scenarios (§ 1.5). In the last section (§ 1.6) dwarf galaxies will be discussed in a cosmological context, focusing on the current issues with the standard model at such small scales.

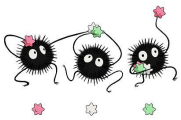

1.1 General properties of dwarf galaxies

Studies of the galaxy luminosity function (Binggeli et al., 1988) agree that the majority of the galaxies in the Universe are dwarfs, i.e. systems at least one order of magnitude fainter than the Milky Way (MW). This is also true in the Local Group (LG) where all galaxies, aside from the MW, M31, M32 and M33, are indeed dwarf galaxies (DGs), with the majority of them being satellites of the MW and M31.

Currently, DGs are one of the best probes for studying DM halos as they exhibit the largest dynamical mass-to-light ratio M/L, reaching even values of 1000 for some of the faintest systems. Also, DGs are still crucial to test the standard cosmological framework. The dark energy plus cold dark matter (ΛCDM) cosmological model has successfully predicted the large-scale structure formation, but on scales smaller than $\approx$1 Mpc and masses lower than $\approx 10^{11}\,M_{\odot}$ the theory is in tension with some observations. Some of the most discussed problems are the core-cusp, missing satellite and too-big-to-fail problems (Bullock and Boylan-Kolchin, 2017, see § 1.6 for a more detailed discussion). Moreover, in the ΛCDM paradigm, MW-like and massive galaxies are formed in a hierarchical process through mergers and accretion of smaller systems, but this process is thought to occur at all scales (Fakhouri et al., 2010), including those of DGs. Thus, any evidence of accretion in DGs is an important probe for galaxy formation theories.

DGs cover a wide range of different types of galaxies. Among them, the dwarf ellipticals (dEs) have properties closest to those of early-type galaxies (ETGs), while the other ones can be distinguished on the basis of their gas content. The gas-rich ones are called dwarf irregulars (dIrrs), while the gas-poor ones, adopting the nomenclature of Simon (2019), are called either dwarf spheroidals (dSphs) or ultra-faint dwarfs (UFDs), depending on whether they are brighter or fainter than absolute V-band magnitude $M_V = -7.7$, respectively. (Putman et al., 2021, and reference there in) showed that these two types of dwarfs are not randomly distributed with respect to the main galaxies. In particular, the gas-rich satellites are mostly segregated outside the virial radius of the main galaxy. This strongly suggests that the LG medium is responsible for stripping gas in DGs and quenching their star formation (Fillingham et al., 2015, 2016, 2018)

For historical reasons, all DGs discovered before the Sloan Digital Sky Survey (SDSS) are called classical DGs. In particular, in the case of dSphs the ones referred to classical are Sculptor, Fornax, Leo I, Leo II, Carina, Ursa Minor, Sextans and Draco. As the most luminous of these fainter and closer objects, these classical dwarfs have been extensively studied over the years. Some of their most significant parameters are reported in Tab. 1.1.

1.2 Morphological properties

Since the first studies by Hodge in the 1960s (Hodge, 1961, 1964, and references therein), two structural features have been found to be common to all classical dSphs.

First, they all appear to have a flattened morphology on the plane of the sky. This

Name	Distance [kpc]	R_e [pc]	$\log L$ [$L_\odot$]	$\log M_{dyn}(R_e)$ $M_\odot$	ϵ	$\overline{\sigma}_{los}$ [km s^{-1}]
Carina	105^{+6}_{-6}	313^{+3}_{-3}	$5.70^{+0.02}_{-0.02}$	$7.01^{+0.14}_{-0.17}$	0.4	$6.6^{+1.2}_{-1.2}$
Draco	76^{+6}_{-6}	225^{+2}_{-2}	$5.42^{+0.02}_{-0.02}$	$7.15^{+0.03}_{-0.03}$	0.3	$9.0^{+0.3}_{-0.3}$
Fornax	147^{+12}_{-12}	749^{+4}_{-4}	$7.32^{+0.06}_{-0.06}$	$7.88^{+0.03}_{-0.03}$	0.3	$11.4^{+0.4}_{-0.4}$
Leo I	254^{+15}_{-15}	276^{+2}_{-2}	$6.64^{+0.11}_{-0.11}$	$7.26^{+0.04}_{-0.04}$	0.3	$9.2^{+0.4}_{-0.4}$
Leo II	233^{+14}_{-14}	155^{+1}_{-1}	$5.83^{+0.02}_{-0.02}$	$6.88^{+0.04}_{-0.05}$	0.1	$7.4^{+0.4}_{-0.4}$
Sculptor	86^{+6}_{-6}	303^{+4}_{-4}	$6.26^{+0.06}_{-0.06}$	$7.36^{+0.03}_{-0.03}$	0.4	$10.1^{+0.3}_{-0.3}$
Sextans	86^{+4}_{-4}	527^{+17}_{-14}	$5.51^{+0.04}_{-0.04}$	$7.47^{+0.04}_{-0.04}$	0.3	$8.4^{+0.4}_{-0.4}$
Ursa Minor	76^{+3}_{-3}	403^{+2}_{-2}	$5.54^{+0.02}_{-0.02}$	$7.21^{+0.03}_{-0.03}$	0.6	$8.0^{+0.3}_{-0.3}$

Tab. 1.1 – Heliocentric distance; projected half-light radius R_e; total V-band luminosity L; dynamical mass $M_{dyn}(R_e)$; ellipticity ϵ; mean l.o.s. velocity dispersion $\overline{\sigma}_{los}$. For each of the 8 classical dSphs. Data from Battaglia and Nipoti (2022) and McConnachie (2012).

can be quantified by the ellipticity parameter ϵ, defined as

$$\epsilon \equiv 1 - \frac{b}{a}, \tag{1.1}$$

where a and b are the projected semi-major and semi-minor axis, respectively. The isophotes of all dSphs show $0.1 \leq \epsilon \leq 0.7$.

Second, the dSphs projected stellar density profile declines more steeply at large radii than the typical ETGs. As resolved systems, the projected stellar density profiles in dSphs are produced by creating circular or elliptical bins on the plane of the sky and counting the stars that fall into each bin. Thus, under the assumption that the stars number density distribution traces linearly the luminosity distribution, for dSphs one can unambiguously refer to stellar number density profiles or projected luminosity profiles. The luminosity profile of ETGs is typically well fitted by the de Vaucouleurs (1948) model, or the more general Sérsic (1963) profile:

$$I(R) = I_e \exp\left\{-b(n)\left[\left(\frac{R}{R_e}\right)^{1/n} - 1\right]\right\}, \tag{1.2}$$

where R is the distance on the plane of the sky from the centre of the system, R_e is the projected half-light radius, I_e is the surface brightness at R_e, n is the Sérsic index and $b(n)$ is a dimensionless parameter. Ciotti and Bertin (1999) showed that it can be approximated to:

$$b(n) = 2n - \frac{1}{3} + \frac{4}{405n} + \frac{46}{25515n^2} + \frac{131}{1148175n^3} - \frac{2194697}{30690717750n^4} + \mathcal{O}(n^{-5}). \tag{1.3}$$

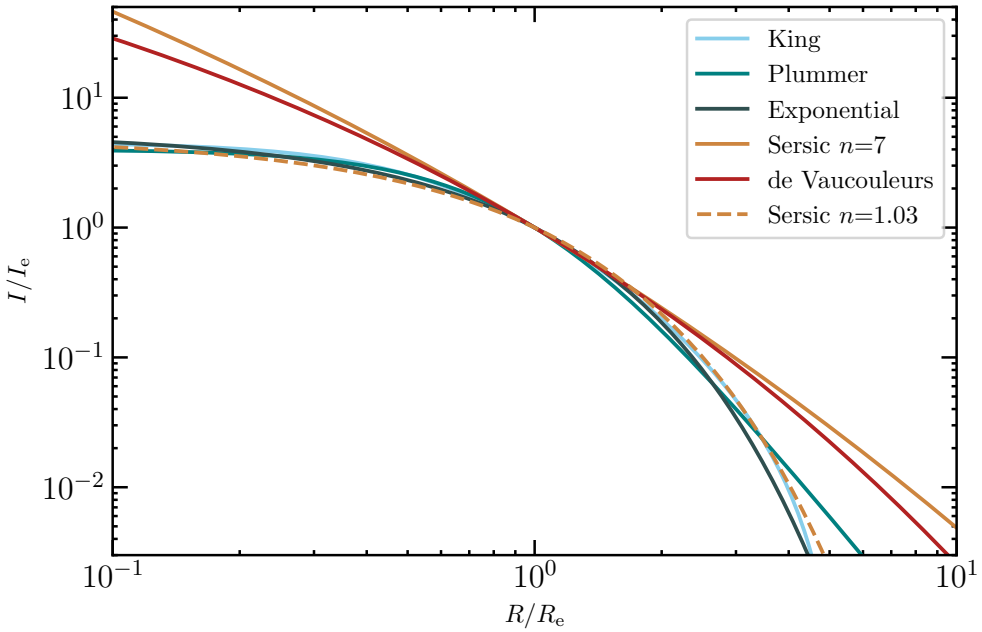

Fig. 1.1 – Several surface brightness profiles as a function of the distance from the centre rescaled to the half-light radius R_e. The profiles are scaled to the surface brightness at the half-light radius I_e. In different colours are the different models mentioned in § 1.2, parameters values have been taken from Cicuéndez et al. (2018).

Notably, for $n = 1$ the Sérsic profile reduces to the exponential one, which is most commonly used in terms of the central surface brightness I_0:

$$I(R) = I_0 \exp\left(-\frac{R}{R_{\rm exp}}\right), \tag{1.4}$$

where $R_{\rm exp} \approx R_e/1.68$.

For ETGs the Sérsic index is typically $2 < n < 10$, but dSphs require models with a cored central profile and a steeper outer profile. Therefore, the models better suited to fit the profile of dSphs are Sérsic profiles with $n < 2$ or the King (1962) analytic profile:

$$I(R) = I_0 \left[\frac{1}{\sqrt{1+(R/R_c)^2}} - \frac{1}{\sqrt{1+(R_t/R_c)^2}}\right]^2, \tag{1.5}$$

where I_0 is a characteristic surface brightness, R is the projected radius, R_c the core radius and R_t the truncation radius. The latter is the limiting radius of the system that one might expect from tidal truncation, i.e. where the density formally drops to zero. Another commonly used cored profile for dSphs is the Plummer (1911) profile,

$$I(R) = \frac{I_0}{\left[1+\left(\frac{R}{R_s}\right)^2\right]^2}, \tag{1.6}$$

widely adopted in the literature to model the distribution of stars in these galaxies due to its simplicity and analytical tractability.

Figure 1.1 presents the luminosity profiles, rescaled by I_e, for the different models mentioned in this section. The plot highlights the different shapes of the two classes of models: King, Plummer, Exponential and Sérsic $n = 1.03$ (so $n < 2$) profiles are cored in the inner region and steeper at the outer radii, Sérsic $n = 7$ and de Vaucouleurs ($n > 2$), instead are cuspier in the inner regions and shallower at greater radii.

1.3 Kinematic properties

Due to the paucity of gas, stars are the only tracers of the gravitational potential in dSphs and UFDs, and a comprehensive understanding of the dynamical properties of the galaxy would require the 6D phase space data for a large number of stars. In practice, even for the most precise distance indicators, as in Muraveva et al. (2020), the relative precision in the depth for individual stars is still of the order of the size of the galaxy itself. Consequently, the only quantities available are the two components of the position vector on the plane of the sky, and the three components of the velocity vector, i.e. one l.o.s. velocity and two proper motions. The advent of *Gaia* DR1 (Gaia Collaboration et al., 2016, Gaia collaboration,) and DR2 (Gaia collaboration, Brown et al., 2018) increased sensibly the amount of stars with measured proper motions. Moreover, by combining *Gaia* DR1 and DR1 with Hubble Space telescope measurements, it was possible to obtain the first three-dimensional internal motions for individual stars in Sculptor (Massari et al., 2018) and Draco (Massari et al., 2020). However, in most of the cases, transverse velocities uncertainties are still at least one order of magnitude larger than those of the l.o.s. component (Battaglia and Nipoti, 2022). Consequently, the dynamical modelling still mostly relies on the latter.

The search for velocity gradients has a long-standing history, as they can arise from a variety of reasons such as intrinsic rotation, streaming motions and tidal disruption, each providing information on the formation and evolution of the system. From observations (for example Battaglia et al., 2008; Fraternali et al., 2009; Wheeler et al., 2017; Kirby et al., 2014; Walker et al., 2008), it can be seen that the majority of DGs do not display evidence of ordered motion. Even when statistically significant velocity gradients can be identified, these appear to be sub-dominant in comparison to the influence of random motions (Wheeler et al., 2017), which are quantified by the l.o.s. velocity dispersion $\sigma_{\rm los}$. As I will discuss in § 3.3, dSphs are pressure-supported systems, meaning that, for these systems, the quantity $\rho\sigma^2$ can be interpreted as a pressure acting against the gravitational forces, where ρ is the local three-dimensional density and σ the velocity dispersion.

For most of the dwarfs in the LG, only the central value of the l.o.s. velocity dispersion, σ_0, is available, while for classical dwarf $\sigma_{\rm los}$ can be studied as a function of projected radius R, allowing the derivation of the l.o.s. velocity dispersion profile. As illustrated in Figure 1.2, the l.o.s. velocity dispersion profiles for the classical dSphs exhibit a relatively flat or slightly increasing trend, with typical values ranging between 5 and 15 km s^{-1}, as it can be seen in the last column of Tab. 1.1.

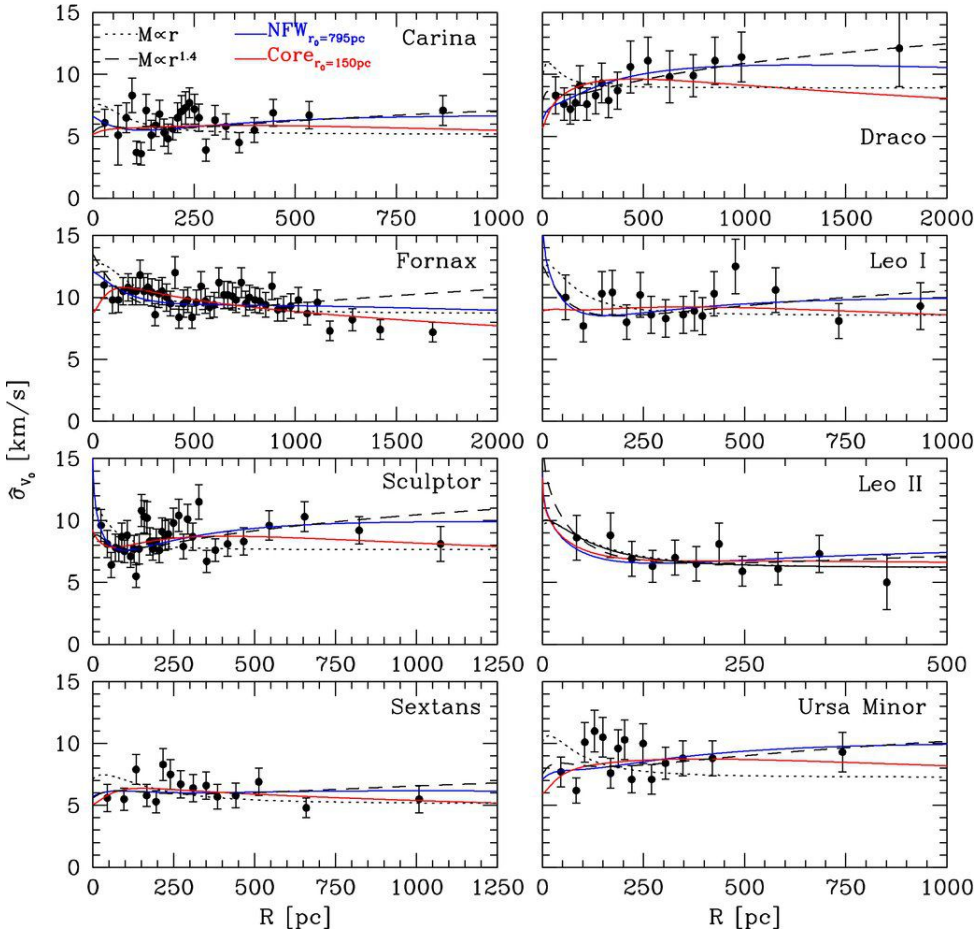

Fig. 1.2 – Projected l.o.s. velocity dispersion profiles for eight of the classical MW dSphs (circles with errorbars). The lines are the fitted profiles calculated for different models. Picture taken from Walker et al. (2009a)

.

Measurements of the l.o.s. velocity dispersion are extremely important, as they provide an indication of the dynamical mass. Indeed, under the assumption of equilibrium and using the virial theorem, $\sigma^2 \propto GM/R$ for relaxed systems with a characteristic size R. As a consequence, the flat profiles visible in Figure 1.2 fit quite well with those of an almost isothermal distribution (dotted line, $M \propto r$). However, the luminous mass is not sufficient to justify the flatness of these curves, indicating that dSphs are necessarily heavily DM-dominated. I will discuss the DM content of dSphs in more detail in the next section.

Being satellites of the MW, the equilibrium assumption is actually non-trivial. Indeed, all classical dSphs orbit within the MW gravitational potential, hence they are susceptible to several phenomena due to tidal forces. Some studies, such as Read et al. (2006), have investigated whether the effects of such external forces can substantially alter the velocity dispersion. Their results showed that tidal forces can indeed alter the velocity dispersion of stars, but this effect is only significant in the outer regions of the DG or if the galaxy is on a particularly disruptive orbit, e.g. passing close to the MW during pericentric passages. For dSphs that are on relatively mild orbits, tidal forces are unlikely to significantly alter the central velocity dispersion, which is more robust and less sensitive

to tidal effects. Moreover, works like Battaglia et al. (2015) showed that the observable properties of Fornax are not significantly influenced by tidal effects, confirming that tidal forces become relevant primarily for dSphs with orbits with small pericentric distances and high orbital eccentricities. In addition to this, Iorio et al. (2019) brought evidence that, for the Sculptor dSph, even in case of non-negligible tidal effects on its DM halo, the stellar kinematics still represents a robust tracer of the internal dynamics.

1.4 Mass content

One of the main goals of studying the stellar dynamics of DGs is to determine the mass density profile ρ of their DM halos. This, in principle, requires an estimate of the galaxy gravitational potential Φ, which can be inferred from the kinematics of the stars via dynamical models. In fact, by assuming that the galaxy is isolated and stationary, the gravitational potential is directly related to the matter density via the Poisson equation $\boldsymbol{\nabla}^2\Phi_{\rm tot} = 4\pi G\rho_{\rm tot}$.

Apart from being assumed to be stationary, dSphs are modelled as collisionless stellar systems, in which two-body interactions between individual components are negligible with respect to the mean gravitational field. The hypothesis of non-collisionality is justified by the high relaxation time, which measures the average time for a star's velocity to be significantly altered by interactions with other stars. In dSphs, this time is extremely long due to their low stellar density, meaning that stars rarely interact directly, making them effectively collisionless systems. For stationary collisionless systems, the structural and kinematic properties of the galaxy can be calculated from its distribution function $f(\boldsymbol{x}, \boldsymbol{v}, t)$, which quantifies the probability of finding a star within a given volume of the phase space centred at $(\boldsymbol{x}, \boldsymbol{v})$ at time t, (Binney and Tremaine, 2008). A more detailed analysis of this topic will be provided in §§ 3.

Nevertheless, it is practically impossible to directly infer $f(\boldsymbol{x}, \boldsymbol{v}, t)$ from data, as it is necessary to have knowledge of the 6D phase-space coordinates of all the constituents of the system, which at present, as explained in § 1.3, is still not accessible. Consequently, the objective of diverse dynamical modelling techniques (Battaglia and Nipoti, 2022) is to find methodologies to infer the intrinsic properties of the galaxy, i.e. ρ and Φ, from observation of their stellar components. It is of crucial importance for this modelling to provide accurate mass estimators which do not rely on strong assumptions about quantities inaccessible from observation. Given that these systems are pressure-supported and their kinematic data are often limited to the l.o.s. velocity dispersion measurement, it follows that dSphs and UFDs mass estimators will depend on this data. Among the most well-known mass estimators, there is the one presented in Wolf et al. (2010), which provides the dynamical mass within the 3D half-light radius $r_{\rm half}$:

$$M_{\rm dyn}(r_{\rm half}) = 3\frac{r_{\rm half}\langle\sigma^2_{\rm los}\rangle}{G} = 4\frac{R_{\rm e}\langle\sigma^2_{\rm los}\rangle}{G}, \tag{1.7}$$

where $R_{\rm e}$ is the half-light radius, $\langle\sigma^2_{\rm los}\rangle$ is the luminosity-weighted square of the l.o.s. velocity dispersion, and it is assumed $R_{\rm e} \approx (3/4)r_{\rm half}$. While the more recent Errani et al.

(2018) allows to estimate the mass within $1.8R_e$

$$M_{dyn}(< 1.8R_e) = 3.5\frac{1.8R_e\langle\sigma^2_{los}\rangle}{G}. \tag{1.8}$$

By employing the mass estimator Eq. 1.7, Battaglia and Nipoti (2022) obtained the dynamical masses shown in Figure 1.3 as a function of the corresponding V-band luminosity for a selection of DGs in the LG. Simon (2019) and Woo et al. (2008) have shown that for stellar populations typical of LG DGs, the stellar mass-to-light ratio is $M_\star/L \lesssim 2$. Therefore, a dynamical mass-to-light ratio, $M/L \equiv M_{dyn}(r_{half})/(L/2)$, much higher that the stellar one must necessarily be ascribed to DM. All classical dwarfs have been found with $M_{dyn}(r_{half}) \sim 10^7 M_\odot$ and $M/L \gtrsim 10$, which implies that the majority of the mass is in the form of DM, even within r_{half}. Furthermore, when all dSphs and UFDs in the LG are considered as in Figure 1.3, the dynamical mass-to-light ratios appear to increase with decreasing luminosity, with values ranging from 10 to even 1000 (diagonal lines in the picture). This is evidence that DGs are among the most DM-dominated systems.

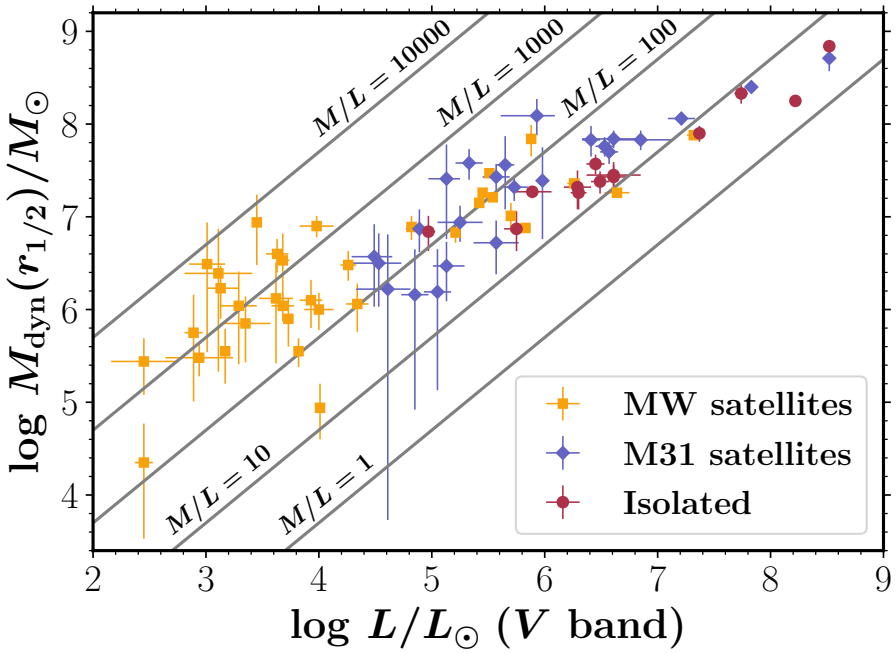

Fig. 1.3 – Dynamical mass M_{dyn} within the 3D half-light radius $r_{1/2}$ (r_{half} in Eq. 1.7) as a function of total V-band luminosity L for a selection of DGs in the LG. The diagonal lines indicate loci of constant mass-to-light ratio $M/L \equiv M_{dyn}(r_{half})/(L/2)$. Figure taken from Battaglia and Nipoti (2022).

1.5 Possible origin and evolution scenario

As explained in § 1.1, the great majority of dSph and UFDs are satellite galaxies of either the MW or M31 and they are located at distances smaller than the virial radius of the host galaxy. As a consequence, tidal interactions with the host galaxies may have severely truncated their DM halos. It is believed that dIrrs, dSphs, and UFDs share a significant

portion of their formation history. The main difference lies in their current state: dIrrs are still undergoing star formation, while in dSphs and UFDs, this process ceased at some point in the past.

The presence of ultra-violet radiation is expected for inhibiting star formation in dwarf-size halos from reionisation down to redshift $z \approx 2$ (Efstathiou, 1992; Bullock et al., 2000; Brown et al., 2014). Therefore, the passive galaxies observed in the present-day Universe may be fossil galaxies, i.e. systems observed in the present-day Universe but that completely formed in the early Universe. This is likely to be the case for UFDs, which exclusively possess very old stellar populations. However, this hypothesis seems to be not true for dSphs, in which the star formation histories (SFHs) are more extended and do not show clear signatures of signature of quenching due to reionisation.

In contrast, for dSphs, the mechanism responsible for inhibiting star formation and depleting these galaxies of their gas is believed to be a form of environmental quenching, resulting from a combination of both tidal and ram-pressure stripping, which, effectively, removes all the gas from the galaxy (Wetzel et al., 2015; Fillingham et al., 2016). The most popular interpretation for this scenario is that dSphs originated as dIrrs and later transformed due to interactions with the host galaxy, consistently with the fact that gas-rich DGs in the LG are segregated outside the virial radius of the host galaxy. In particular, the case of Leo I, presented by Ruiz-Lara et al. (2021), supports this scenario. The last peak of star formation in Leo I happened 1 Gyr ago together with its most recent perigalactic passage, and subsequently it was substantially quenched. Most probably during this passage at the pericentre, the ram pressure by the MW gas halo stripped the galaxy from its gas thus transitioning Leo I from dIrr to dSph.

However, nowadays a plethora of observations (Tolstoy et al., 2004; Battaglia et al., 2006, 2011; Amorisco and Evans, 2012; Fabrizio et al., 2016; Breddels and Helmi, 2014; Kordopatis et al., 2016; Pace et al., 2020; Spencer et al., 2017) have shown evidence that almost all stellar populations of classical dwarfs are composed of multiple chemo-kinematic components (CKCs), i.e. the stellar populations are described by the super-position of components with different mean metallicity, spatial distribution and kinematics. Since these different populations within the same galaxy must have different origins, it suggests that the history of dSphs may be far more complex, with the possibility that accretion of gas or other stellar systems was more common than expected.

1.6 Cosmological context

According to the Cold Dark Matter (CDM) cosmology, DM consists of weakly interacting particles that became non-relativistic before decoupling. CDM, thus, has negligible thermal velocity and does not suppress structure formation on any scale relevant for galaxy formation (Peebles, 1980). The formation of the known structures in this scenario occurs *bottom-up*: smaller systems were the first to virialise, while larger systems formed later through mergers and accretion of smaller ones and diffused matter. Usually referred to as hierarchical merging, this is the mechanism supposed to drive the growth of DM halos.

DM-only N-body simulations in this cosmological context predict that the mass den-

sity distribution $\rho(r)$ of DM structures is well described by cusped profiles, such as the Navarro et al. (1996) profile

$$\rho(r) = \frac{\rho_0}{\left(\frac{r}{r_\mathrm{s}}\right)\left(1+\frac{r}{r_\mathrm{s}}\right)^2}, \tag{1.9}$$

where ρ_0 and r_s are some characteristic density and radius, respectively. Moreover, with high-resolution simulations, it is also possible to constrain the halo mass function of LG-like groups of galaxies to be $\mathrm{d}N(M)/\mathrm{d}M \sim M^{-\alpha}$ with $\alpha \approx 1.9$. Being a decreasing function of the mass, this profile suggests that a large amount of the halos is in the range of low masses.

However, on smaller scales, as the one of DGs, these predictions show discrepancies with observations. There are three classic problems associated with the small-scale predictions for DM in the ΛCDM framework.

Core-cusp problem DM only ΛCDM simulations predict that halo density profiles should rise steeply at a small radius (Navarro et al., 2010). The first evidence against this prediction came from the Hα rotational curves of Low Surface Brightness (LSB) galaxies and dIrrs (McGaugh et al., 2001; Marchesini et al., 2002), which rather suggest cores of constant densities. Whether dSphs have cored or cusped profiles is still a matter of debate, as shown by Hayashi et al. (2020). Draco, for example, is believed to have a cuspy DM halo, while the DM halo of Fornax is likely cored (Pascale et al., 2018; Battaglia and Nipoti, 2022). However, even in dSphs that are seemingly compatible with a cusped profile, the best observations suggest a preference against the steep central slope predicted by ΛCDM model (Battaglia et al., 2008; Walker and Peñarrubia, 2011). Even though for dSphs there is no clear tension between the cosmological simulations and the inferred DM halos, this incompatibility is still evident in the case of dIrrs (Bullock and Boylan-Kolchin, 2017).

The mechanism responsible for such cored profiles is still unclear. One of the most accredited hypotheses suggests that interactions between DM particles and baryons would eventually redistribute the energy and momentum of DM particles, thus diluting the inner density and leading to a cored profile (e.g. Pontzen and Governato, 2014; Nipoti and Binney, 2015).

Missing satellite problem From the highest-resolution cosmological simulations of LG or even MW scales halos, the number of subhalos with masses large enough to have supported molecular cooling ($M_\mathrm{peak} \gtrsim 10^7 M_\odot$) are expected to be of the order of 10^3 (Springel et al., 2008; Stadel et al., 2009; Griffen et al., 2016). However, at present, only ~ 40 satellites have been observed to orbit within the virial radius of the MW (Drlica-Wagner et al., 2015).

Even though future observation may bring the number of UFDs to the order of the hundreds, it is extremely unlikely to reach the predicted thousands. Alternatively, the existence of dark satellites (Helmi et al., 2012), i.e. halos failed to accrete gas and form stars due to environmental quenching mechanisms, is one of the theories proposed to solve this problem.

Too-big-to-fail problem This problem is strictly related to the core/cusp one and concerns the density of larger ($M_{\rm vir} \sim 10^{10} M_{\odot}$) halos in the local Universe. As for the missing satellites problem, too few galaxies with such inferred halos have been detected. However, halos of this mass are generally believed to be too massive to have failed star formation, thus the fact that they are missing cannot be addressed to halos that remained dark, which would inhibit their observations. In addition, the absence of these halos is in contrast with all the observed DM-dominated UFDs, because it is not clear why more massive halos should fail to form stars, while less massive halos do not.

An alternative solution may be to abandon the CDM paradigm in favour of a Warm Dark Matter (WDM) cosmology. The introduction of a warmer component would inhibit structure formation at smaller scales, thereby reducing the number of expected satellites, and would also reproduce cored profiles (Bullock and Boylan-Kolchin, 2017).

It is currently evident that our understanding of structure formation at the scale of DGs is incomplete. Consequently, a comprehensive investigation of the potential events that these galaxies may have undergone is essential for placing meaningful constraints on cosmological models.

II

The Sextans Dwarf Spheroidal

The Sextans dwarf spheroidal galaxy was the last classical dwarf to be discovered, mostly due to its low luminosity and location on the plane of the sky, which suffers from a considerable amount of contamination from Milky Way stars.
In § 2.1 the global properties of Sextans will be presented, focusing on its stellar population in § 2.1.1, its structural properties in § 2.1.2 and its dark matter content in § 2.1.3.
§ 2.2 will review the main evidence that Sextans may have been subject to accretion events in the past, which is the primary motivation of this thesis. § 2.2.2 will illustrate the work by Cicuéndez and Battaglia (2018), who found a peculiar ring-like structure in the kinematics and metallicity distribution of the galaxy, using spectroscopic data. § 2.2.1 will focus on the work by Kim et al. (2019), who found a roundish overdensity in a metal-poor selection of the galaxy stellar population, using photometric data.

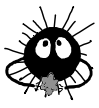

2.1 Sextans Dwarf Spheroidal overview

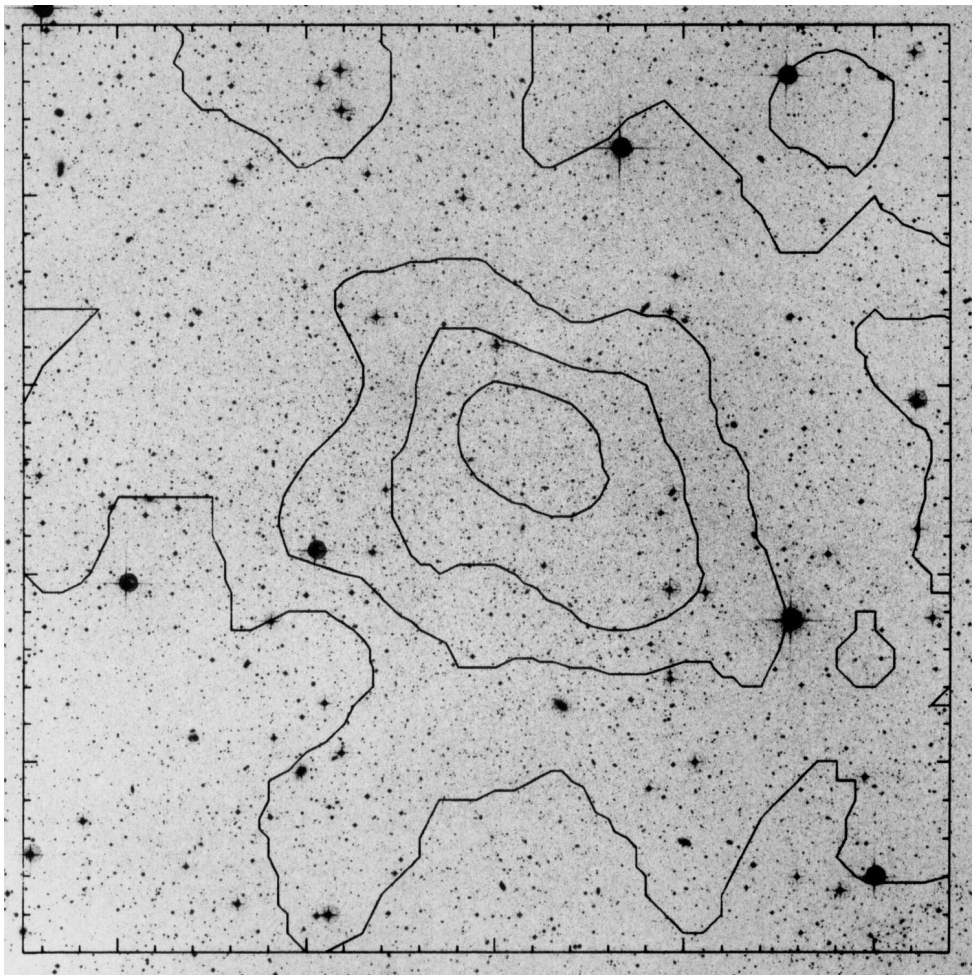

Fig. 2.1 – The Sextans dSph from a IIIaJ plate (J10658c) taken on the UK 1.2-m Schmidt Telescope. Overlaid is an isodensity contour map of the stellar distribution covering $1° \times 1°$ of the region. Picture taken from Irwin et al. (1990).

The last of the classical dSphs to be discovered was found at a heliocentric distance of 86 kpc in the Sextans constellation by Irwin et al. (1990) and presented with the image in Figure 2.1. The Sextans dSph was discovered relatively late with respect to the other classical dwarfs primarily because it is one of the most diffuse and faint dSphs, with a central brightness $\Sigma_0 = 18.2 \pm 0.5$ mag arcmin^{-2} and luminosity $L = 4.1 \pm 1.9 \times 10^5 L_\odot$ (Irwin and Hatzidimitriou, 1995). In addition to this, its location in celestial coordinates (R.A. $10^{\mathrm{h}}13\ ^{\mathrm{m}}03^{\mathrm{s}}$, Dec. -01° 36′ 54″, Norris et al., 2014) results in a considerable amount of contamination from Milky Way stars, making the exploration of its 2D structure particularly challenging.

The observational properties of Sextans, as collected by Battaglia et al. (2011), are summarised in Tab. 2.1.

Parameter	value
[R.A.(J2000), Dec.(J2000)]	$[10^h13^m03^s, -01^\circ\ 36'\ 54'']$
ϵ	0.35
$R_{\rm core}$	16.6 arcmin
$R_{\rm tidal}$	160 arcmin
$R_{\rm e}$	15.5 arcmin
$v_{\rm sys}$	226.0±0.6 km s^{-1}
σ	8.4±0.4 km s^{-1}
(m-M)$_0$	19.67
Distance	86 kpc
L_V	$4.37 \pm 1.69 \times 10^5$ L$_\odot$
V$_{\rm HB}$	20.35
E(B-V)	0.0477

Tab. 2.1 – Main parameters of Sextans. From top to bottom:: coordinates of the optical centre (R.A.,Dec.); ellipticity ε, King core and tidal radii $R_{\rm core}$ ad $R_{\rm tidal}$; exponential radius $R_{\rm e}$; heliocentric l.o.s. systemic velocity $v_{\rm sys}$; global l.o.s. velocity dispersion in the heliocentric system σ; distance modulus (m-M)$_0$ and heliocentric distance; luminosity in V-band L_V (based on the apparent magnitude measured by Irwin and Hatzidimitriou 1995 adjusted for the distance of 86 kpc by Łokas 2009); V magnitude of the horizontal branch V$_{\rm HB}$; reddening E(B-V). Adapted from Battaglia et al. (2006)

2.1.1 Stellar population

According to McConnachie (2012), the total mass of Sextans stellar population is

$$M_\star = 4.4 \times 10^5 M_\odot, \tag{2.1}$$

obtained by assuming a constant, unitary, mass-to-light ratio.

It is currently well established that the majority of stars in Sextans are old, with typical ages exceeding 10 Gyr. This conclusion is supported by a substantial body of evidence, such as Mateo et al. (1991, 1995), Bellazzini et al. (2001) or Goon Lee et al. (2003). However, a significant population of stars have also been identified on the main sequence (MS), above the oldest turn-off. The age of these stars has been debated for many years after Mateo et al. (1991) suggested that these could be MS stars as young as 2 Gyr. After deep Suprime-Cam V and I photometry at Subaru Telescope, Okamoto et al. (2017) demonstrated that their spatial distribution is highly analogous to that of the old (>10 Gyr) MS stars, while Cicuéndez et al. (2018) indicated that it is more probable that they are blue stragglers (BS) stars with ages consistent with the dominant Sextans stellar population. Furthermore, Bettinelli et al. (2018) and Revaz and Jablonka (2018) have brought evidence that Sextans ceased forming stars ≈12.9 Gyr ago before the end of the reionisation epoch. Consequently, Sextans can be classified as a fossil of the pre-reionisation era.

As in the case of other dSphs, Sextans displays evidence of metallicity and age gradients. Red Horizontal Branch (RHB) stars are observed to be more centrally concentrated

Parameter	Exponential	Sérsic	Plummer	King
Sérsic index n	-	$1.03^{+0.07}_{-0.07}$	-	-
Sérsic R_s [arcmin]	-	20^{+8}_{-8}	-	-
Exponential $R_{\rm exp}$ [arcmin]	$12.7^{+0.4}_{-0.4}$	-	-	-
Plummer R_s [arcmin]	-	-	$22.8^{+0.7}_{-0.7}$	-
King R_c [arcmin]	-	-	-	$13.8^{+0.9}_{-0.9}$
King R_t [arcmin]	-	-	-	120^{+20}_{-20}
2D Half-light R_e [arcmin]	$21.4^{+0.7}_{-0.6}$	20^{+8}_{-8}	$22.8^{+0.7}_{-0.7}$	22^{+2}_{-2}

Tab. 2.2 – Sextans structural parameters from best-fits. The Sérsic index n and projected half-light radius R_e appear in Eq. 1.2. The exponential R_e, in Eq. 1.4. The Plummer R_s, in Eq. 1.6. The King R_c and R_t, in Eq. 1.5. Adapted from Cicuéndez et al. (2018).

than the Blue Horizontal Branch (BHB) stars (Bellazzini et al., 2001; Harbeck et al., 2001; Goon Lee et al., 2003). Moreover, the analysis presented by Okamoto et al. (2017) suggests a minimum age difference of 3 Gyr between the outer parts (∼13 Gyr) and the central parts (∼10 Gyr). This implies that the younger stellar population is more centrally concentrated than the older one, which is consistent with the observed distribution of RHB and BHB stars. The spectroscopic follow-ups at medium–low resolution in the region of the calcium (CaII) triplet (8498Å, 8542Å and 8662 Å) revealed that the radial gradient of the metallicity is very small in Sextans, but the mean metallicity was observed to decrease with increasing distance from the centre. By employing VLT/FLAMES intermediate-resolution spectra of individual red giant branch (RGB) stars in the Ca II triplet region, Battaglia et al. (2011) showed that within the inner region ($R < 0.8$ deg) the metallicity [Fe/H] ranges from -3.2 to -1.4 dex, with an average $[\mathrm{Fe/H}]_{\rm avg}$ = -1.9 dex and a scatter of 0.6 dex. In contrast, at larger radii, the available stars in the sample exhibited metallicities that were all lower than [Fe/H] ∼-2.2 dex. These metallicities were found to be consistent with recent high-resolution measurements by Theler et al. (2020) of 81 member stars in Sextans, which found that [Fe/H] spanned a range from -3.2 to -1.5 dex. It is therefore clear that Sextans is an overall metal-poor system.

2.1.2 Structural properties

In order to derive the most accurate and quantitative structural properties of the stellar component of Sextans, recent works, such as Cicuéndez et al. (2018) and Tokiwa et al. (2023), have adopted a Bayesian analysis to fit the surface number density profile with the four cored profile models mentioned in § 1.2, i.e. the King, Sérsic, exponential and Plummer profiles. The results of Cicuéndez et al. (2018), perfectly compatible with those from Tokiwa et al. (2023), are presented in Tab. 2.2. As it can be seen in Figure 2.2, all cored profiles provide an adequate fit to the number density profile of Sextans stellar population, with the Plummer and King one being the most accurate, according to the authors.

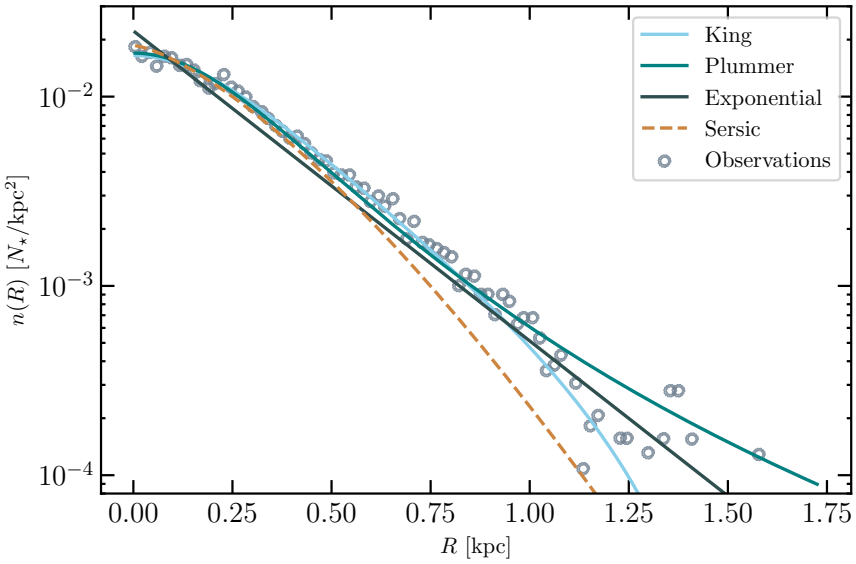

Fig. 2.2 – Surface number density profile of Sextans (grey points) as a function of the semi-major axis Cicuéndez et al. 2018. The colored lines correspond to the King (Eq. 1.5), Plummer (Eq. 1.6), exponential (Eq. 1.4) and Sérsic (Eq. 1.2) models. The models best-fit parameters are reported in Tab. 2.2

2.1.3 Mass content

The dynamical mass of Sextans was determined by Battaglia et al. (2011) using a Jeans modelling of the observed l.o.s. velocity dispersion profile. The method involves comparing the observed line-of-sight velocity dispersion $\sigma_{\rm los}$ in each radial bin with the values predicted by Jeans modelling, see § 3.3 for details. This comparison is done across a range of DM profile models and velocity anisotropy assumptions. In the case of a spherical, stationary, and non-rotating system, as assumed by Battaglia et al. (2011), the predicted $\sigma_{\rm los}$ depends on the choice of a mass density profile ρ and the anisotropy parameter β, which is indicative of the degree of radial anisotropy of the system, and the spatial distribution of the kinematic tracer, which is inferred from the surface density profile, see § 3.3.

As previously discussed in § 1.4, Sextans exhibits a remarkably high $M_{\rm dyn}/L$, which renders the stellar contribution to the total potential effectively negligible. Hence, DM can be considered the sole contributor to the dynamical mass of Sextans. Battaglia et al. (2011) considered two different models for a spherically symmetric DM halo potential:

- Pseudo-Isothermal sphere (cored model),

$$\rho_{\rm DM}^{\rm iso}(r) = \frac{\rho_0}{1 + \left(\frac{r}{r_c}\right)^2}, \tag{2.2}$$

where r_c is the core radius and ρ_0 the central density

- NFW model (cuspy model),

$$\rho_{\rm DM}^{\rm NFW}(r) = \frac{\delta_c \rho_c}{\left(\frac{r}{r_{\rm s}}\right)\left(1+\frac{r}{r_{\rm s}}\right)^2}, \tag{2.3}$$

  where r_s is a scale radius, ρ_c the present critical density and δ_c a characteristic over-density, defined as $\delta_c = 100c^3 g(c)/3$, where $c = r_{\rm vir}/r_s$ is the concentration parameter, $r_{\rm vir}$ the virial radius and $g(c) = (\ln(1+c) - c/(1+c))^{-1}$.

Once a suitable ρ well reproduces the observed $\sigma_{\rm los}$, the dynamical mass is simply given by integrating over the spherical volume up to a limit radius.

The results of the fitting procedure are presented in Tab. 2.3. The l.o.s. velocity dispersion profile of Sextans was found consistent with both a cored DM halo with a large core radius and a cuspy halo with low concentration. Furthermore, the dynamical mass within the last measured point of the profile ($R = 2.3$ kpc) is in the range $(2-4)\times10^8 M_\odot$, indicating a dynamical mass to stellar mass ratio of at least 10^3.

	$\chi^2_{\rm red}$	p_β	$M(< R_{\rm last})$	$M_{\rm vir}$
Cored $r_c = 3.0$ kpc $\beta = const$	0.2	$0.06 < \beta < 0.6$	$4.0 \pm 0.7 \times 10^8$ M$_\odot$	
Cored $r_c = 1.5$ kpc $\beta = \beta_{\rm OM}$[†]	0.6	$r_a > 1.5$ kpc	$3.2 \pm 0.7 \times 10^8$ M$_\odot$	
Cuspy c = 10 $\beta = const$	0.7	$-1.4 < \beta < 0$	$1.9 \pm 0.6 \times 10^8$ M$_\odot$	$2.6 \pm 0.8 \times 10^9$ M$_\odot$

Tab. 2.3 – Parameters of the best-fitting DM models from the mass modelling of Sextans Battaglia et al. (2011). The columns show, from left to right: the reduced χ^2, the anisotropy parameter (i.e., the value of β when it is constant, or the anisotropy radius r_a [kpc] for the $\beta = \beta_{\rm OM}$ case), the mass contained within the last measured point $M(< R_{\rm last})$ (at $R_{\rm last} = 2.3$ kpc), and the virial mass $M_{\rm vir}$ for the cuspy profile.

2.2 Signs of accretion in Sextans

As mentioned in § 1.6, mergers are also expected between low mass halos of DGs (Fakhouri et al., 2010). This assertion is supported by dissipationless cosmological zoom-in simulations of Deason et al. (2014), which showed that very few isolated DG in the LG could have escaped from a major merger from their formation until now. The search for any evidence of these events in DGs is of particular importance for demonstrating hierarchical mergers at the smallest scales.

The kinematics and density distribution of the stellar component of several LG DGs have revealed the existence of different substructures, which are likely the result of the disruption of smaller accreted systems. In the case of the dSphs, some well-known examples are Fornax and Carina. Various pieces of evidence suggest that Fornax may have experienced merger events. For instance, Coleman et al. (2004) observed a shell-like structure,

[†] Osipkov-Merritt parametrisation $\beta_{\rm OM} = r^2/(r^2+r_a^2)$, where r_a is the anisotropy radius, Osipkov (1979); Merritt (1985)

while a double-peaked l.o.s. velocity distribution was found for its metal-poor stars. Additionally, both Battaglia et al. (2006) and del Pino et al. (2015) noted an asymmetry in the spatial distribution of Fornax's younger stars, which are more centrally concentrated. Another example is Carina, which presents evidence of two different episodes of star formation formed from gas with different metallicities, a feature that is inconsistent with simple evolution in an isolated system (de Boer, T. J. L. et al., 2014). Before Sextans, the smallest galaxy exhibiting unequivocal signs of accretion was And II ($M_\star \sim 7.6 \times 10^6 M_\odot$), where Amorisco et al. (2014) detected the presence of a stellar stream. The works of Cicuéndez and Battaglia (2018) and Kim et al. (2019), place Sextans, with a stellar mass $\sim 10^5 M_\odot$, as the smallest galaxy currently showing clear observational signs of accretion at present.

In the following sections, I will present the studies that inspired the idea of this thesis, which aims to reproduce the peculiar observational features of Sextans using N-body simulations. Specifically, this work models the interaction between the Sextans and a smaller satellite, with the goal of explaining the observed ring-like substructures as the result of a recent encounter. These studies have shaped the simulation setup and analysis, guiding efforts to replicate the distinctive spatial and kinematic signatures observed in Sextans.

2.2.1 A possible relic star cluster

Kim et al. (2019) observed Sextans with Suprime-Cam on Subaru 8.2 m telescope through Ca-, b-, and y-band filters. b and y are two Strömgren filters, b is centred at 4670 Å and has full width at half maximum (FWHM) of 180 Å, while y is centred at 5470 Å and FWHM=230 (Strömgren, 1966). The Ca filter is a narrow (FWHM = 90 Å) filter centred on the ionised calcium H and K lines, originally developed by Anthony-Twarog et al. (1991) for metal-poor dwarfs and red giants stars or, more generally, for regions where the $uvby$ metallicity index $m_1 = (v-b)-(b-y)$ loses sensitivity. In order to discriminate the metal-poor and metal-rich stars, the authors used a photometric metallicity indicator, i.e. the index developed by Anthony-Twarog et al. (1991) $hk \equiv (Ca-b)-(b-y)$.

The results are shown in Figure 2.3. The panels in the upper row present the spatial distributions of all member stars (left), metal-poor stars (centre), and metal-rich stars (right), superimposed with isodensity curves. The central panel clearly shows a number density excess of metal-poor stars located at 7.7 arcmin from the centre (∼190 pc) exhibiting a roundish shape with a radius of ∼80 pc. The panels in the bottom row displays the statistical significance contours of the number excess for each group of stars. To quantify the significance of the off-centre peak of metal-poor stars, a smoothed surface density map was constructed using a Kernel Density Estimation (KDE) with a bandwidth five times larger than the original. This smoothed map was subtracted from the original to create a residual map. The off-centre peak of metal-poor stars was found to be significant at over 5σ, making it the most distinct feature in the contour map. Furthermore, the strong concentration of this overdensity, coupled with its exclusive occurrence in the metal-poor selection, suggests that it may be a gravitationally bound object, with the authors suggesting that it may be a relic star cluster recently dissolved. The size of this overdensity

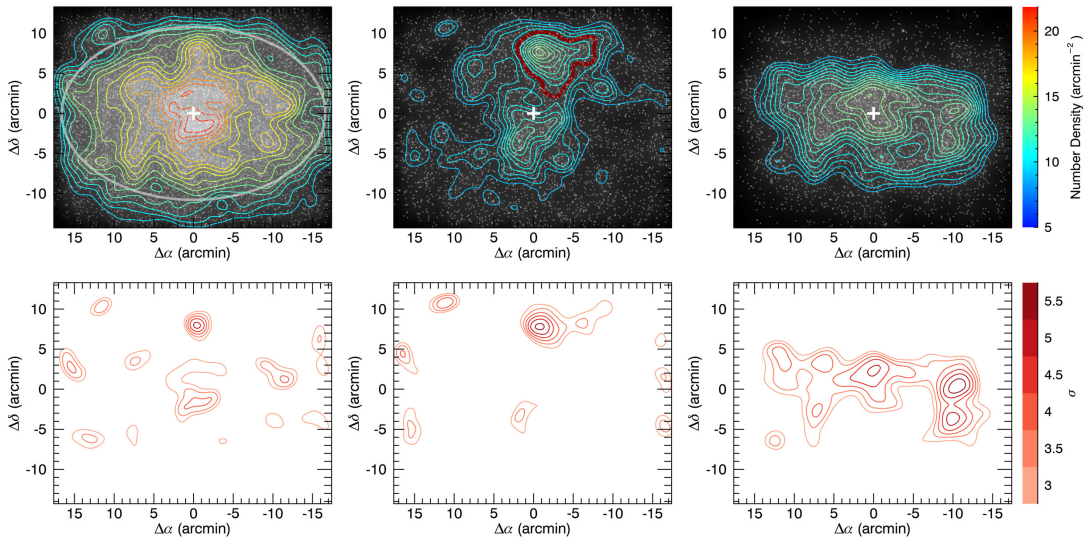

Fig. 2.3 – Upper row: spatial distributions of all member stars (left), metal-poor stars (centre), and metal-rich stars (right) along with the surface number density contours. The images are rotated so that the major axis of Sextans is along the x-axis. The white cross represents the centre of the galaxy (Irwin et al., 1990), and the grey ellipse denotes the core radius and ellipticity. In the central panel, a number excess of metal-poor stars is visible at about 7.7 arcmin above the centre. The thick red locus is the isodensity contour of 7.5 arcmin^{-2} and the selection area for stars associated with a possible relic star cluster. Lower row: statistical significance contours from 3σ in steps of 0.5σ.

will be used as the reference for the stellar component of the object accreted by Sextans in the N-body simulations explored in this thesis.

2.2.2 A ring-like feature

By re-analysing spectroscopic sample from Walker et al. (2009b), Cicuéndez and Battaglia (2018) detected a ring-like substructure with a considerably larger systemic l.o.s. velocity with respect to the systemic velocity of Sextans and lower metallicity than the rest of the stars in the sample.

The spectroscopic dataset consisted of l.o.s. heliocentric velocities and pseudo-equivalent widths of the Mg-triplet absorption feature (ΣMg) obtained with the Michigan/MIKE Fiber System MMFS at the Magellan 6.5m Clay Telescope. From the dataset, the authors included only those RGB and HB stars with a probability greater than 95% of belonging to Sextans, using the membership probabilities determined in Cicuéndez et al. (2018). From this preliminary selection, Figure 2.4 was obtained by plotting the positions of the stars on the plane of the sky and assigning the colours on the basis of different quantities in the two panels. The left panel shows the l.o.s. velocities with respect to the Sextans rest frame velocity, while in the right panel, stars are colour-coded for ΣMg. The values assigned to each star have been estimated as the weighted average of neighbouring observed data within a median kernel of 5 arcmin. This smoothing is commonly adopted since helps reduce the noise, making the velocity and metallicity maps easier to interpret, and revealing larger-scale patterns that in some cases might be obscured.

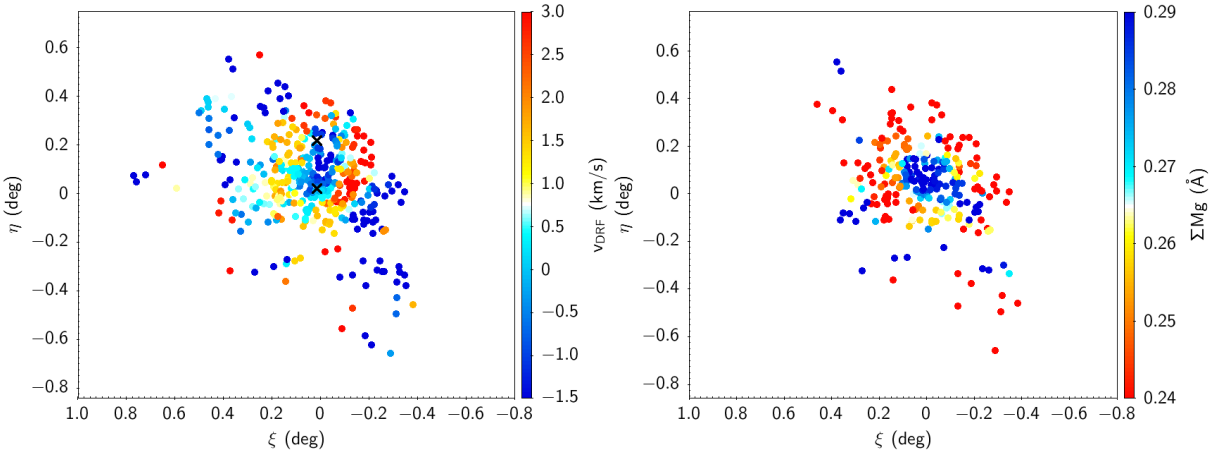

Fig. 2.4 – W09 spectroscopic sample of Sextans most probable members, colour-coded using smoothed l.o.s. velocities (left) and ΣMg values (right). Upper and lower black crosses in the left panel mark the centres of the cold kinematic substructures detected in Walker et al. (2006), and in Battaglia et al. (2011), respectively.

In the left panel, it can be distinguished a ring-like feature that has a systemic l.o.s. velocity ∼3 km/s larger than than the systemic velocity of Sextans. Notably, the ring-like structure does not show the *one side proceeding one arm receding* kinematics typical of a rotational object, but rather almost homogeneous positive velocities. A ring feature is also clearly visible at the same location in the right panel, which also indicates that the stars populating this feature have a lower metallicity with respect to the others. Additionally, the authors estimated that the fraction of stars associated with the ring-like structure corresponds to 20% of the total stars in the sample.

III

Equilibrium Theory for Non-Collisional Systems

The aim of this chapter is to give the theoretical basis necessary to describe the type of systems that will be involved in the simulations subject of this thesis. As mentioned in §§ 1, dSph are collisionless systems and for the majority of them, ongoing interactions with nearby objects have a negligible effect on their internal kinematics, indicating that they can be reasonably considered to be in an equilibrium state.
This chapter will thus introduce what collisionless stellar systems are and the fundamental principles of equilibrium theory, with a particular focus on the tools that will be employed in the generation of initial conditions for the N-body simulations explored in §§ 4. In § 3.1, the concept of the distribution function will be introduced, highlighting its connection to the collisionless Boltzmann equation. Then, in § 3.2, the concept of integrals of motion will be explored, along with their use in deriving the Eddington formula which gives an explicit form to the distribution function. Moreover, this section will show some examples in which the distribution function is analytical. Finally, § 3.3 will demonstrate how the distribution function and the Boltzmann equation relate to observable quantities in astrophysical systems.
This chapter will follow the treatment of Binney and Tremaine (2008).

3.1 Introduction to distribution functions

A system is defined as collisionless if the effects of two-body interaction on the motion of its particles are negligible. In a galaxy, this implies that the net gravitational force acting on a star is determined by the overall structure of the galaxy, rather than by its proximity to neighbouring stars. In this hypothesis, a system composed of a large number N of equal stars moving under the influence of a smooth potential, $\Phi(\boldsymbol{x}, t)$, can be fully described at any time t by its so-called distribution function (DF).

A DF is a function $f(\boldsymbol{x}, \boldsymbol{v}, t)$ defined such that $f(\boldsymbol{x}, \boldsymbol{v}, t)\mathrm{d}^3\boldsymbol{x}\mathrm{d}^3\boldsymbol{v}$ represents the probability that at the specified time t, a star can be found within the phase-space volume element $\mathrm{d}^3\boldsymbol{x}\mathrm{d}^3\boldsymbol{v}$ centred in $(\boldsymbol{x}, \boldsymbol{v})$. As probability density functions, two fundamental properties inherent to any DF are:

$$\int \mathrm{d}^3\boldsymbol{x}\mathrm{d}^3\boldsymbol{v} f(\boldsymbol{x}, \boldsymbol{v}, t) = 1 \quad \text{and} \quad f(\boldsymbol{x}, \boldsymbol{v}, t) \geq 0. \tag{3.1}$$

By definition, any DF can depend on time, either explicitly or through the phase-space coordinates $\boldsymbol{x}(t)$ and $\boldsymbol{v}(t)$. For the rest of this section, for the sake of simplicity, the phase-space coordinates will be collected in the six-dimensional vector $\boldsymbol{w}$:

$$\boldsymbol{w} \equiv (\boldsymbol{x}, \boldsymbol{v}) = (w_1, ..., w_6) \qquad \dot{\boldsymbol{w}} = (\dot{\boldsymbol{x}}, \dot{\boldsymbol{v}}) = (\boldsymbol{v}, -\boldsymbol{\nabla}\Phi), \tag{3.2}$$

where the equivalence $\dot{\boldsymbol{v}} = -\boldsymbol{\nabla}\Phi$ is derived from the equations of motion in classical mechanics. To clarify the behaviour of $f(\boldsymbol{w})$ for different sets of phase-space coordinates, let $\boldsymbol{W}$ be some arbitrary set of phase-space coordinates, with DF $F(\boldsymbol{W})$. Then the probability of finding a star in a phase-space volume $\mathcal{V}$ must be the same in both coordinates systems, that is:

$$\int_{\mathcal{V}} \mathrm{d}^6\boldsymbol{W} F(\boldsymbol{W}) = \int_{\mathcal{V}} \mathrm{d}^6\boldsymbol{w} f(\boldsymbol{w}). \tag{3.3}$$

If $\mathcal{V}$ is small enough, f and F will be approximately constant throughout the volume, and they can be taken outside the integrals, yielding to

$$F(\boldsymbol{W}) \int_{\mathcal{V}} \mathrm{d}^6\boldsymbol{W} = f(\boldsymbol{w}) \int_{\mathcal{V}} \mathrm{d}^6\boldsymbol{w}. \tag{3.4}$$

Therefore, only if the coordinates are canonical, meaning $\int_{\mathcal{V}} \mathrm{d}^6\boldsymbol{W} = \int_{\mathcal{V}} \mathrm{d}^6\boldsymbol{w}$, the DFs are equivalent, i.e. $F(\boldsymbol{W}) = f(\boldsymbol{w})$.

3.1.1 Velocity moments of distribution functions

One method to link a DF with the observables is through its velocity moments. The n-order moment, denoted as $\boldsymbol{T}^{\mathrm{n}}$ of a DF $f(\boldsymbol{x}, \boldsymbol{v}, t)$ is a tensor of order n, defined by its components:

$$T^{\mathrm{n}}_{i,j,\ldots,k}(\boldsymbol{x}, t) = \int \mathrm{d}^3\boldsymbol{v} \overbrace{v_i v_j \ldots v_k}^{\mathrm{n}} f(\boldsymbol{x}, \boldsymbol{v}, t) \tag{3.5}$$

Considering that the DF can be alternatively normalised so that the integral over the whole phase space gives the total number of stars N, i.e.

$$\int \mathrm{d}^3\boldsymbol{x}\mathrm{d}^3\boldsymbol{v} f(\boldsymbol{x},\boldsymbol{v}) = N, \tag{3.6}$$

then low-order moments have simple physical meanings:

$$\int \mathrm{d}^3\boldsymbol{v} f(\boldsymbol{x},\boldsymbol{v}) = n(\boldsymbol{x}) \quad 0^{\text{th}} \text{ moment, number density} \tag{3.7}$$

$$\frac{1}{n(\boldsymbol{x})}\int \mathrm{d}^3\boldsymbol{v} v_i f(\boldsymbol{x},\boldsymbol{v}) = \overline{v}_i(\boldsymbol{x}) \quad \begin{array}{l} 1^{\text{st}} \text{ moment, mean velocity} \\ \text{of the } i\text{-th components} \end{array} \tag{3.8}$$

$$\left.\begin{array}{r} \dfrac{1}{n(\boldsymbol{x})}\displaystyle\int \mathrm{d}^3\boldsymbol{v} v_i^2 f(\boldsymbol{x},\boldsymbol{v}) = \overline{v_i^2}(\boldsymbol{x}) \\ \dfrac{1}{n(\boldsymbol{x})}\displaystyle\int \mathrm{d}^3\boldsymbol{v} v_i v_j f(\boldsymbol{x},\boldsymbol{v}) = \overline{v_i v_j}(\boldsymbol{x}) \end{array}\right\} \quad 2^{\text{nd}} \text{ moments} \tag{3.9}$$

The 2-nd order moments are usually grouped together in the velocity dispersion tensor

$$\sigma_{ij}^2 \equiv \overline{(v_i - \overline{v}_i)(v_j - \overline{v}_j)}, \tag{3.10}$$

which is the 2-nd order moment centred on the mean velocity. It can therefore be rewritten as

$$\begin{aligned} \sigma_{ij}^2 &= \frac{1}{n(\boldsymbol{x})}\int \mathrm{d}^3\boldsymbol{v} f(\boldsymbol{x},\boldsymbol{v})(v_i - \overline{v}_i)(v_j - \overline{v}_j) \\ &= \frac{1}{n(\boldsymbol{x})}\left[\int \mathrm{d}^3\boldsymbol{v} f(\boldsymbol{x},\boldsymbol{v}) v_i v_j - \int \mathrm{d}^3\boldsymbol{v} f(\boldsymbol{x},\boldsymbol{v})\overline{v}_i v_j - \int \mathrm{d}^3\boldsymbol{v} f(\boldsymbol{x},\boldsymbol{v}) v_i \overline{v}_j + \int \mathrm{d}^3\boldsymbol{v} f(\boldsymbol{x},\boldsymbol{v})\overline{v}_i\overline{v}_j\right] \\ &= \frac{1}{n(\boldsymbol{x})}[n\overline{v_i v_j} - n\overline{v}_i\overline{v}_j - n\overline{v}_j\overline{v}_i + n\overline{v}_i\overline{v}_j] \\ &= \overline{v_i v_j} - \overline{v}_i\overline{v}_j. \end{aligned} \tag{3.11}$$

The velocity dispersion tensor describes the spread in the velocity of stars in a system around the mean value $\overline{\boldsymbol{v}}$. Since the tensor is symmetric $\left(\sigma_{ij}^2 = \sigma_{ji}^2\right)$, it can be diagonalised in a tensor $\tilde{\sigma}$, whose elements are $\tilde{\sigma}_{ij}^2 = \tilde{\sigma}_{ii}^2\delta_{ij}$. The ellipsoid that has $\tilde{\sigma}_{11}$, $\tilde{\sigma}_{22}$ and $\tilde{\sigma}_{33}$ for its semi-axis length is the velocity ellipsoid at $\boldsymbol{x}$. In particular, if all diagonal elements have the same value σ, so that

$$\tilde{\sigma}_{ij} = \sigma^2\delta_{ij}. \tag{3.12}$$

the system is called isotropic.

Furthermore, as it will be seen in § 3.3, the velocity dispersion can be interpreted as a form of anisotropic pressure which shapes the galaxy.

3.1.2 Collisionless Boltzmann equation

Any given star moves through phase-space, and so the probability of finding it at any given phase-space location evolves with time. As f evolves, the probability must be conserved,

much like how mass is conserved in a fluid flow.

In Eq. 3.2, I introduced $\dot{\boldsymbol{w}}$, which a six-dimensional vector that bears the same relationship to the six-dimensional vector $\boldsymbol{w}$ as the three-dimensional fluid flow velocity $\boldsymbol{v} = \dot{\boldsymbol{x}}$. The flow $\dot{\boldsymbol{w}}$ must then conserve stars in time. This is due to the fact that, in the absence of encounters, stars are immersed in a smooth gravitational potential. Consequently, they cannot "jump" from one point in the phase space to another, but instead, they drift smoothly through the phase space. It follows that $f(\boldsymbol{w}, t)$ must satisfy a continuity equation analogous to that which applies to ordinary fluids. Using Einstein notation, where repeated indices are summed over, this conservation law can be expressed as

$$\frac{\partial f}{\partial t} + \frac{\partial \left(f \dot{w}_k\right)}{\partial w_k} = 0, , \tag{3.13}$$

where w_k is the k-th component of $\boldsymbol{w} = (w_1, \ldots, w_6)$. This equation can be simplified by considering the definition of $\dot{\boldsymbol{w}}$ in Eq. 3.2 and noting that

$$\frac{\partial \dot{w}_k}{\partial w_k} = \frac{\partial v_k}{\partial x_k} + \frac{\partial \dot{v}_k}{\partial v_k} = -\frac{\partial}{\partial v_k}\left(\frac{\partial \Phi}{\partial x_k}\right) = 0, \tag{3.14}$$

where it was used $\dot{\boldsymbol{v}} = -\boldsymbol{\nabla}\Phi$ and the fact that $\partial v_k / \partial x_k = 0$, since x_k and v_k are independent coordinates of the phase space. The last term vanishes as well because Φ is not an explicit function of velocities, nor of its derivative. As a result of these simplifications, Eq. 3.13 reduces to the so-called collisionless Boltzmann equation:

$$\frac{\partial f}{\partial t} + \dot{w}_k \frac{\partial f}{\partial w_k} = 0. \tag{3.15}$$

The physical meaning of Eq. 3.15 becomes more evident when the concept of convective derivative $\mathrm{d}/\mathrm{d}t$ is extended to six dimensions as follows

$$\frac{\mathrm{d}}{\mathrm{d}t} = \frac{\partial}{\partial t} + \dot{w}_k \frac{\partial}{\partial w_k}. \tag{3.16}$$

The collisionless Boltzmann equation then assumes the simple form

$$\frac{\mathrm{d}f}{\mathrm{d}t} = 0. \tag{3.17}$$

This implies that the flow of the probability fluid through the phase space is incompressible, i.e. the phase-space density f of the fluid surrounding a given star remains constant with time.

3.2 The Jeans theorem

Finding a solution to the collisionless Boltzmann equation is typically very challenging due to the fact that it depends on seven variables and that, in the most general case, it is a partial differential equation for which general solutions are not known. The Jeans theorem allows for making some steps forward in the quest for solutions to the collisionless

Boltzmann equation, by establishing a connection between the integrals of motion and the DF. Given a stationary potential $\Phi(\boldsymbol{x})$, a function of the phase-space coordinates $I(\boldsymbol{x}(t), \boldsymbol{v}(t))$ is defined to be an integral of motion if and only if

$$\frac{\mathrm{d}}{\mathrm{d}t}[I(\boldsymbol{x}(t), \boldsymbol{v}(t))] = 0 \tag{3.18}$$

along all orbits. It is worth noting that integrals of motion satisfy the same conditions of a steady-state DF, i.e. $\mathrm{d}f/\mathrm{d}t = 0$. This property leads to the Jeans theorem.

Jeans theorem Any steady-state solution of the collisionless Boltzmann equation depends on the phase-space coordinates only through integrals of motion of the galactic potential, and any function of the integrals yields a steady-state solution of the collisionless Boltzmann equation.

If the form or the existence of certain integrals of motion is known, then any function of these will solve Eq. 3.15 and conversely, the DF must be a function of these integrals of motion. However, no matter how robust a theorem may be, there can still be cases in which, even if the existence of an integral of motion is proven, it may not have an analytical expression. In such cases, an analytical form for the DF cannot be obtained either.

DFs for stationary collisionless stellar systems are usually classified on the basis of the integrals of motion on which they depend. For spherical systems, the DF can either depend only on the Hamiltonian H or on the Hamiltonian H and the angular momentum modulus L. In the axisymmetric cases, instead, the DF is a function of the Hamiltonian H and the third angular momentum component L_z. For the purposes of this thesis, the focus will be on the first case.

3.2.1 Distribution functions for ergodic spherical systems

For a spherical steady-state system, the potential Φ and the number density n are such that

$$\begin{aligned} \Phi(\boldsymbol{x}, t) &\Rightarrow \Phi(r) \\ n(\boldsymbol{x}, t) &\Rightarrow n(r) \end{aligned} \tag{3.19}$$

where $r = \sqrt{x^2 + y^2 + z^2}$. Conveniently, for these systems, the Hamiltonian $H = \frac{1}{2}|\boldsymbol{v}|^2 + \Phi(r)$ is an integral of motion. As a consequence, the Jeans theorem assures that it is possible to define a DF $f = f(H) = f\left(\frac{1}{2}|\boldsymbol{v}|^2 + \Phi(r)\right)$, which is called ergodic.

Since $f = f(\frac{1}{2}|\boldsymbol{v}|^2 + \Phi(r))$ is an even function of the velocities, it follows that

$$\overline{\boldsymbol{v}}(r) = \frac{1}{n(r)} \int \mathrm{d}^3\boldsymbol{v}\, \boldsymbol{v} f\left(\frac{1}{2}|\boldsymbol{v}|^2 + \Phi(r)\right) = \boldsymbol{0}, \tag{3.20}$$

i.e. the mean velocity vanishes everywhere. Considering the velocity dispersion tensor

$$\sigma_{ij}^2 = \overline{v_i v_j} = \int \mathrm{d}^3\boldsymbol{v}\, v_i v_j f\left(\frac{1}{2}|\boldsymbol{v}|^2 + \Phi(r)\right), \tag{3.21}$$

only the diagonal components are non-null. For example, considering the Cartesian coordinates and $i = j = x$, the diagonal element

$$\sigma_{xx}^2 = \frac{1}{n(r)} \int \mathrm{d}v_z \mathrm{d}v_y \int \mathrm{d}v_x \, v_x^2 \, f\left(\frac{1}{2}(v_x^2 + v_y^2 + v_z^2) + \Phi(r)\right), \tag{3.22}$$

is not zero because the integrand is an even function of the velocities. Moreover, since f depends only on the modulus of $\boldsymbol{v}$ the integral would be the the same even in the y- and z-components, thus

$$\sigma_{xx} = \sigma_{yy} = \sigma_{zz} = \sigma. \tag{3.23}$$

Vice versa, when $i \neq j$, the integrand is an odd function of the velocities, thus $\sigma_{ij} = 0$.

Given these considerations, the velocity dispersion tensor is isotropic everywhere:

$$\sigma_{ij}^2 = \sigma^2 \delta_{ij}, \tag{3.24}$$

meaning that every system with an ergodic DF is isotropic.

For simplicity, it can be considered a spherical stellar system consisting of a single stellar population of identical stars, with mass $m_\star$. Under this assumption, the mass density ρ is simply proportional to $n(r)$ via $\rho = m_\star n$. If the system is also self-consistent, i.e. the density generates the potential through the Poisson equation

$$\boldsymbol{\nabla}^2 \Phi(\boldsymbol{x}) = 4\pi\rho(\boldsymbol{x}), \tag{3.25}$$

then the DF is unique.

It is convenient to define the relative potential

$$\Psi \equiv -\Phi + \Phi_0 \tag{3.26}$$

and the relative energy

$$\mathcal{E} \equiv -H + \Phi_0 = \Psi - \frac{1}{2}v^2, \tag{3.27}$$

where Φ_0 is such that $\Psi \to 0$ at infinity. It follows that $f > 0$ for $\mathcal{E} > 0$ and $f = 0$ for $\mathcal{E} \leq 0$.

Since the DF is a function of H, the Jeans theorem guarantees that the DF is also a function of $\mathcal{E}$. With these assumptions in place, it is now possible to derive an explicit expression for $f(\mathcal{E})$. Given that f depends only on the magnitude v of $\boldsymbol{v}$ and not on its direction, the integration over the angular coordinates in velocity space is reduced to a factor 4π, i.e.

$$n(\boldsymbol{x}) = \int \mathrm{d}^3\boldsymbol{v} f\left(\Psi - \frac{1}{2}v^2\right) = 4\pi \int \mathrm{d}v \, v^2 f\left(\Psi - \frac{1}{2}v^2\right) = n(\Psi). \tag{3.28}$$

Then, by changing the coordinates according to Eq. 3.27, the density can be written as

$$n(\Psi) = 4\pi \int_0^\Psi \mathrm{d}\mathcal{E} f(\mathcal{E}) \sqrt{2(\Psi - \mathcal{E})} \tag{3.29}$$

and, since Ψ is a monotonic function of r in any spherical system, it is possible to treat n as a function of Ψ rather than r, thus yielding the notation $n(\Psi)$. Differentiating both sides of Eq. 3.29 with respect to Ψ:

$$\frac{\mathrm{d}n}{\mathrm{d}\Psi} = 2\sqrt{2}\pi \int_o^\Psi \mathrm{d}\mathcal{E}\, \frac{f(\mathcal{E})}{\sqrt{\Psi - \mathcal{E}}}. \tag{3.30}$$

This is an Abel integral equation which has solution

$$f(\mathcal{E}) = \frac{1}{\sqrt{8}\pi^2} \frac{\mathrm{d}}{\mathrm{d}\mathcal{E}} \int_0^\mathcal{E} \frac{\mathrm{d}\Psi}{\sqrt{\mathcal{E} - \Psi}} \frac{\mathrm{d}n}{\mathrm{d}\Psi}, \tag{3.31}$$

commonly referred to as Eddington's formula. This formula can be generalised to systems with multiple components. Each i-th component will have its own given by

$$f_i(\mathcal{E}) = \frac{1}{\sqrt{8}\pi^2} \frac{\mathrm{d}}{\mathrm{d}\mathcal{E}} \int_0^\mathcal{E} \frac{\mathrm{d}\Psi_{\mathrm{TOT}}}{\sqrt{\mathcal{E} - \Psi_{\mathrm{TOT}}}} \frac{\mathrm{d}n_i}{\mathrm{d}\Psi_{\mathrm{TOT}}}, \tag{3.32}$$

where n_i is the density of the i-th component, while Ψ_{TOT} is the total potential given by the sum of the potentials of all the components.

However, only a handful of models have an analytical DF. The next paragraphs present some spherical models with analytic density and DF.

Plummer model The Plummer (1911) profile has already been introduced in § 1.2 in terms of the luminosity profile. By assuming a constant stellar mass-to-light ratio, the Plummer profile can be expressed in terms of the mass density distribution as follows:

$$\rho(r) = \frac{3M_{\mathrm{TOT}}}{4\pi R_s^3} \left(1 + \frac{r^2}{R_s^2}\right)^{-5/2}, \tag{3.33}$$

where M_{TOT} is the total mass of the system, and R_s is the same as in Eq. 1.6. The corresponding DF is

$$f(\mathcal{E}) = \frac{24\sqrt{2}}{7\pi^3} \frac{R_s^2}{G^5 M_{\mathrm{TOT}}^4} \mathcal{E}^{7/2} \tag{3.34}$$

Dehnen models The Dehnen model is a family of models which offer a versatile framework for describing the mass distribution and gravitational potential of spherical galaxies, capturing a wide range of density profiles from steep cusps to shallow cores. The mass density profile is defined as

$$\rho(r) = \frac{(3-\gamma)M_{\mathrm{TOT}}}{4\pi} \frac{r_s}{r^\gamma \left(r + r_s\right)^{4-\gamma}}, \tag{3.35}$$

where r_s is a scale radius, M_{TOT} the total mass and γ an adimensional parameter. The DF of these models is analytical only in for some specific values of γ (Dehnen, 1993). By defining $\varepsilon = (\mathcal{E} r_s)/(G M_{\mathrm{TOT}})$, some examples are

- $\gamma = 0$

$$f(\varepsilon) = \frac{3M_{\rm TOT}}{2\pi^3 (GM_{\rm TOT} r_s)^{3/2}} \left(\sqrt{2\varepsilon} \frac{3 - 4\varepsilon}{1 - 2\varepsilon} - 3 \operatorname{asinh} \sqrt{\frac{2\varepsilon}{1 - 2\varepsilon}} \right), \tag{3.36}$$

- $\gamma = 3/2$

$$\begin{aligned} f(\varepsilon) = \frac{3M_{\rm TOT}}{2(2\pi^2 G M_{\rm TOT} r_s^{3/2})} \frac{\sqrt{\varepsilon}}{(2-\varepsilon)^4} \Bigg[& -\frac{9}{16} - \frac{99}{16}\varepsilon + \frac{405}{8}\varepsilon^2 - \frac{3705}{56}\varepsilon^3 \\ & + \frac{561}{14}\varepsilon^4 - \frac{181}{14}\varepsilon^5 + \frac{15}{7}\varepsilon^6 - \frac{\varepsilon^7}{7} + \frac{3\,(3 + 32\varepsilon - 8\varepsilon^2)}{8\sqrt{\varepsilon(2-\varepsilon)}} \arcsin\sqrt{\frac{\varepsilon}{2}} \Bigg], \end{aligned} \tag{3.37}$$

- $\gamma = 1$, also known as Hernquist (1990) model

$$\begin{aligned} f(\varepsilon) = \frac{1}{\sqrt{2}(2\pi)^3 (GM_{\rm TOT} r_s)^{3/2}} \frac{\sqrt{\varepsilon}}{(1-\varepsilon)^2} \Bigg[& (1 - 2\varepsilon)(8\varepsilon^2 - 8\varepsilon - 3) + \\ & \frac{3 \arcsin(\sqrt{\varepsilon})}{\sqrt{\varepsilon(1-\varepsilon)}} \Bigg]. \end{aligned} \tag{3.38}$$

Isochrone model The isochrone potential uniquely allows for all stellar orbits to be described analytically, making it a rare and valuable model in galactic dynamics. Its density profile is

$$\rho(r) = M_{\rm TOT} \left[\frac{3r_s^2 (r_s + a) - r^2 (r_s + 3a)}{4\pi a^3 (r_s + a)^3} \right], \tag{3.39}$$

where r_s is a scale radius and $a \equiv \sqrt{r^2 + r_s^2}$.

$$\begin{aligned} f(\varepsilon) = \frac{1}{\sqrt{2}(2\pi)^3 (GM_{\rm TOT} r_s)^{3/2}} \frac{\sqrt{\varepsilon}}{[2(1-\varepsilon)]^4} \Bigg[& 27 - 66\varepsilon + 320\varepsilon^2 - 240\varepsilon^3 \\ & + 64\varepsilon^4 + 3\left(16\varepsilon^2 + 28\varepsilon - 9\right) \frac{\arcsin(\sqrt{\varepsilon})}{\sqrt{\varepsilon(1-\varepsilon)}} \Bigg], \end{aligned} \tag{3.40}$$

where again $\varepsilon = (\mathcal{E} r_s)/(GM_{\rm TOT})$.

3.3 Jeans equations

An alternative method to gain insights into the solution of the collisionless Boltzmann equation involves calculating the moments of the equation, leading to the so-called Jeans equation.

The first Jeans equation is derived by calculating the zero-order moment of Eq. 3.15, thus by integrating it over all the velocities:

$$\int \mathrm{d}^3\boldsymbol{v}\, \frac{\partial f}{\partial t} + \int \mathrm{d}^3\boldsymbol{v}\, v_i \frac{\partial f}{\partial x_i} - \frac{\partial \Phi}{\partial x_i} \int \mathrm{d}^3\boldsymbol{v}\, \frac{\partial f}{\partial v_i} = 0 \tag{3.41}$$

This equation can be simplified by considering that

- in the first term, the integration domain does not depend on time, thus $\partial/\partial t$ can be taken outside the integral;
- in the second term, v_i does not depend on x_i, so $\partial/\partial x_i$ can be taken outside the integral;
- the last term vanishes on application of the divergence theorem, given that $f(\boldsymbol{x}, \boldsymbol{v}, t) = 0$ for sufficiently large $|\boldsymbol{v}|$, because there are no stars that move infinitely fast.

Therefore, using the definitions of n and $\bar{v}$ given in Eq. 3.7 and Eq. 3.8, respectively, Eq. 3.41 becomes

$$\frac{\partial n}{\partial t} + \frac{\partial \left(n\bar{v}_k\right)}{\partial x_k} = 0 \tag{3.42}$$

which describes the conservation of the number density distribution $n(\boldsymbol{x}, t)$.

For each i-th component of the velocity $\boldsymbol{v}$, the second Jeans equation can be derived from the first-order moment of the collisionless Boltzmann equation, i.e. multiplying Eq. 3.15 by v_i and integrating it over all velocities,

$$\frac{\partial}{\partial t}\int \mathrm{d}^3\boldsymbol{v}\, v_i f + \int \mathrm{d}^3\boldsymbol{v}\, v_i v_j \frac{\partial f}{\partial x_j} - \frac{\partial \Phi}{\partial x_j}\int \mathrm{d}^3\boldsymbol{v}\, v_i \frac{\partial f}{\partial v_j} = 0. \tag{3.43}$$

The last term on the left-hand side can be transformed by applying the divergence theorem, and using the fact that f vanishes for large $|\boldsymbol{v}|$:

$$\int \mathrm{d}^3\boldsymbol{v}\, v_i \frac{\partial f}{\partial v_i} = -\int \mathrm{d}^3\boldsymbol{v} \frac{\partial v_i}{\partial v_j} f = -\int \mathrm{d}^3\boldsymbol{v} \delta_{ij} f = -n\delta_{ij}. \tag{3.44}$$

This allows us to rewrite Eq. 3.43 as

$$\frac{\partial \left(n\bar{v}_i\right)}{\partial t} + \frac{\partial \left(n\overline{v_i v_j}\right)}{\partial x_i} - n\frac{\partial \Phi}{\partial x_j} = 0. \tag{3.45}$$

The last step consists in subtracting v_i times the continuity equation (Eq. 3.42) and using Eq. 3.11 to eliminate $\overline{v_i v_j}$. The second Jeans equation is then:

$$n\frac{\partial \bar{v}_i}{\partial t} + n\bar{v}_j \frac{\partial \bar{v}_i}{\partial x_j} = -n\frac{\partial \Phi}{\partial x_i} - \frac{\partial (n\sigma_{ij}^2)}{\partial x_i}, \tag{3.46}$$

which has the same form as the Euler equation of fluid dynamics, with the difference that the fluid mass is substituted by stellar number density, and the stream velocity by the mean velocity of stars. A consequence of this analogy is that the last term on the right-hand side of Eq. 3.46 represents a collisionless analogue to the pressure force $-\boldsymbol{\nabla} p$. Therefore, $n\sigma_{ik}^2$ is a stress tensor that describes an anisotropic pressure.

However, the Jeans equations are not a closed set of equations, as the number of independent functions is greater than the number of available equations. For example, if the potential Φ and the density DF $n(\boldsymbol{x}, t)$ are known, there are nine other unknown quantities: six independent elements of the velocity dispersion tensor σ_{ij}^2, three components of the mean velocity $\overline{\boldsymbol{v}}$, but four equations only. In practice, the difficulty can be mitigated

by making some assumptions about the form of the tensor $\boldsymbol{\sigma}^2$ or the symmetries of the system, as illustrated in the following section.

3.3.1 Spherical systems

Assuming spherical symmetry also reduces the degrees of freedom in the problem and allows us to close the set of Jeans equations. For spherical systems, it can be proved that the DF depends on the magnitude of angular momentum and total energy only. Thus, for stationary systems,

$$n\frac{\partial \overline{v}_i}{\partial t} = 0, \tag{3.47}$$

Eq. 3.46 takes a simple form in spherical coordinates (r, θ, ϕ):

$$\frac{\mathrm{d}\left(n\overline{v_r^2}\right)}{\mathrm{d}r} + n\left(\frac{\mathrm{d}\Phi}{\mathrm{d}r} + \frac{2\overline{v_r^2} - \overline{v_\theta^2} - \overline{v_\phi^2}}{r}\right) = 0 \tag{3.48}$$

It can then be introduced the anisotropy parameter

$$\beta \equiv 1 - \frac{\overline{v_\theta^2} + \overline{v_\phi^2}}{2\overline{v_r^2}}, \tag{3.49}$$

which measures the level of anisotropy of the galaxy, and by definition $-\infty < \beta \leq 1$. In particular, if $\beta = 0$ the system is isotropic, if $\beta > 0$ it is said to be radially biased, otherwise it is tangentially biased. Rearranging for the introduction of β, Eq. 3.48 becomes

$$\frac{\mathrm{d}(n\overline{v_r^2})}{\mathrm{d}r} + 2\frac{\beta}{r}n\overline{v_r^2} = -n\frac{\mathrm{d}\Phi}{\mathrm{d}r} \tag{3.50}$$

This last equation has an explicit solution:

$$n\sigma_r^2(r) = \frac{1}{h(r)}\int_r^\infty \mathrm{d}r'\, h(r')n(r')\frac{\mathrm{d}\Phi}{\mathrm{d}r} \tag{3.51}$$

where $h(r) = \exp\int_r^\infty \mathrm{d}r'\,\beta/r$, that gives the radial velocity dispersion. However, the latter is not directly observable. Instead, what is typically measured is the l.o.s. velocity dispersion, which can be derived by projecting $\sigma_r^2(r)$ along the l.o.s. The weakness of this approach is the lack of information on the anisotropy parameter, in addition to the fact that different combinations of mass and anisotropy profiles give the same solution to Eq. 3.51. The latter is the so-called mass-anisotropy degeneracy of stellar systems. In principle, both the mass distribution and the anisotropy of stellar velocities influence the observable kinematics, and in particular the velocity dispersion profile. However, these two factors can produce similar effects, making it difficult to uniquely infer either one from the data alone. For example, a system with a concentrated mass profile may produce the same velocity dispersion as a system with a more extended mass distribution but significant radial velocity anisotropy.

IV

Creation of Initial Conditions

This chapter aims to provide a comprehensive understanding of the processes involved in preparing for N-body simulations, laying the groundwork for the subsequent simulation that will involve interactions between Sextans and a smaller satellite. In particular, I will detail the procedure for the creation of initial conditions for N-body simulations tailored for the hydrodynamical N-body code Arepo, a state-of-the-art code that has been extensively employed to deal with a large number of astrophysical problems.

In § 4.1 it will be given an introduction to the Arepo code, including its key algorithms for resolving hydrodynamical and gravitational interactions. This section will briefly discuss also the advantages of Arepo's design, such as its scalability and computational efficiency, which enable it to handle a wide range of astrophysical phenomena.

Then, § 4.2 will describe in detail the scheme adopted to create initial conditions for the simulations, by outlining the algorithms employed to sample the distribution functions that define the phase-space distribution of the particles representing the simulated systems. Next, in § 4.2.1, it will be shown the consistency checks ensured that the generated initial conditions aligned with the theoretical models used. This validation is essential to guarantee that the simulations are based on realistic parameters and structures. Finally, § 4.2.3 it will be verified that the created systems are in a steady state, by verifying that their global properties remain stable over time.

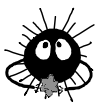

4.1 Arepo

All the simulations in this thesis have been performed using the N-body, hydrodynamic code Arepo (Springel, 2010), as implemented in its publicly released version (Weinberger et al., 2020). Arepo has been widely employed to deal with a large number of astrophysical problems thanks to its efficiency in treating both gravitational and hydrodynamical interactions in a massively parallel framework. At present, a variety of simulations run on Arepo, such as large volume cosmological simulations of galaxy formation, as the latest IllustrisTNG simulations (Pillepich et al., 2017; Nelson et al., 2018; Springel et al., 2018; Naiman et al., 2018; Marinacci et al., 2018), zoom-in cosmological magneto-hydrodynamical simulation (Grand et al., 2017), high resolution of galaxy mergers (Pascale et al., 2021, 2022, 2024) or even simulations of active galactic nuclei winds and feedback (Costa et al., 2020).

In these next paragraphs, it will be briefly explained the algorithms implemented in Arepo to solve gravity interactions and follow gas evolution.

Hydrodynamics Typically, numerical hydrodynamics solvers are either Eulerian or Lagrangian. Eulerian schemes employ a fixed mesh whose cells exchange conserved fluid properties. Lagrangian schemes, instead, sample the gas with particles and follow them in time, adapting to their clustering. Arepo uses a hybrid approach by combining the mesh of Eulerian scheme with the spatial adaptability of Lagrangian methods. In Arepo, the mesh is not fixed or structured like in traditional Eulerian methods. Instead, it is defined dynamically through a Voronoi tessellation, which divides space into cells around each particle. These cells adjust their shape and size as the gas particles move, allowing the mesh to naturally adapt to the fluid's flow. This dynamic adjustment prevents issues like cell distortion or tangling, which can occur in conventional grid-based methods.

Gravity Solving the gravitational interactions in an N-body problem essentially involves calculating the gravitational potential ϕ at a point $\boldsymbol{x}$ generated by N particles:

$$\Phi(\boldsymbol{x}) = -G \sum_{i=1}^{N} \frac{m_i}{\sqrt{(\boldsymbol{x} - \boldsymbol{x}_i)^2 + \varepsilon^2}} \tag{4.1}$$

where $\boldsymbol{x}_i$ is the position of the i-th particle, m_i its mass and ε is the so-called softening length. The softening length is a parameter used to dampen Φ at short range in order to ensure the collisionless behaviour of the N particles and avoid particle pair interactions. In principle, interactions between N particles can be calculated analytically by individually summing over each pair of particles. However, for N particles this would require a number of operations of order N^2, which is computationally expensive for large values of N as usually happens in N-body simulations. Therefore, approximate methods are employed to speed up gravity-related calculations.

One of these methods is the tree method (Barnes and Hut, 1986), also known as the hierarchical multipole method. A tree method approximates distant groups of particles through their multipole expansion, instead of considering individual interactions between

particles in a group and a particle positioned at $\boldsymbol{x}$. Such groups can be represented by nodes of an oct-tree (Barnes and Hut, 1986) allowing to follow the clustering of matter by creating smaller and smaller nodes. Thanks to this approximation, this method reduces the number of operations to $N \log N$. On the other hand, the tree method is unable to efficiently handle almost homogeneous matter distributions, since in this case, the very small force acting on a particle is the sum of many partial contributions from other particles and nodes, so obtaining accurate results becomes computationally expensive.

The particle-mesh (PM) method (Klypin and Shandarin, 1983; Frenk et al., 1983), instead, solves the Poisson equation $\boldsymbol{\nabla}^2\Phi = 4\pi G\rho$, where ρ is the matter density, via the Green function of the Laplacian operator $\boldsymbol{\nabla}^2$, $g(\boldsymbol{x} - \boldsymbol{y})$. In this specific case, the Green function yields the following convolution

$$\Phi(\boldsymbol{x}) = 4\pi G \int \mathrm{d}^3\boldsymbol{y}\, \rho(\boldsymbol{y}) g(\boldsymbol{x} - \boldsymbol{y}). \tag{4.2}$$

Using the convolution theorem in Fourier space, the equation for the Fourier transform of Φ reduces to a multiplication of the Fourier transform of ρ and g. To build the density field ρ, the method distributes the mass of the N-particles among cells of fixed mesh, therefore it lacks the resolution adaptability of the tree method. The main advantage of the particle-mesh method is that its cost scales almost linearly with the number of particles, i.e. $\propto N$ plus the cost of the Fourier transform[†].

Given the complementary strengths of these methods, Arepo employs a combination of the two, splitting the potential into long and short-range components which are then calculated via tree and PM methods, respectively.

4.2 Set up for the simulations

Running a N-body simulation requires setting the initial conditions (ICs) for samples of N particles, representing all the systems involved, each with their own mass, initial position $\boldsymbol{x}_i$ and initial velocity $\boldsymbol{v}_i$, with $i = 1 \dots N$. Specifically, since the aim of the simulations in this thesis is to reproduce the observed peculiar features in Sextans, as the result of a merger between Sextans and a smaller companion, it is mandatory that both systems are represented in the simulations with realistic sets of particles.

By definition of dSph, see § 1.1, Sextans lacks gas, thus its only components are stars and DM, which are, de facto, non-collisional. Moreover, in § 1.3, it was illustrated that dSphs are typically pressure-supported systems with little to no velocity gradients or sign of systemic rotation. Also, tidal interactions with the MW have had negligible effects on the internal kinematics, thus the galaxy can be assumed stationary and isolated. For these reasons, Sextans is modelled as a completely non-collisional steady-state ergodic system, that for simplicity will be assumed spherically symmetric.

[†] The Fourier transform of field on a discretised grid of $\mathcal{N}$ cells through a direct summation scales with $\mathcal{N}$ (Springel, 2016). Nowadays, numerical Fourier transforms are calculated through the fast Fourier transform (FFT) algorithm (Cooley and Tukey, 1965), which provides both better scaling ($\propto \mathcal{N} \log \mathcal{N}$) and higher accuracy with respect to direct summation.

On this basis, I chose to model Sextans by a stellar population embedded in a dominant DM halo. The stellar component has been modelled using the Plummer profile in Eq. 3.33, because among the best-fitting models in Cicuéndez et al. (2018) it is the one that better represents the observed profile. The DM halo, instead, has been described by an NFW profile (Eq. 1.9) with an exponential cut-off that ensures that the halo has finite mass:

$$\rho(r) = \frac{\rho_0 \exp\left(-\left(\frac{r}{r_t}\right)^{\gamma}\right)}{\left(\frac{r}{r_s}\right)\left(1+\frac{r}{r_s}\right)^2}, \tag{4.3}$$

where r_t is the truncation radius, and γ is an adimensional parameter responsible for the sharpness of the cut-off, typically $\gamma = 2$.

As no morphological constraints exist for the satellite, I investigated two cases

- a satellite composed solely of a stellar component with a Plummer profile;
- a satellite with also a DM halo, i.e. a Plummer stellar component embedded in a dominant DM halo with a truncated NFW profile.

The next section will therefore explain the scheme that I adopted to generate the ICs of all the systems involved in the two types of simulations.

4.2.1 Creation of initial conditions

Any non-collisional system is described by a DF, which encapsulates the full dynamical state of the system. Once the DF is specified, it is possible to sample the particle's phase-space positions that represent the target system from the DF itself. For each component, the set of N particles, each one with phase-space coordinates $(\boldsymbol{x}_i, \boldsymbol{v}_i)$, has been created following a three-step algorithm.

1. The DF is obtained via the Eddington inversion formula Eq. 3.32. In systems with only one component, like the satellite in the simulations where it is made only of stars, ρ and Φ in the Eddington formula are simply the ones from the chosen model, linked via the Poisson Equation (Eq. 3.25). For a Plummer model, the Eddington inversion can be solved analytically and the DF is given in equation Eq. 3.34. In the two-component case, the Eddington formula yields a separate DF for each component. The density ρ_i appearing in Eq. 3.32 can be either $\rho_\star$ or $\rho_{\rm DM}$, representing the stellar and DM density profiles. Instead, Φ corresponds to the total potential of the system, which can be assumed to be generated only by the dominant component, $\Phi = \Phi_{\rm DM}$, with $\Phi_{\rm DM}$ the DM potential, or both components, $\Phi = \Phi_{\rm DM} + \Phi_\star$, with $\Phi_\star$ the stellar potential. In our case, the latter is considered.
2. Positions are assigned by sampling the model mass distribution.
3. Velocities are assigned by using the previously computed DF.

Therefore, to sample each component, it is essential that all their parameters are well-defined. These include the total mass $M_{\rm tot}$, the number of particles N, and a model for sampling. For example, in the case of the Plummer model, the scale radius r_s is required, while for a truncated NFW model, both r_s and the truncation radius r_t are necessary. Since the systems are assumed to consist of equal mass particles, to each particle is assigned the same mass m_p. This mass is calculated by dividing the total mass of the

component by the number of particles:

$$m_p = \frac{M_{\rm TOT}}{N}. \tag{4.4}$$

The procedure adopted to assign positions and velocities is explained in the following paragraphs.

Position assignment The definition of spherical coordinates is given by

$$\begin{cases} x = r\sin\theta\cos\phi \\ y = r\sin\theta\sin\phi \\ z = r\cos\theta, \end{cases} \tag{4.5}$$

where (x, y, z) are the Cartesian coordinates, $r \in [0; \infty[$, $\theta \in [0; \pi[$ and $\phi \in [0, 2\pi[$. In spherical coordinates, assigning a position to each point means creating N triplets (r, θ, ϕ). Since the system is spherically symmetric, ρ depends only on r and therefore

$$\int_0^x \mathrm{d}x \int_0^y \mathrm{d}y \int_0^z \mathrm{d}z\rho(x, y, z) = \int_0^\pi \mathrm{d}\theta \sin\theta \int_0^{2\pi} \mathrm{d}\phi \int_0^r \mathrm{d}r\, r^2\rho(r). \tag{4.6}$$

From Eq. 4.6, it is evident that the sampling of the variables r, θ and ϕ can be performed independently from one another. For a set of N particles, r must be sampled from the probability density distribution $P(r) = r^2\rho(r)\mathrm{d}r$, θ from the probability $P(\theta) = \sin\theta\mathrm{d}\theta$ and ϕ from $P(\phi) = \mathrm{d}\phi$.

To efficiently sample the radial coordinate r, I used the inverse mass function method. The method requires to compute first the cumulative probability function, which, for r, is proportional to the total mass $M(r)$, while for ϕ and $\sin\theta$ is a constant,

The cumulative probability function for r is normalised to unity, obtaining the adimensional mass parameter $q(r)$, which by definition $0 \leq q \leq 1$. Therefore, being a growing function of r, $q(r)$ can be inverted in order to obtain $r(q)$, which gives the radius as a function of q. For a Plummer model, the inversion can be performed analytically, while in the NFW case, the inversion is carried out numerically. This is achieved through linear interpolation of $r(q)$, where q is sampled on a grid of points q_i that are evenly spaced in the logarithm of the variable. Then, I sampled N values of q from a uniform distribution. The radii are then assigned simply by computing the corresponding $r(q)$ for each extracted q. For ϕ it is sufficient to extract N uniformly distributed values in $[0, 2\pi[$, while for θ I extracted N uniformly distributed values in [-1,1[and then calculated their arcsin.

Finally, the sets of spherical coordinates (r, θ, ϕ) are converted into sets of Cartesian coordinates (x, y, z) using Eq. 4.5.

Velocity assignment To assign velocities to each position $\boldsymbol{x}_i$, I employed a rejection sampling algorithm to extract the velocities from the DF at fixed positions.

In general, for a given DF $f(\boldsymbol{x}, \boldsymbol{v})$, once the position $\boldsymbol{x}_i$ is fixed, the corresponding

velocity probability function, also referred to as Velocity Distribution (VD), is

$$\mathrm{VD}(\boldsymbol{x}_i, \boldsymbol{v}) = \frac{f(\boldsymbol{x}_i, \boldsymbol{v})}{\int \mathrm{d}^3\boldsymbol{v} f(\boldsymbol{x}_i, \boldsymbol{v})} = \frac{f(\boldsymbol{x}_i, \boldsymbol{v})}{\rho(\boldsymbol{x})}. \tag{4.7}$$

To assign the velocity, it is then necessary to sample the corresponding VD for each $\boldsymbol{x}_i$ in the sample. However, unlike the position sampling method, it is not feasible to apply the same approach to velocity sampling. This is because the cumulative probability distribution of VD is not necessarily analytical. Thus, to properly compute and invert it, it would require a separate numerical integration and interpolation for each $\boldsymbol{x}_i$, making the procedure too computationally expensive. For this reason, I adopted a rejection sampling.

Recall that for a model with finite mass, such as the one considered in this thesis, the maximum velocity allowed at a fixed position $\boldsymbol{x}_i$ is the escape velocity

$$v_{\mathrm{esc}} = \sqrt{-2\Phi(\boldsymbol{x}_i)}. \tag{4.8}$$

Thus, the sampling in the velocity space proceeds as follows. First, for each position $\boldsymbol{x}_i$, I sample three velocities from a uniform distribution within $[0, v_{\mathrm{esc}}]$. These three numbers are the components of the test velocity $\boldsymbol{v}_{\mathrm{temp}}$. Another number k is sampled from a uniform distribution in the range $[0, f_{\mathrm{max}}]$, with f_{max} the value that maximises the entire $\mathrm{VD}(\boldsymbol{x}_i, \boldsymbol{v})$. For a steady state, spherical, isotropic system, this value is $f_{\mathrm{max}} = \mathrm{VD}(\boldsymbol{x}_i, 0)$. The velocity $\boldsymbol{v}_{\mathrm{temp}}$ is accepted as velocity at x_i only if $k < \mathrm{VD}(\boldsymbol{x}_i, \boldsymbol{v}_{\mathrm{temp}})$ and $|\boldsymbol{v}_{\mathrm{temp}}| \leq v_{\mathrm{esc}}$. If $k > \mathrm{VD}(\boldsymbol{x}_i, \boldsymbol{v}_{\mathrm{temp}})$, $\boldsymbol{v}_{\mathrm{temp}}$ is rejected and the procedure is re-iterated.

4.2.2 Check of the initial conditions

For each component, either stars or DM, I tested if the positions and velocities have been correctly sampled by comparing the morphological and kinematic properties of the N-body samples with the ones predicted by their corresponding models.

In particular, to check the accuracy of the position generation, I compared the mass density profile of the generated sample with the theoretical one. The mass density profiles of the particles depend only on their spatial distribution, since all of them, by hypothesis, have the same mass $m_p = M_{\mathrm{TOT}}/N$. Furthermore, since the system is spherically symmetric, the only relevant coordinate is the radial one. I then calculated the radial distance for each set of generated Cartesian coordinates and divided these into $\mathcal{N}$ radial bins, representing spherical shells. The total mass in each i-th bin, M_i, is determined by multiplying the number of particles in that bin, $N_{\mathrm{counts},i}$, by the mass of each particle, m_p. Therefore, the mass density in each bin i is estimated as

$$\rho_i = \frac{M_i}{V_i} = \frac{m_p N_{\mathrm{counts,\ i}}}{\frac{4\pi}{3}\left(r_i^3 - r_{i-1}^3\right)} \tag{4.9}$$

where the denominator is the volume of the spherical shell as a function of its limiting

radii r_i and r_{i-1}. To each ρ_i, I assigned a Poissonian error equal to

$$\delta\rho_i = \frac{m_p\sqrt{N_{\text{counts, i}}}}{\frac{4\pi}{3}\left(r_i^3 - r_{i-1}^3\right)} \tag{4.10}$$

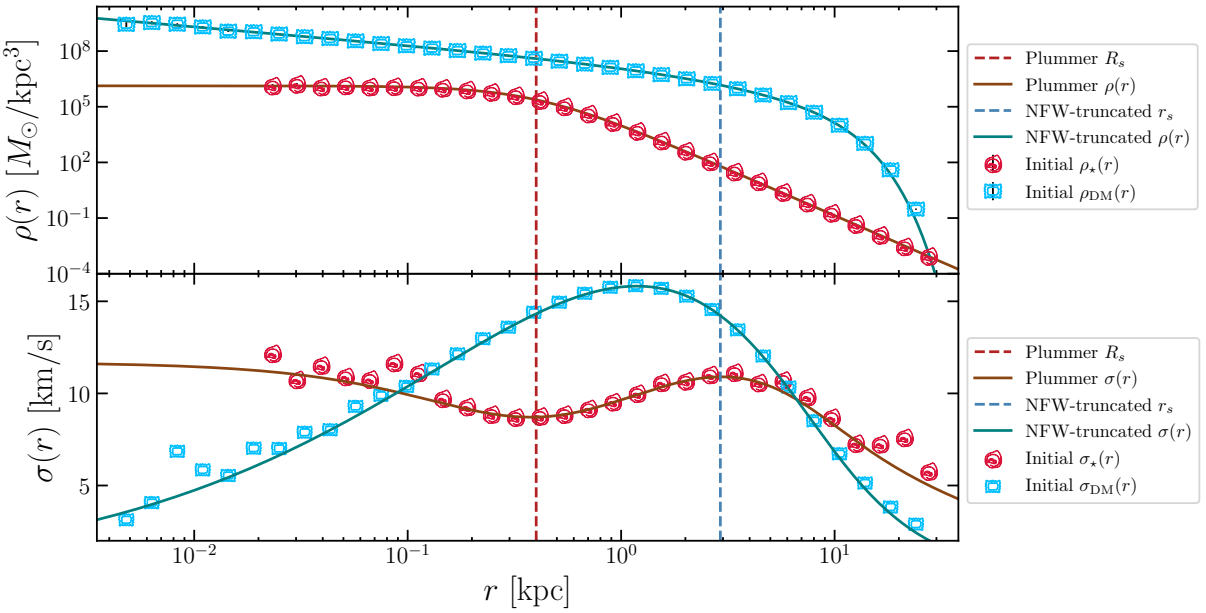

Fig. 4.1 – Upper panel: mass densities of the generated Plummer component (red tortellini, PASTA Collaboration et al., 2024), the theoretical Plummer model (red line), the generated truncated-NFW halo (blue ravioli) and the theoretical truncated-NFW model (blue line). Lower panel: velocity dispersions of the generated Plummer component (red tortellini), the theoretical Plummer model (red line), the generated truncated-NFW halo (blue ravioli) and the theoretical truncated-NFW model (blue line).

To check the accuracy of the velocities generation, I compared the velocity dispersion profiles of the generated samples with the theoretical ones, calculated using Eq. 3.51, in the case $\beta = 0$ since the system is isotropic. Notice that, in the formula, the density ρ refers to the target component (stars or DM), while Φ is the total potential (stars and DM) of the system, analogously to the Eddington formula. Moreover, the isotropy condition (see Eq. 3.23) ensures that the velocity dispersion is the same along all Cartesian directions and, therefore, it can be computed along only one direction. Relying again on the spherical symmetry of the system, I used the same radial binning and calculated the velocity dispersion of the i-th bin, σ_i as the standard deviation of the velocities of the particles m that fell into the bin, i.e.

$$\sigma_i = \sqrt{\frac{\sum_m |v_m - \overline{v_i}|^2}{N_{\text{counts, i}}}}, \tag{4.11}$$

where $\overline{v_i}$ is the average velocity in the bin and $N_{\text{counts, i}}$ the number of particles in the bin.

The results are displayed in Figure 4.1 for the case of a stellar component described by a Plummer profile embedded in a truncated NFW DM halo. The upper panel shows

the mass density distributions of the generated samples (markers) and the theoretical model (continuous lines). The lower panel shows the velocity dispersion profiles of the generated samples (markers) and the theoretical model (continuous lines). In both cases, the profiles derived from the N-body samples closely match the theoretical predictions, accurately reproducing the expected mass density and velocity dispersion distributions.

4.2.3 Check of the steady-state condition

The final requirement is to verify that the generated systems are in a steady state, meaning their global properties must remain stable over time. Specifically, the mass density and velocity profiles of the samples should consistently align with the theoretical ones.

To verify this, I evolved the generated systems in isolation using the Arepo code, where the only forces involved are the gravitational interactions among the particles themselves. Additionally, I examined how varying the number of particles impacts the simulation's timescales and the system's stability over time. Given a fixed value of the total DM mass, increasing the mass of individual DM particles reduces their total number, which in turn speeds up the simulation by decreasing the number of computations required. However, if the mass ratio between stellar and DM particles becomes too low, it can cause the formation of binary systems, leading to artificial heating and compromising the stability of the system.

	Stars	DM
Model	Plummer	Truncated NFW
M [$M_\odot$]	3.6×10^5	9.7×10^8
R_s [kpc]	0.4	–
r_s [kpc]	–	2.9
r_t [kpc]	–	7

Tab. 4.1 – Summary of the structural parameters for each Sextans component in the simulations. Stars follow a Plummer profile (Eq. 3.33), while the DM follows a truncated NFW profile (Eq. 4.3). From the top, the table lists the total mass M of the component, the Plummer scale radius R_s for the stars, and the scale radius r_s and truncation radius r_t for the DM halo.

To resemble Sextans, the structural parameters in Tab. 4.1 have been chosen in accordance to §§ 2. However, in the simulation, Sextans was truncated at 7 kpc. This decision, discussed further and more quantitatively in § 5.1, is justified by the fact that most of the observed peculiar features in the galaxy are concentrated in its central regions, making the outer areas not relevant for the purpose of this study. Additionally, by removing the outer regions, the resolution in the central regions improves, as the same number of particles have been used to sample a smaller volume, allowing for a more detailed representation of the inner dynamics and providing better insight into the phenomena occurring in the core of Sextans. Moreover, in § 2.2.2 it was shown that the stars belonging to the ring-like structure were 20% of the total stars in the same. I decided to adopt approximately the same ratio for the Sextans and the accreted satellite's stellar mass, resulting in the Sextans-like system having around 80% of the observationally inferred $4.4 \times 10^5 M_\odot$.

	Stars	DM		
		$q_p = 3$	$q_p = 10$	$q_p = 20$
Npts	74472	6591014	9977305	988652
$m_p\,[M_\odot]$	4.8	14.4	48	96
$t_{\rm CPU}$ [h]		4200	1176	504

Tab. 4.2 – Configurations of different test simulations. Npts is the number of particles, m_p is the particle mass and $t_{\rm CPU}$ are the core hours.

The number of stellar particles was determined based on considerations regarding the softening length ε, by following the findings of Merritt (1996) who showed that an optimal choice for its value scales with $N^{1/3}$. For a bound system of $N_{\rm part}$ particles, this scaling is typically estimated as

$$\varepsilon = r_{\rm half}\left(\frac{8\pi}{3N_{\rm part}}\right)^{1/3} \tag{4.12}$$

where $r_{\rm half}$ is the 3D half-mass radius. Using this approach, I calculated the number of stellar particles by ensuring that the softening length, $\varepsilon_\star$, for the stellar components of both Sextans and the satellite is at least one order of magnitude smaller than the size of the observed substructures. This choice ensures that the accreted satellite system is sufficiently well sampled by several resolution elements. If the softening is too large with respect to the clump size, it risks approximating the satellite as a single, smooth entity rather than resolving its internal features and dynamics, which, instead, is central to the goals of this thesis. Therefore, $\varepsilon_\star$ was chosen by considering that the observed clump in § 2.2.1 had a radius of approximately 80 pc, thus we require $\epsilon < 80/10$. The number of particles required, as reported in the first column of Tab. 4.2, was calculated from Eq. 4.12. The numbers of DM particles, instead, were calculated by dividing the DM total mass $M_{\rm DM}$ by the mass $m_{p,\rm DM}$ of the particles. To balance the need for high-resolution simulations with computational efficiency, I tested different particle mass ratios, $q_p = m_{p,\rm DM}/m_{p,\star}$, the results are reported in the second, third and fourth column of Tab. 4.2. Increasing the value of $m_{p,\rm DM}$, while maintaining the same $M_{\rm TOT,\,DM}$, results in a reduction in the number of DM particles. This decrease leads to shorter computational times, but it may also induce the formation of artificial binary systems, which could alter the characteristics of the galaxy. The computational time is usually quantified in terms of the core hours, which are calculated by multiplying the number of CPUs used (#CPU) by the wall-clock time of the simulation $t_{\rm run}$:

$$t_{\rm CPU} = \#{\rm CPU} \times t_{\rm run}. \tag{4.13}$$

This value provides a clear measure of the computational cost associated with evolving the system. The last row of Tab. 4.2 shows the core hours required to evolve the system in isolation for 3 Gyr.

The first particle mass ratio I examined was $q_p = 3$, which corresponds to $N = 6591014$ particles of mass $m_p = 14.4 M_\odot$. Figure 4.2 shows the ρ and σ profiles of the generated sample (markers) for both components at different time steps over a 3 Gyr simulation. For each component, the continuous lines represent the theoretical profiles from the selected

models and the coloured bands highlight the scales smaller than the softening length. The image clearly demonstrates that both the mass density and velocity dispersion profiles remain unchanged over time, confirming that the systems are indeed in a steady state. However, the $q_p = 3$ is extremely computationally expensive as it required $t_{\rm CPU} \approx 4200$ h.

I then examined the case $q_p = 10$, in Figure 4.3, and $q_p = 20$, in Figure 4.4. For $q_p = 10$, the DM component was composed of $N = 9977305$ particles of mass $m_{p,DM} = 48\,M_\odot$, resulting in $t_{\rm CPU}$=1176 h to simulate the evolution over 3 Gyr. Conversely, for $q_p = 20$, instead, the DM component was composed of $N = 988652$ particles of mass $m_{p,DM} = 96 M_\odot$, leading to an even shorter computational time $t_{\rm CPU}$=504 h for the same 3 Gyr simulations. In both cases, the generated sample remained consistent with the theoretical models, even up to 10 Gyr.

Given the reduced computational cost associated with the $q_p = 20$ system, I chose this configuration to represent the Sextans-like system for the simulations. This decision allows for a more efficient exploration of the system's dynamics while maintaining the necessary resolution and accuracy in the modelling.

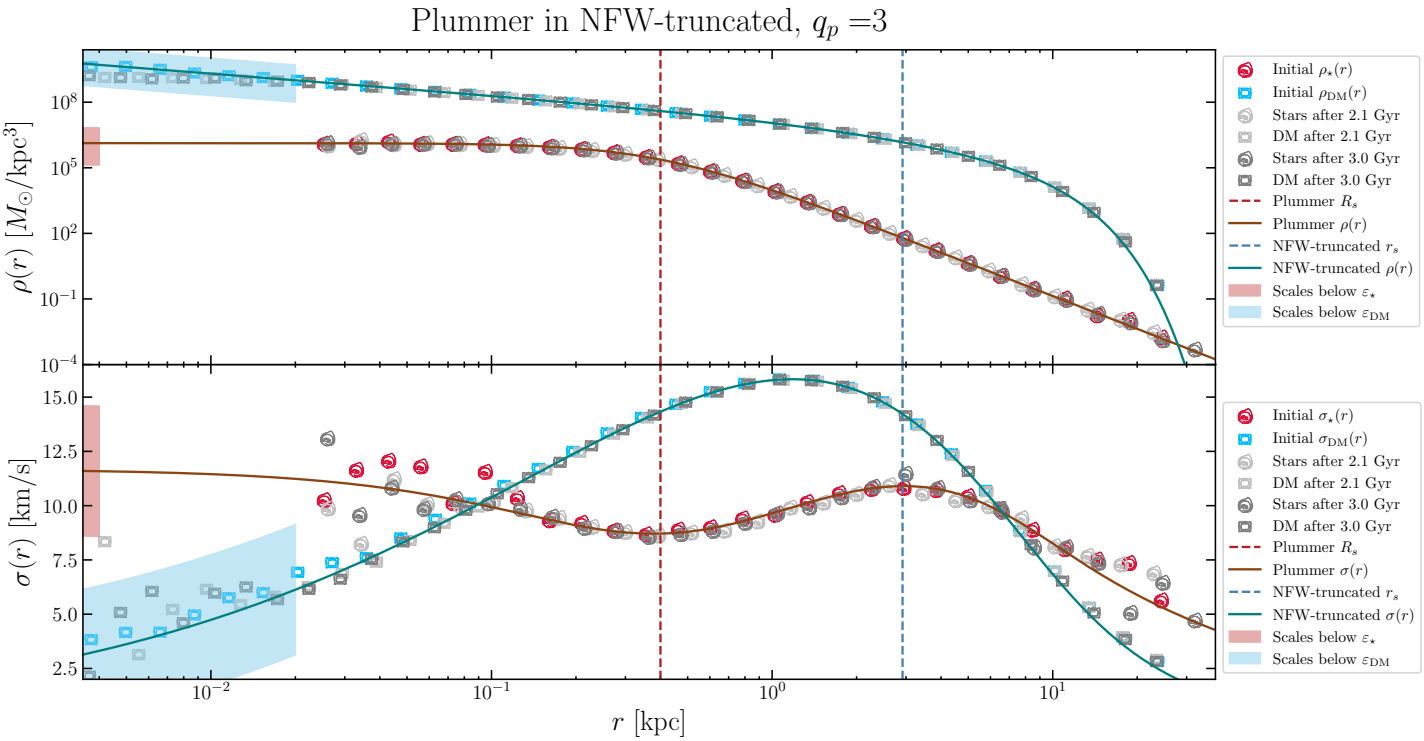

Fig. 4.2 – Characteristic profiles of a system composed of DM and stellar particles with $q_p = 3$ during the evolution in isolation for 3 Gyr. Upper panel: mass densities of the generated Plummer component (red tortellini for the IC, grey tortellini for successive timesteps), the theoretical Plummer model (red line), the generated truncated-NFW halo (blue ravioli for the IC, grey ravioli for successive timesteps) and the theoretical truncated-NFW model (blue line). Lower panel: velocity dispersions of the generated Plummer component (red tortellini for the IC, grey tortellini for successive timesteps), the theoretical Plummer model (red line), the generated truncated-NFW halo (blue ravioli for the IC, grey ravioli for successive timesteps) and the theoretical truncated-NFW model (blue line). In both panels, the red band marks the scales for the stars particles smaller than the stars softening length, while the blue band the scales for the DM particles smaller than the DM softening length.

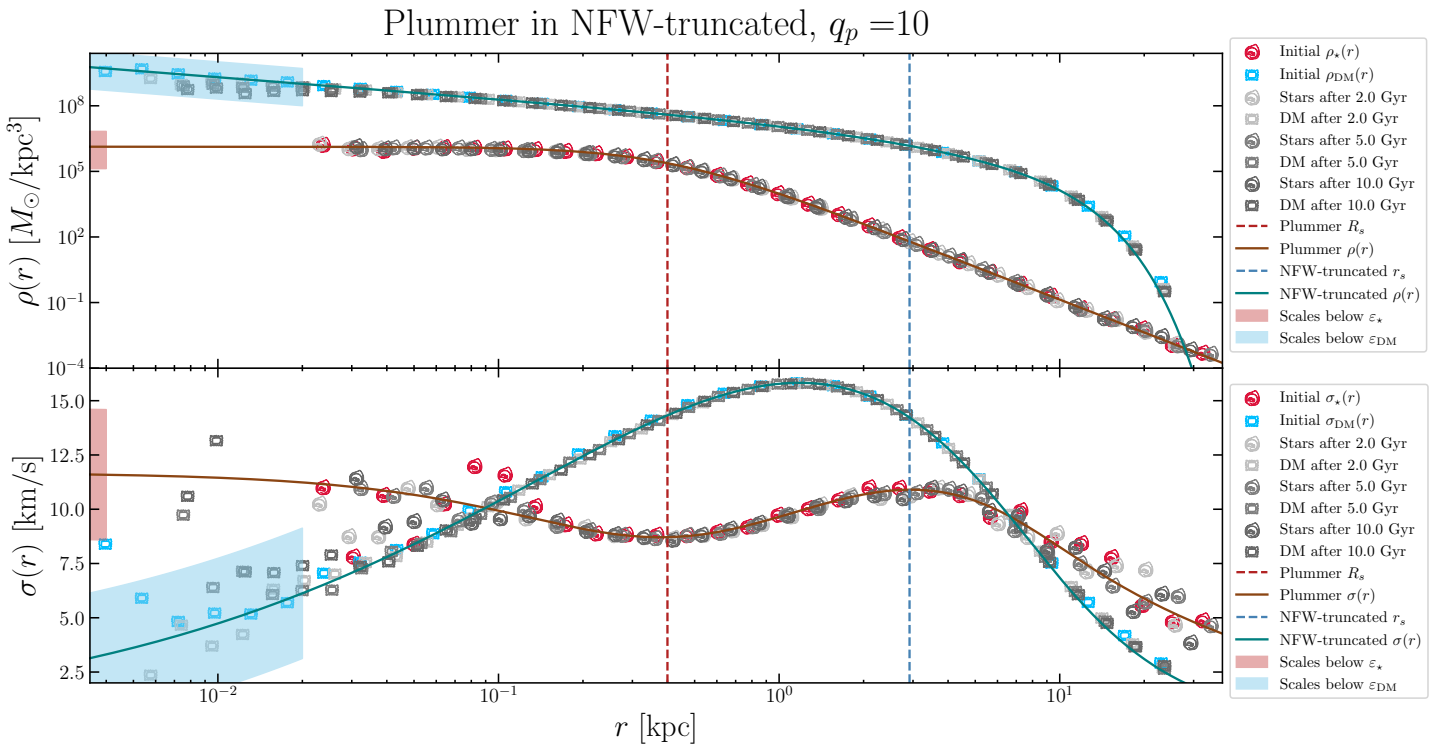

Fig. 4.3 – Same as Figure 4.2, but for $q_p = 10$ and evolved in isolation for 10 Gyr.

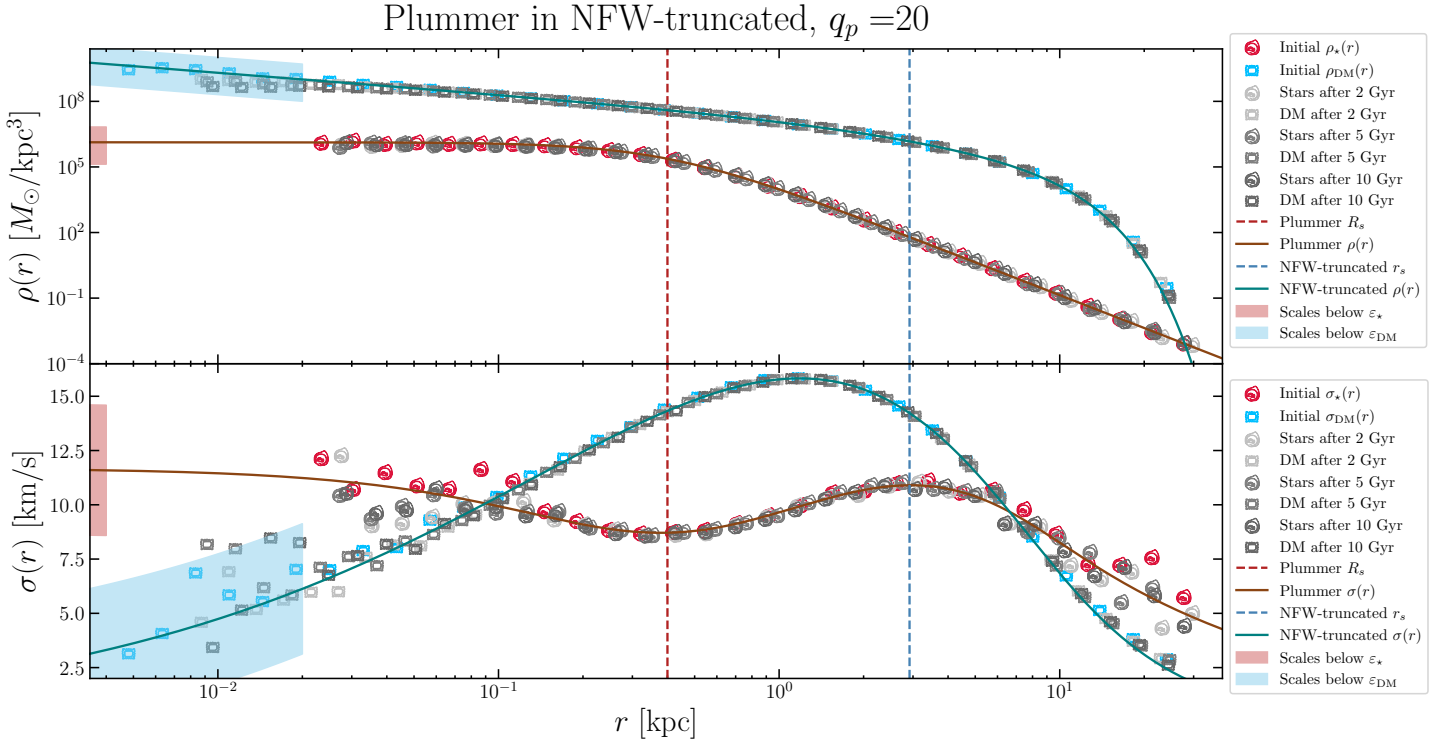

Fig. 4.4 – Same as Figure 4.2, but for $q_p = 20$ and evolved in isolation for 10 Gyr.

V

Simulations with a Satellite Composed only of Stars

In this chapter, I will delve into the results of the simulations and I will explore whether the observed velocity map in the field of Sextans can be reproduced through a minor merger event involving a satellite composed solely of stars, which is intended to represent a disrupted nuclear star cluster.

In particular, in § 5.1, I will describe the properties of the satellite, including its initial conditions, and discuss the typical timescales involved in the evolution of the system.

Primarily, in § 5.2 I will analyse the extreme scenario of a satellite initially put in a circular orbit near the centre of Sextans, to test whether the observed features could be consistent with a rotating object moving in the very centre. I will also describe the method used to create mock datasets, allowing for a direct comparison between simulation snapshots and observations.

In § 5.3 and § 5.4, I will examine physically motivated scenarios where the satellite system approaches Sextans from its outskirts, considering both cases of a small and a higher initial velocity. Ultimately, I will show that both these scenarios fail to replicate the observed features in Sextans, which suggests that a satellite without a dark matter halo is not a viable explanation.

5.1 General considerations

In this chapter, the satellite is modelled as a single-component system consisting of a spherical Plummer stellar population. All parameters are listed in Tab. 5.1. The stellar mass of the satellite, which in this case represents its total mass $M_{\rm Sat}$, was constrained by Cicuéndez and Battaglia (2018). As discussed in § 2.2.2, the authors estimated that around 20% of the stars in their sample were part of the observed ring-like structure. Based on this consideration, I assigned the satellite approximately 30% of the inferred Sextans stellar mass, slightly more than the 20% attributed to the ring. This accounts for the fact that during the interaction, a fraction of the stellar mass of the satellite can be lost in the outskirts of Sextans due to tidal forces exerted by the host galaxy, meaning that not all the mass would have ended up in the central region observed by Cicuéndez and Battaglia (2018). The parameter q is the merger mass ratio, which is the ratio between the total mass of the satellite and the total mass of Sextans $M_{\rm Sext}$ in the simulation:

$$q = \frac{M_{\rm Sat}}{M_{\rm Sext}}. \tag{5.1}$$

The number of satellite particles Npts was calculated from $M_{\rm Sat}$ by ensuring the mass of each stellar particle of the satellite matched the stellar particle mass in the Sextans-like system. Finally, the scale radius, r_s, was chosen based on the results from Kim et al. (2019), which showed that the roundish overdensity extends to approximately 80 pc in radius, thus I fixed $R_s = 40$ pc.

	Stars
Model	Plummer
$M\ [M_\odot]$	1.2×10^5
R_s [kpc]	0.04
Npts	25000
$m_p\ [M_\odot]$	4.8
q	0.0001

Tab. 5.1 – Satellite parameters in the simulations where the satellite is composed only of stars with a Plummer profile (Eq. 3.33). M is the total stellar mass, R_s is the Plummer scale radius, Npts is the number of particles that constitute the satellite, m_p is the mass of each particle, and q is the merger mass ratio.

I then investigated how to assign physically motivated orbital ICs to the satellite. In this context, two characteristic timescales for simulations determine the physical processes involved:

- the orbital period $t_{\rm orbit}$, which is the time it takes an object to complete one full orbit around another object. In this case, it is the time taken by the satellite to orbit around its host galaxy;
- the timescale of dynamical friction $t_{\rm fric}$, which refers to the loss of momentum and kinetic energy experienced by a moving body due to gravitational interactions with surrounding matter in space.

To estimate these timescales I considered a simplified version of the Sextans+Satellite system. The satellite is treated as a point mass with $M_{\rm sat}$ as total mass, moving within the smooth gravitational potential $\Phi(r)$ generated by the DM halo of Sextans, modelled by NFW profile (Eq. 2.3), with the parameters from the last row of Tab. 2.3. Then, to find the orbital period it is necessary to solve the equation of motion:

$$\begin{cases} \dot{\boldsymbol{x}} = \boldsymbol{v} \\ \dot{\boldsymbol{v}} = -\boldsymbol{\nabla}\Phi(\boldsymbol{x}) \end{cases}. \tag{5.2}$$

However, this two-body problem cannot be solved analytically because the potential depends on r, making the problem dependent on the satellite's changing position as it moves through the halo. Therefore, I used the fourth-order Runge-Kutta method (RK4) to solve the equations of motion numerically and calculate the orbital time.

The timescale for dynamical friction, $t_{\rm fric}$ can be, instead, estimated using the formula provided by Binney and Tremaine (2008) for a compact object starting at r_0 in an external potential created by a host galaxy. Let $M_{\rm NFW}(r_0)$ be the mass of the host enclosed mass within r_0, the circular velocity of a point like objects at $r = r_0$ is

$$v_{\rm circ}(r_0) = \sqrt{\frac{GM_{\rm NFW}(r_0)}{r_0}}. \tag{5.3}$$

Then, the crossing time is

$$t_{\rm cross}(r_0) \equiv \frac{r_0}{v_{\rm circ}(r_0)}, \tag{5.4}$$

which measures the characteristic time taken by the satellite to cross Sextans. From Binney and Tremaine (2008), the $t_{\rm fric}$ can be then estimated as

$$t_{\rm fric}(r_0) = \frac{1.17}{\ln\Lambda}\frac{M_{\rm NFW}(r_0)}{M_{\rm sat}} t_{\rm cross}(r_0), \tag{5.5}$$

where $\ln\Lambda$ is the Coulomb logarithm, which depends on the actual geometry of the trajectory. However, as $\ln\Lambda$ typically spans values from 6 to 15, I will consider both cases, denoting them as $t_{\rm fric,15}$ and $t_{\rm fric,6}$, for the lower and upper estimates, respectively.

Consequently, Figure 5.1 shows the comparison between $t_{\rm fric,15}$, $t_{\rm fric,6}$, and $t_{\rm orb}$, for a varying initial position r_0. $t_{\rm fric,15}$ and $t_{\rm fric,6}$ have been calculated using Eq. 5.5, while $t_{\rm orb}$ was calculated numerically. For the initial position, I spanned a range of distances from 0.2 kpc up to the virial radius of Sextans, i.e. 30 kpc, in steps of 0.06 kpc. The initial velocity v_0 was estimated using the momentum conservation law:

$$r_0 v_0 = r_f v_f, \tag{5.6}$$

where r_f is measured from the velocity map in Figure 2.4, and it represents the radius of the ring-like structure, and v_f is the maximum velocity measured in the ring. Additionally, in Figure 5.1 on the black dashed vertical lines spaced every 5 kpc, I reported the values

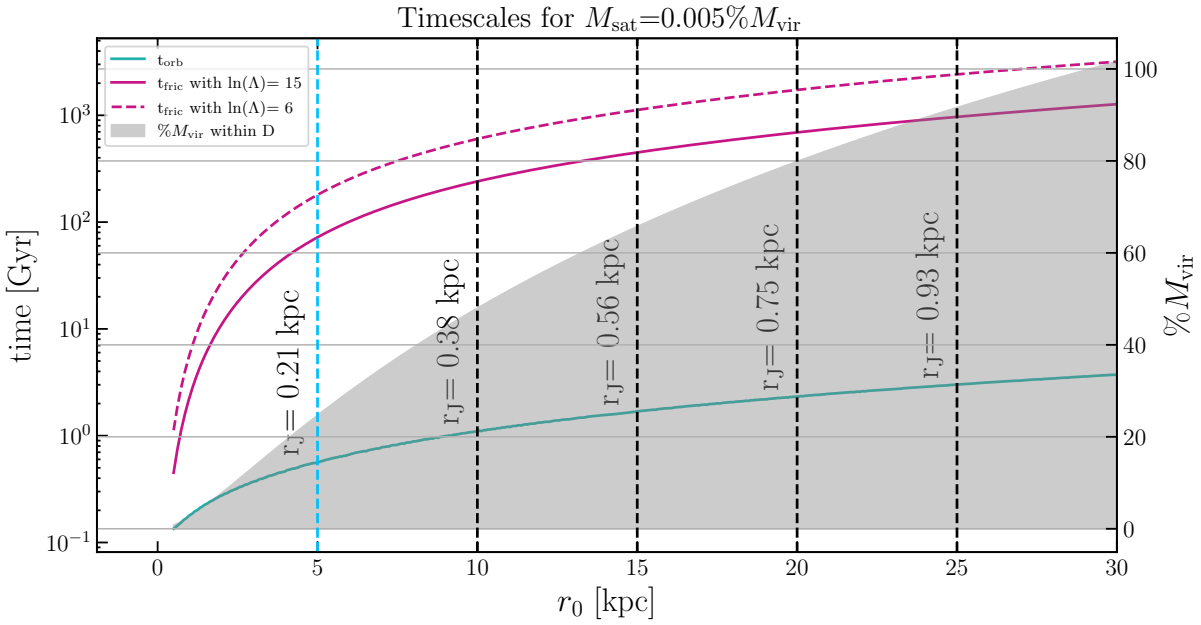

Fig. 5.1 – The characteristic timescales for the simulation as a function of the initial position r_0: the orbital period t_{orb} (teal solid line), and the dynamical friction timescales t_{fric} (pink solid and dashed lines), for the two limiting values of $\ln\Lambda$. On the right axis is reported the percentage of Sextans halo mass within r_0. The vertical dashed lines show values of the Jacobi radius r_J for varying r_0.

of the Jacobi radius (or truncation radius Binney and Tremaine, 2008) of the satellite:

$$r_J(r_0) = r_0 \left(\frac{M_{sat}}{3M_{NFW}(r_0)} \right)^{1/3} . \tag{5.7}$$

The Jacobi radius indicates the distance from the centre of the host galaxy where its tidal forces on the satellite significantly impact the structural properties of the latter, once it is located at a distance r_0 from the host. Finally, the right axis of Figure 5.1 indicates the percentage of the virial mass of the halo M_{vir} within the initial position of the mass particle.

From the image it is evident that for varying r_0, t_{orb} is much smaller than the timescale for dynamical friction, suggesting that the effects of the latter are negligible. The satellite is thus expected to conserve both its initial energy and momentum. In addition, the values of r_J legitimate the adopted model for the satellite, as its scale radius is $\sim 10^{-2}$ kpc (r_s in Tab. 5.1), so, much smaller than both r_0 and r_J, which are $\sim 10^0 - 10^1$ kpc.

A key decision in setting up the simulation is to determine the initial position of the satellite. The goal of this thesis is not to investigate how a satellite is captured by a galaxy, but rather to assess whether the resulting accretion can explain the peculiar velocity structure of Sextans. Thus, in all simulations, the satellite is always initially positioned within the virial radius of Sextans. Given the high values of t_{fric} and the fact that r_J is smaller than the distance between the outskirts of the satellite and the centre of the galaxy, the satellite is not expected (at least in these simulations) to lose a significant amount of mass as it moves closer to Sextans and it will not significantly affect

its structural parameters up until the closer distances.

As an example, only when the satellite reaches $r_0 = 5$ kpc, its Jacobi radius becomes comparable to its half-mass radius. This indicates that interactions occurring at distances greater than 5 kpc allow any gravitational perturbations from the host galaxy to be gradually incorporated into the simulations. Provided that the initial velocity is chosen in accordance with equation Eq. 5.6, simulations with $r_0 > 5$ kpc will thus produce similar outcomes, but on greater timescales. I therefore standardised the satellite's initial position at $r = 5$ kpc.

This also offers an additional advantage: since the Sextans halo is spherically symmetric and the initial position of the satellite always represents the apocentre of the orbit, the satellite's centre of mass will never explore regions beyond 5 kpc. Thus, although the Sextans halo has a virial radius of 29 kpc, it can be truncated well before this value without impacting the dynamics of the interactions. I then chose to truncate the halo at ≈ 7 kpc, a value that ensures the entire size of the satellite remains within the Sextans halo. This choice also provides the significant advantage of reducing the number of particles needed to sample the Sextans halo, and therefore it drastically reduces the computational time for the simulations.

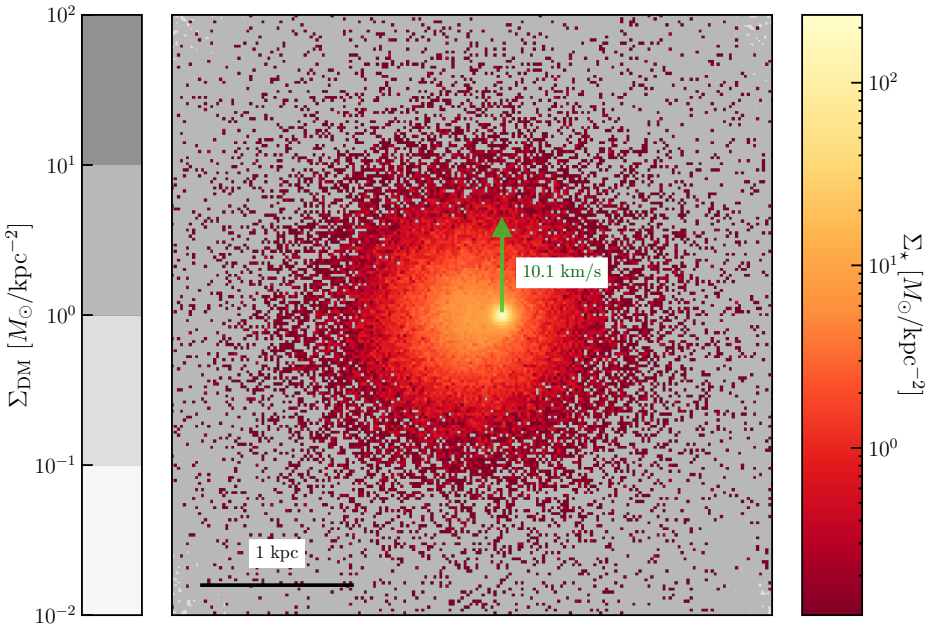

Fig. 5.2 – Case 0. 2D map of the initial set-up of the Sextans+Satellite system, satellite's orbital ICs in Eq. 5.8. In the background, in scales of greys, are the isodensity surfaces of the DM component, overlaid with the surface density distribution of the combined stellar component of Sextans and the satellite (red to yellow colour map). The arrow shows the direction and the value of the initial systemic velocity of the satellite.

5.2 Case 0: A circular orbit at 0.2 kpc

Before investigating the more realistic and physically motivated scenarios, I first tested whether the kinematics of the disrupted satellite could be consistent with it being on

a circular orbit at the same distance from the centre as the ring-like feature shown in Figure 2.4. I placed the satellite at 0.2 kpc on a circular orbit, with the tangential velocity calculated using Eq. 5.3. The orbital ICs in Cartesian coordinates are:

$$\boldsymbol{x}_0 = (0.2, 0, 0)\ [\mathrm{kpc}] \qquad \boldsymbol{v}_0 = (0, 10.1, 0)\ [\mathrm{km/s}]. \tag{5.8}$$

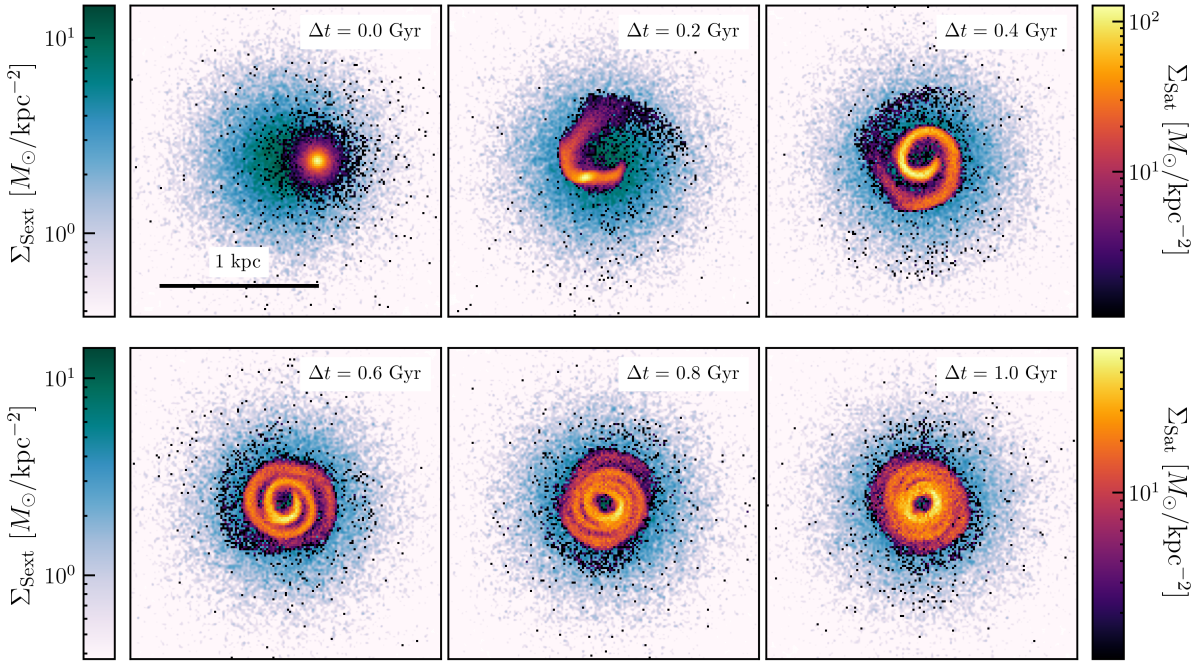

Fig. 5.3 – Case 0. 2D density maps of the Sextans+Satellite system at different times in the simulation, separated by 0.2 Gyr. Sextans and the satellite have different colour gradients to distinguish them visually.

The initial setup is shown in the surfaced density map Figure 5.2. Figure 5.3 shows the evolution up to 1 Gyr. In the figure, it clearly appears that within less than a Gyr, the satellite settles into a ring structure, which remains relatively unchanged afterwards.

To determine whether this simulated structure is compatible with the observed one (shown in the left panel of Figure 2.4), I generated mock data from the simulation to mimic an observation. For some selected snapshots, I aligned the simulated system with the observed one by matching the centre of mass of the Sextans+Satellite system to the centre of Sextans, marked by Cicuéndez and Battaglia (2018). Once the systems were aligned, I selected the simulated star particles closest to the stars observed positions. I then smoothed the l.o.s. velocities of these stars using the same smoothing method employed by Cicuéndez and Battaglia (2018), which involved applying a median kernel over a 5 arcmin (≈ 0.13 kpc) radius. Specifically, for each selected star, the smoothed l.o.s. velocity was computed as the median of the l.o.s. velocities of all neighbouring stars within the 5 arcmin radius. Notably, in simulations, the l.o.s. corresponds to the direction
perpendicular to the plane of the 2D map being analysed, therefore it strictly depends on the chosen point of view. Consequently, the selection and the smoothing procedure had to be repeated for different viewing angles, in order to assure a comprehensive comparison

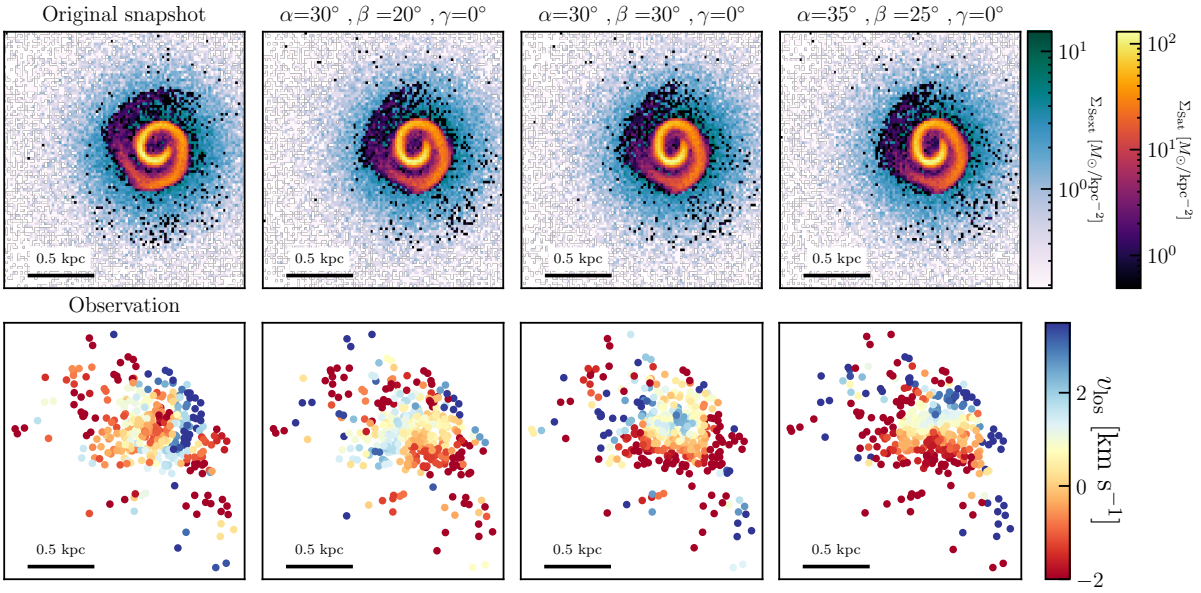

Fig. 5.4 – Case 0. Upper row: 2D density maps of the Sextans+Satellite system at 0.4 Gyr. Sextans and the satellite are shown with different colour gradients to visually distinguish between them. The first image on the left shows the original l.o.s. from Figure 5.3, while the subsequent columns display the system viewed at different rotational angles. Lower row: Smoothed l.o.s. velocity maps. The first image on the left represents the observed dataset, while the remaining images show the mock datasets corresponding to the panels above them, with each map using the same rotational angles as the density maps in the upper row.

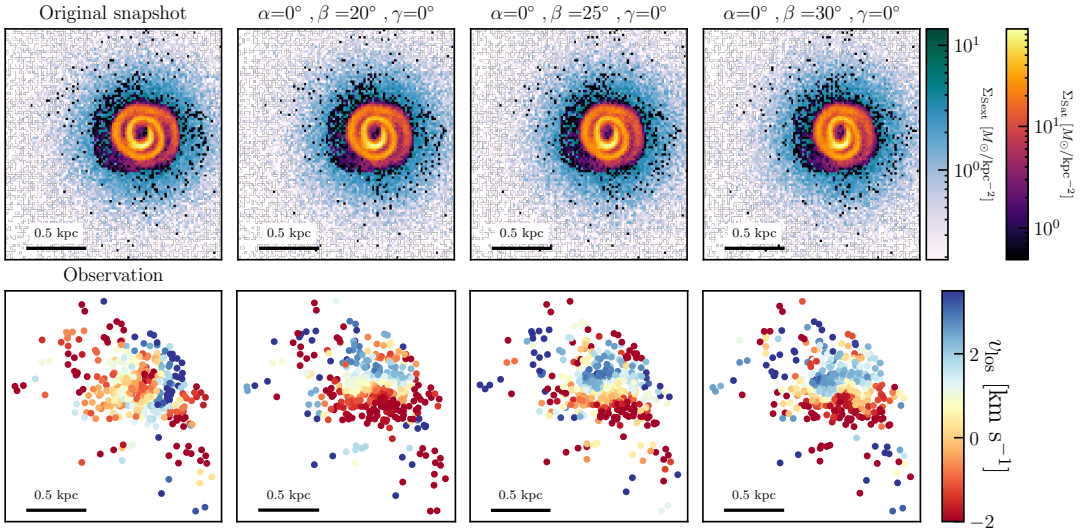

Fig. 5.5 – Case 0. Same as Figure 5.4 but for the Sextans+Satellite system at 0.8 Gyr

between simulations and observations. To obtain this, I applied a series of rotations to the entire system using Euler rotation matrices, defined by three specific angles (α, β, γ), to reorient the system as needed, as described in §§ A.

Next, I iterated the procedure across various snapshots, exploring a wide range of

rotation angles, and visually inspected the resulting velocity maps. Some examples of these maps are shown in Figure 5.4 and Figure 5.5.

Interestingly, in the case shown in the third column of Figure 5.5 a ring-like structure appears also in the velocity map, though with velocities opposite to those observed. It is important to note that the snapshot corresponds to the ring as it is still forming, and not yet in a stable configuration. Therefore, Figure 5.6 shows the same case but with inverted l.o.s. axis.

This suggests that a satellite, having reached the central regions with the profile determined by the parameters in Tab. 5.1, and subsequently disrupted by tidal interactions, can indeed produce a ring-like feature similar to observed one by Cicuéndez and Battaglia (2018). Consequently, in the following cases, I will investigate physically motivated ICs for a satellite without DM, to assess whether such conditions could plausibly explain the presence of the satellite in the central regions or, alternatively, reproduce the ring-like feature through different mechanisms.

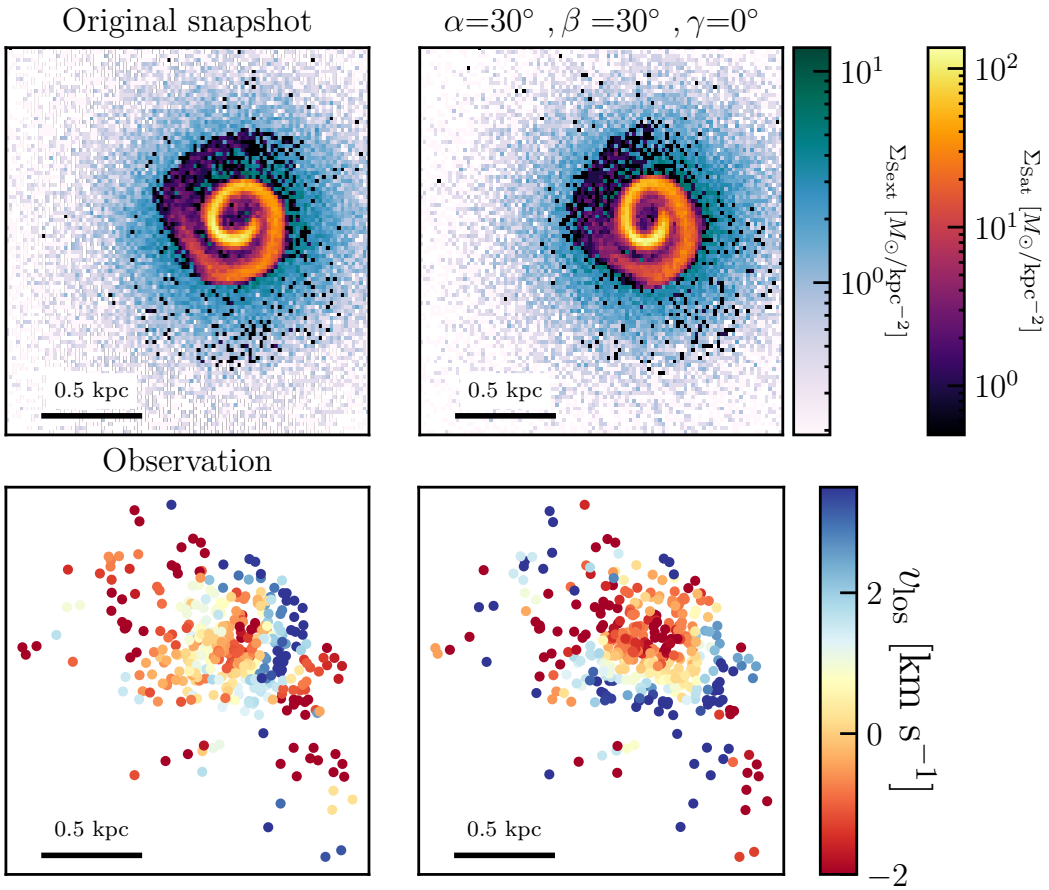

Fig. 5.6 – Case 0. Upper row: 2D density maps of the Sextans+Satellite system at 0.8 Gyr. Sextans and the satellite are shown with different colour gradients to visually distinguish between them. The image on the left shows the original l.o.s. from Figure 5.3, while the one on the right displays the rotated system. Lower row: Smoothed l.o.s. velocity maps. The image on the left reports the observed dataset, while the one on the right shows the mock datasets corresponding to the panel above.

5.3 Case 1: A nearly radial orbit starting at 5 kpc

In this first attempt, I selected the ICs based on the considerations discussed in § 5.1. In particular, I set the satellite at a distance r_0=5 kpc, which results in $v_0 \approx 0.14$ km/s, thus on a nearly radial orbit. The orbital ICs in Cartesian coordinates are:

$$\boldsymbol{x}_0 = (5, 0, 0)\ [\mathrm{kpc}] \qquad \boldsymbol{v}_0 = (0, 0.1, 0)\ [\mathrm{km/s}]. \tag{5.9}$$

The ICs are displayed in the surface density map in Figure 5.7. I then let the Sex-

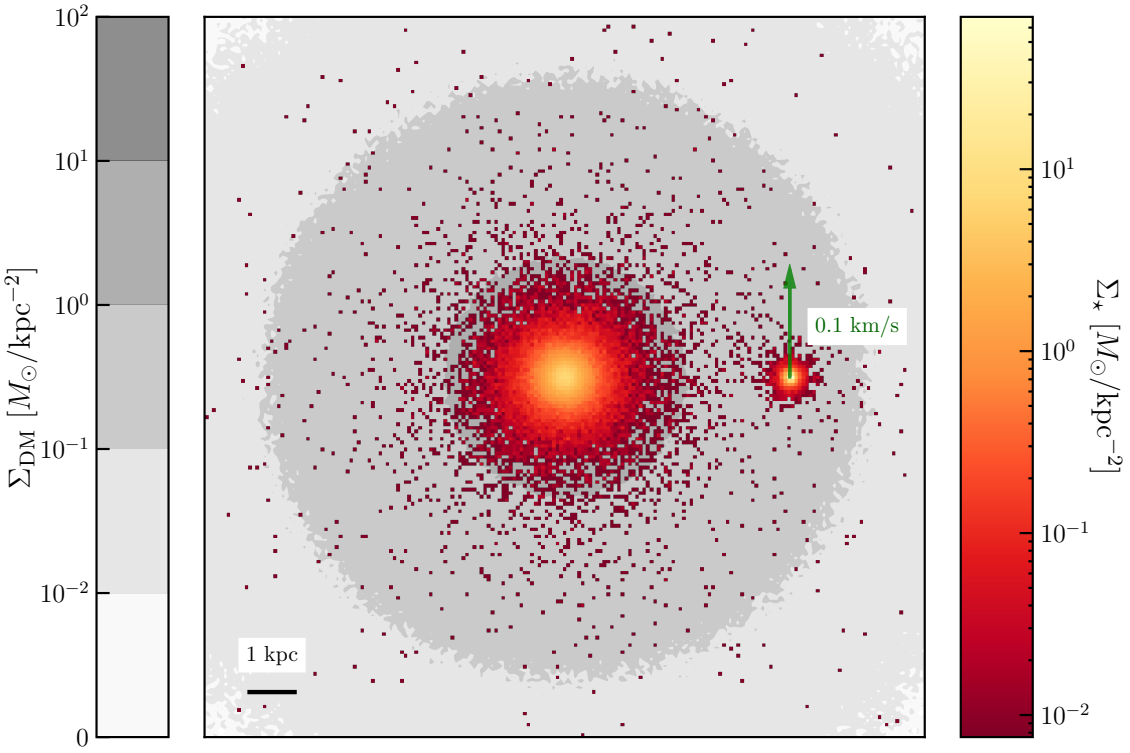

Fig. 5.7 – Case 1. Same as Figure 5.2 but for the orbital ICs in Eq. 5.9.

tans+Satellite system evolve for 12 Gyr. In Figure 5.8 I only report the 2D density maps up to 5.5 Gyr, as there were no significant differences in the subsequent timesteps. In addition to this, Figure 5.9 shows a zoomed-in view of the inner regions from the snapshot at 5.5 Gyr and for three perpendicular l.o.s. In this case, the only remarkable features obtained in the simulation are shell-like structures consistent with the ones found by Hernquist and Quinn (1988) using a similar set up. These shells are typically formed when a satellite galaxy is disrupted by the gravitational field of a larger host galaxy. As the satellite is torn apart, its stars or DM particles are stripped and spread out, gradually organising into concentric, spherical-like shells as they orbit within the host's potential. The Case 1 simulations satisfy many of the conditions that Hernquist and Quinn (1988) identified as promoting the formation of shells, particularly:

- radial or nearly radial orbits: on radial orbits particles stripped from the satellite experience strong tidal forces, causing them to oscillate back and forth through the host galaxy's potential, leading to the formation of distinct, concentric shells at

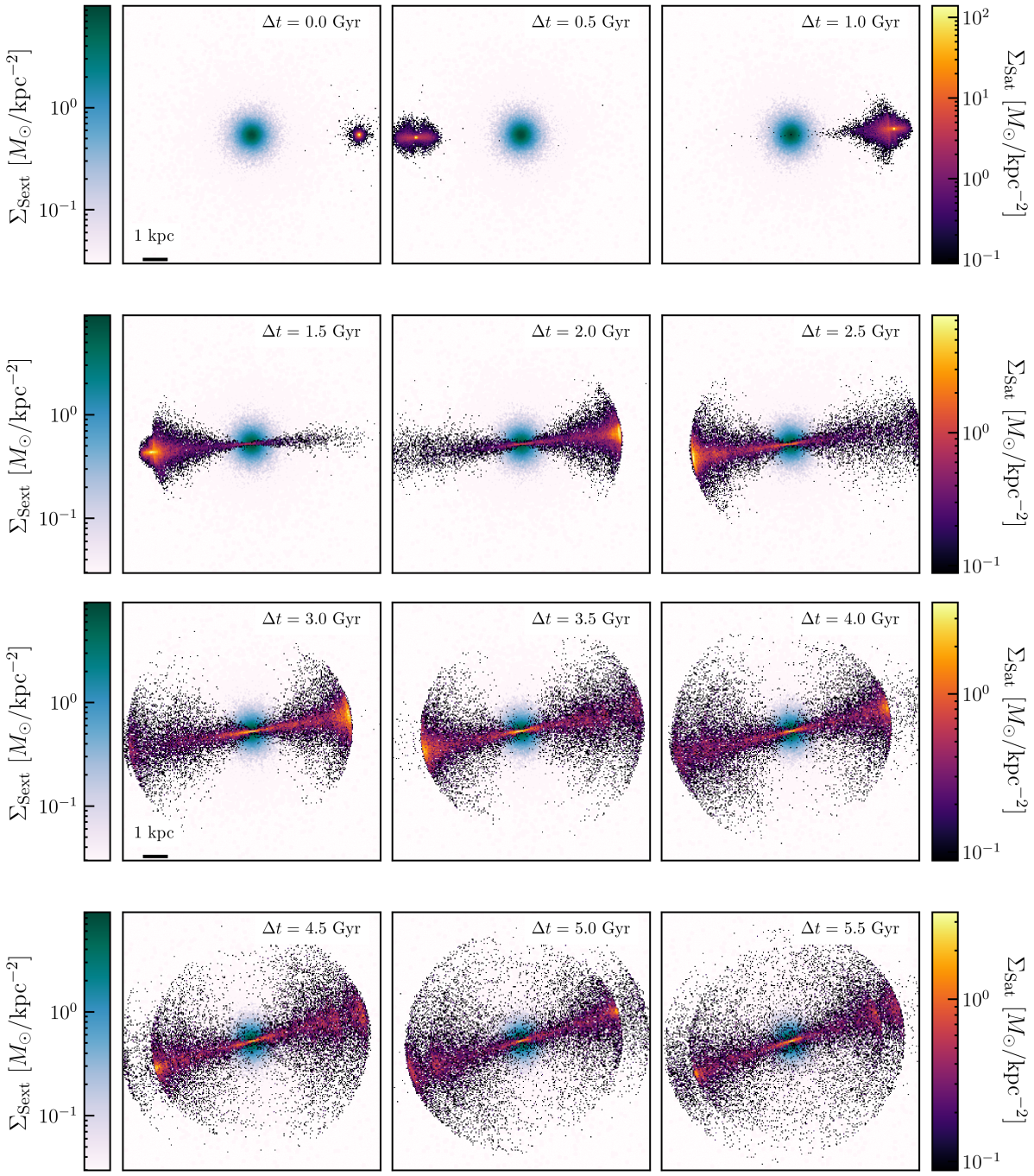

Fig. 5.8 – Case 1. 2D density maps of the Sextans+Satellite system in the simulation separated by 0.5 Gyr, up to 5.5 Gyr. Sextans and the satellite have different colour gradients to distinguish them visually.

different radii;

- low merger mass ratio: a lower-mass satellite is less capable of retaining its structure due to the strong gravitational forces from the host, which strip its particles and disperse them into shells;
- spherical or a near-spherical host potential: a relatively smooth, spherical gravitational potential in the host galaxy allows the stripped particles to remain confined in spherical distributions.

It is evident from both Figure 5.8 and Figure 5.9, that these ICs do not preserve the structure of the satellite, and thus do not lead to the scenario in Case 0, nor do they reproduce any ring-like structure in any snapshot of the simulation. Consequently, I discarded this set-up as a possible scenario for the accretion event that occurred in the galaxy.

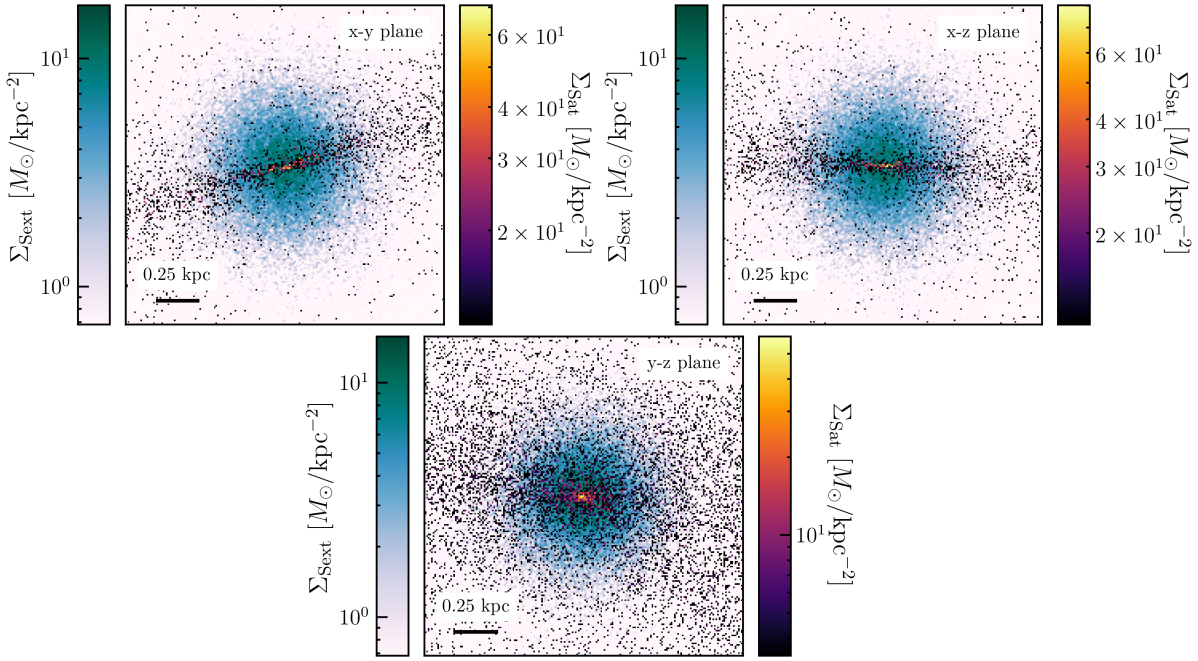

Fig. 5.9 – Case 1. Zoom-in 2D density maps of the Sextans+Satellite system in the simulation at 5.5 Gyr. The three panels show the three perpendicular points of view. Sextans and the satellite have different colour gradients to distinguish them visually.

5.4 Case 2: An eccentric orbit starting at 5 kpc

After the failure of Case 1, I investigated a similar set-up, but with a larger initial velocity. The orbital ICs in Cartesian coordinates are:

$$\boldsymbol{x}_0 = (5, 0, 0)\ [\text{kpc}] \qquad \boldsymbol{v}_0 = (0, 3, 0)\ [\text{km/s}], \tag{5.10}$$

as shown in Figure 5.10. Figure 5.11 shows how the system evolved up to 8.5 Gyr.

In the later stages, the disrupted satellite appears to form shell-like structures, similarly to the ones observed in Case 1. However, due to its higher initial tangential velocity, the satellite forms arc-like structures already from the early stages of the simulation and avoids passing through the galaxy's centre.

It is therefore plausible that a ring-like structure could emerge when observing these arcs from a suitable viewpoint. To explore this possibility, I selected the timestep at 8 Gyr and analysed it from different lines of sight. The results are shown in Figure 5.12, where, to simplify the interpretation, only the stellar population of the satellite is displayed. In this case, for varying angles α and β, I explored six different inclinations of the structure.

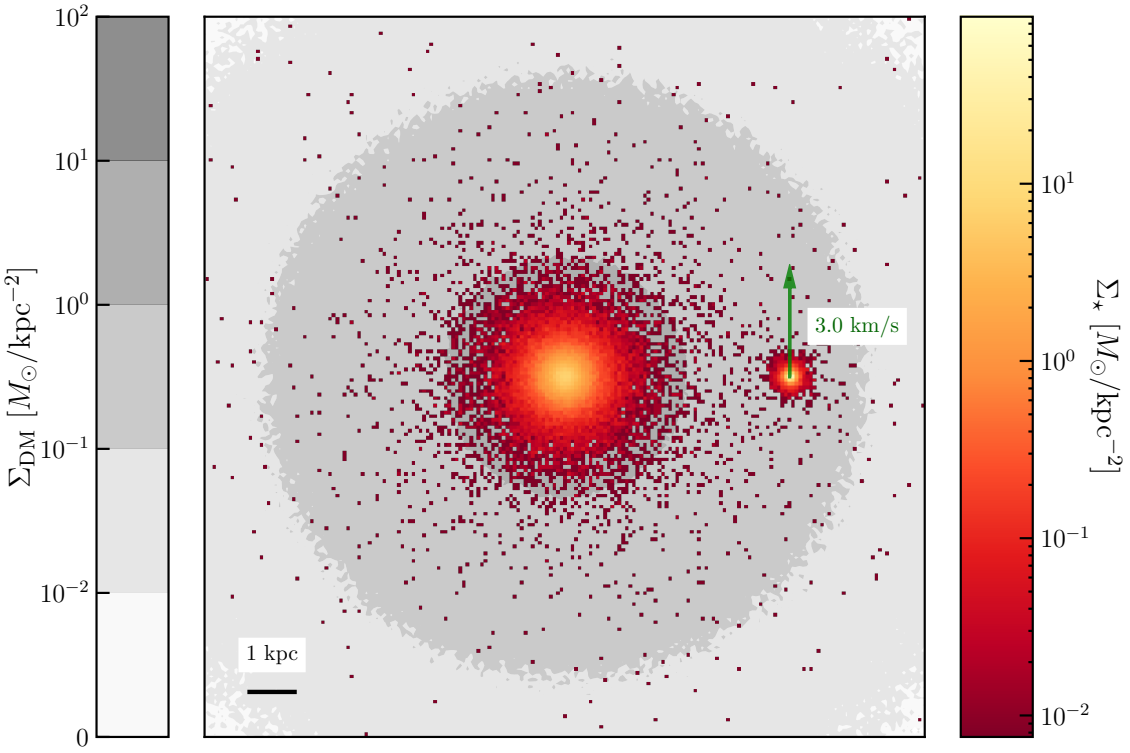

Fig. 5.10 – Case 2. Same as Figure 5.2 but for the orbital ICs in Eq. 5.10.

For each set of angles, the upper panel displays the surface density $\Sigma_{\rm Sat}$ map, while the lower panel shows the l.o.s. velocity $v_{\rm los}$ map. Although a ring-like structure can be seen in the surface density map for the case $\beta = 75°$, this feature nearly vanishes in the velocity map. Instead, the velocity map shows a pattern where one region is moving towards the observer and another is receding, resembling the behaviour of a system rotating around the centre of the galaxy. Moreover, the l.o.s. velocities resulting from this projection are not compatible with the observed values, being at least an order of magnitude higher than those shown in Figure 2.4.

Although it can reproduce a ring-like structure at the centre, the velocity pattern is not consistent with observations or expected dynamics.

In conclusion, I have found that it is not possible to reproduce the observed ring-like structure or the configuration of Case 0 without the satellite having a DM halo. In particular, the simulations in this chapter have shown that, without DM in the satellite, it is not possible

1. to bring the satellite intact into the central regions;
2. to maintain sufficiently low velocities compatible with the observed ones.

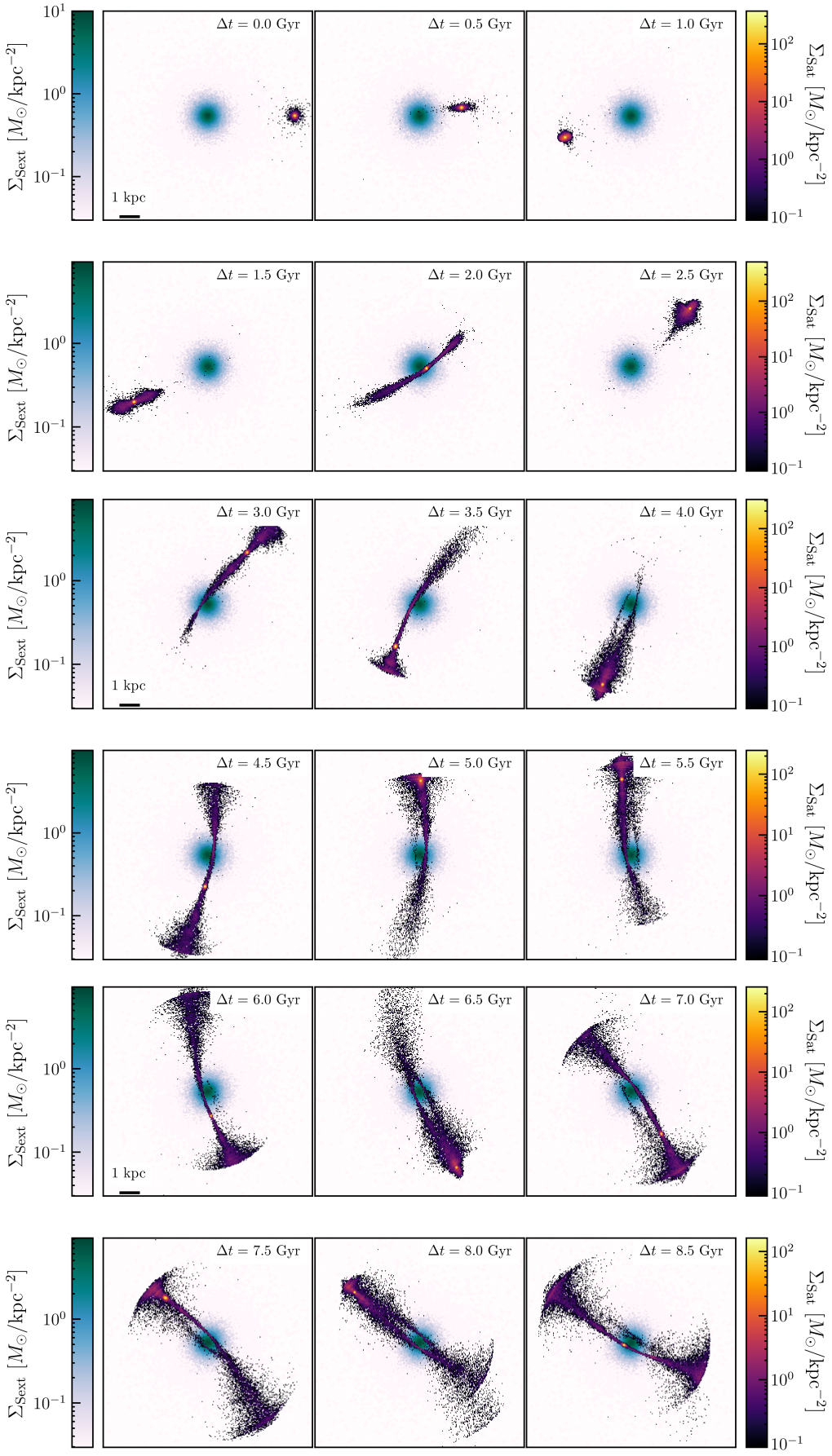

Fig. 5.11 – Case 2. 2D density maps of the Sextans+Satellite system at different times in the simulation, separated by 0.5 Gyr. Sextans and the satellite have different colour gradients to distinguish them visually.

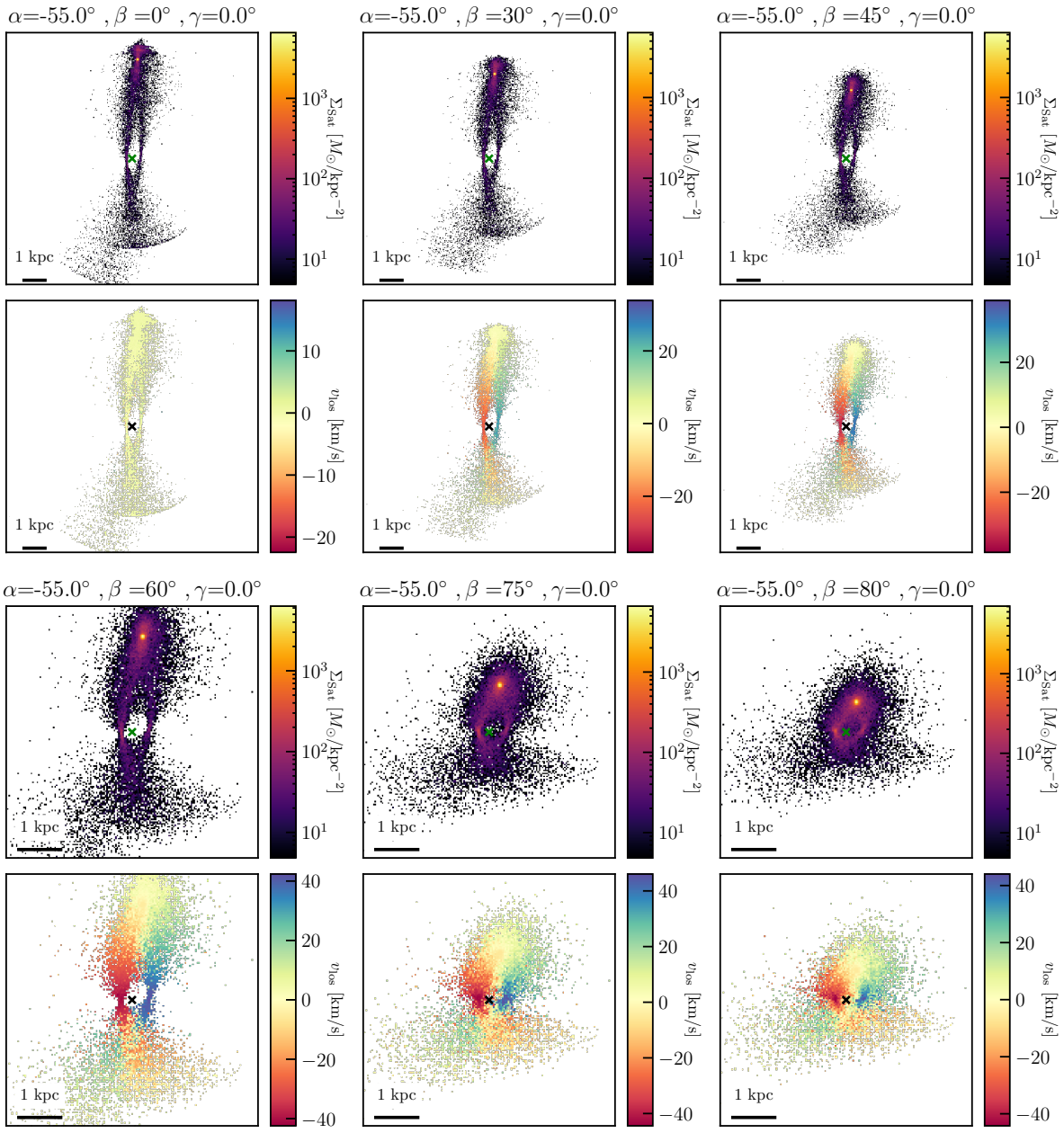

Fig. 5.12 – Case 2. Surface density $\Sigma_{\rm Sat}$ maps (upper panels) and l.o.s. velocity $v_{\rm los}$ maps (lower pales) for six different inclination angles. The green and black crosses in the maps mark the centre of Sextans.

VI

Simulations with a Satellite Embedded in a Dark Matter Halo

In this chapter, I will present the results of the simulations and investigate whether the observed velocity map of Sextans can be reproduced through a minor merger event involving a satellite composed of both stars and dark matter. The primary objective is to explore different configurations of dark matter halos for the satellite using a trial-and-error approach. By doing so, I aim to assess how various halo properties influence the stability of Sextans and determine if they can replicate the distinctive ring-like velocity structure observed in the galaxy.
In § 6.2 and § 6.3, I will discuss two initial attempts in which the satellite's dark matter halo was found to be too compact and massive, preventing it from being effectively disrupted into the ring-like feature seen in Sextans. Both configurations failed to reproduce the desired kinematic features and, moreover, disrupted the stable equilibrium of the galaxy.
Finally, in § 6.4 I will present a successful simulation that reproduces the peculiar velocity pattern observed in the galaxy and demonstrates a more suitable satellite halo configuration for the accretion event.

6.1 General considerations

As a consequence of the findings from the previous chapter, which demonstrated that simulations involving a satellite composed solely of stars fail to recreate the observed ring-like structure in the inner region of Sextans. In this chapter, I will investigate accretion events involving a two-component satellite composed of both stars and DM.

For the stellar component, I adopted a Plummer profile with the same structural parameter as in Tab. 5.1, i.e. a total mass of ≈30% the inferred Sextans stellar mass and a scale radius of 0.04 kpc. Since the stellar particles of the satellite must be identical to the stellar ones in the Sextans-like system, also m_p remained at 4.8 $M_\odot$, and consequently neither the number of stellar particles changed. For the DM component, observational data offers no direct constraints, necessitating an arbitrary construction of the halo. To ensure a physically motivated choice, I initially consulted McConnachie (2012) to search for objects in the Local Universe with similar stellar mass and scale radius to the satellite, hoping to infer the DM halo from known analogues. Unfortunately, no such objects were found with both compatible structural properties and available dynamical mass estimates. I then relayed on known scaling relations, as the one reported in Figure 1.3, to roughly estimate the halo mass. Indeed, assuming a stellar mass-to-light ratio of 1, for an object with a stellar mass of $\sim 10^5\,M_\odot$ one could expect the dynamical mass to luminous mass ratio in the range $10^2 - 10^4$.

In testing these halo profiles, I aimed to balance two factors: ensuring the galaxy stability during the evolution, and reproducing the observed stellar structures at the centre Sextans. This process, while empirical, allowed me to explore a range of plausible halo characteristics and to identify configurations that best matched the target observational features.

For these simulations, since the mass varies from case to case, the timescales $t_{\rm orb}$ and $t_{\rm fric}$, that were introduced in § 5.1, will be determined individually for each specific scenario and discussed in the subsequent sections.

	Stars	DM
Model	Plummer	Truncated NFW
$M\,[M_\odot]$	1.2×10^5	2.8×10^8
R_s [kpc]	0.04	–
r_s [kpc]	–	0.7
r_t [kpc]	–	2
Npts	25000	2767404
$m_p\,[M_\odot]$	4.8	96
q	0.28	

Tab. 6.1 – Case 3. Structural parameters for each Satellite component. Stars follow a Plummer profile (Eq. 3.33), while the DM follows a truncated NFW profile (Eq. 4.3). From the top, the table lists the total mass M of the component, the Plummer scale radius R_s for the stars, and the scale radius r_s and truncation radius r_t for the DM halo, Npts the number of particles, and m_p the mass of each particle.

6.2 Case 3: A satellite with $M_{\rm Sat} = 10\% M_{\rm vir}$

In this first attempt, I modelled the satellite's DM halo as a scaled-down version of Sextans, with the structural parameters of each component of the satellite reported in Tab. 6.1. It is important to notice that for both the stellar and DM components, the number of particles, Npts, was determined by ensuring that the mass of each particle matches the mass of the corresponding particle in the Sextans-like system. Moreover, in the merger mass ratio q, defined in Eq. 5.1, $M_{\rm Sat}$ refers to the total mass of the satellite in the simulation, formally the sum of both stellar and DM total mass M in Tab. 6.1.

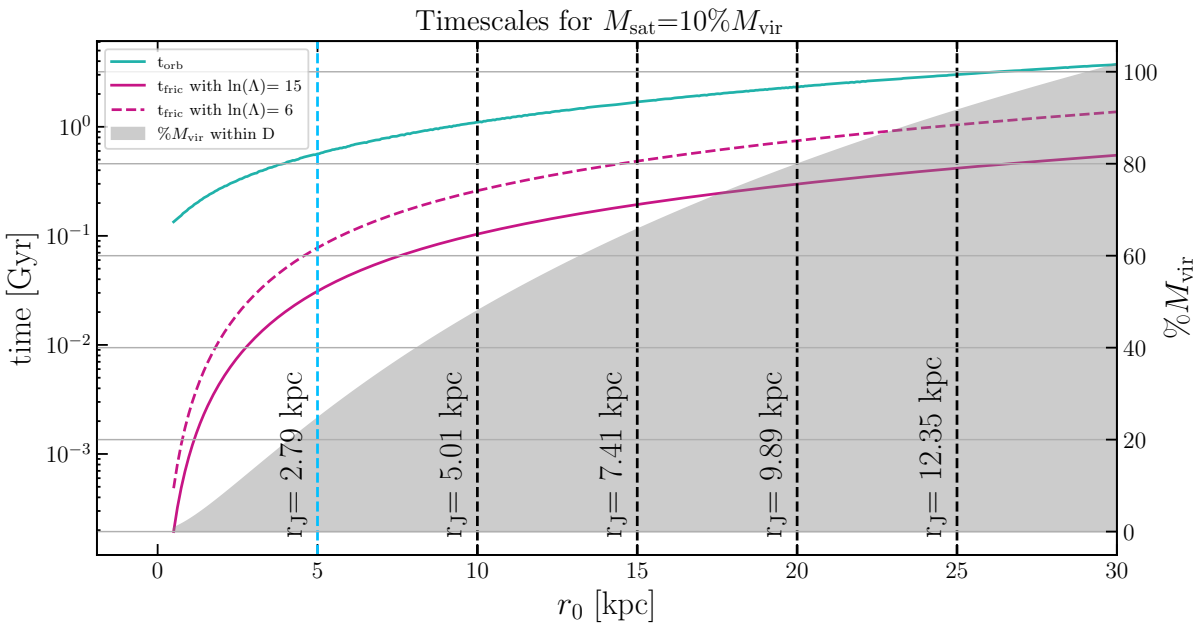

Fig. 6.1 – Case 3. The characteristic timescales for the simulation as a function of the initial position r_0: the orbital period $t_{\rm orb}$ (teal solid line), and the dynamical friction timescales $t_{\rm fric}$ (pink solid and dashed lines), for the two limiting values of $\ln\Lambda$. On the right axis is reported the percentage of Sextans halo mass within r_0. The vertical dashed lines show values of the Jacobi radius $r_{\rm J}$ for varying r_0.

Figure 6.1 was obtained analogously to Figure 5.1, but for $M_{\rm sat} = 2.8 \times 10^8\, M_\odot$, which corresponds to approximately the 10% of Sextans virial mass, and q=0.28 in the simulation. At greater initial distances r_0, $t_{\rm fric}$ is comparable to $t_{\rm orb}$, but it decreases rapidly for decreasing distances. This implies that, in this scenario, the effects of dynamical friction are no longer negligible and will significantly influence the dynamics of the interaction, especially as the satellite approaches the central regions. However, similar to the case of a DM-free satellite, the Jacobi radius $r_{\rm J}$ becomes comparable to the satellite's half-mass radius only for $r_0 < 5$ kpc. This suggests that interactions occurring at distances greater than 5 kpc allow the gravitational perturbations from the host galaxy to be gradually integrated into the satellite's evolution. Consequently, for a given initial velocity, simulations with $r_0 > 5$ kpc will yield similar outcomes, although over longer timescales. This again justifies the decision to place the satellite's initial position at $r = 5$ kpc and to truncate the Sextans halo at 7 kpc.

Due to dynamical friction, the satellite's energy and angular momentum are not con-

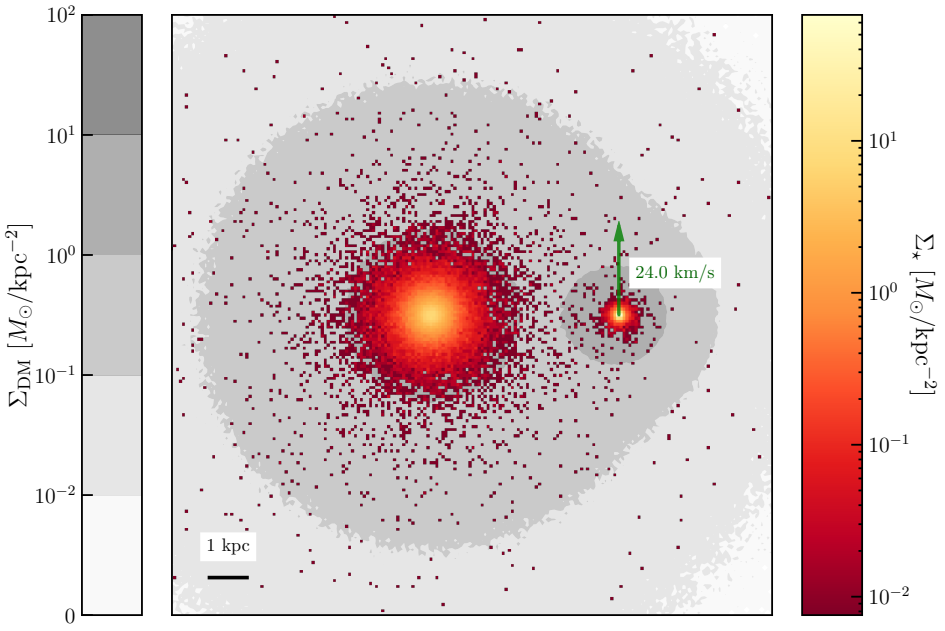

Fig. 6.2 – Case 3. 2D map of the initial set-up of the Sextans+Satellite system, satellite's orbital ICs in Eq. 6.1. In the background, in scales of greys, are the isodensity surfaces of the DM component, overlaid with the surface density distribution of the combined stellar component of both Sextans and the satellite (red to yellow colour map). The arrow shows the direction and the value of the initial systemic velocity of the satellite.

served throughout the simulation. As a result, the initial position r_0 and velocity v_0 are not expected to satisfy Eq. 5.6. Therefore, I opted to place the satellite on a circular orbit, assigning it a tangential velocity calculated using Eq. 5.3. The loss of angular momentum of the satellite will bring it on a short timescale on a radial orbit and it will eventually move close to the center of Sextans. The orbital ICs in Cartesian coordinates are:

$$\boldsymbol{x}_0 = (5, 0, 0)\ [\mathrm{kpc}] \qquad \boldsymbol{v}_0 = (0, 24.1, 0)\ [\mathrm{km/s}], \tag{6.1}$$

and the initial setup is shown in Figure 6.2. Figure 6.6 shows how the system evolved up to 2.2 Gyr, as the configuration remained substantially unchanged afterwards. The outcome of the simulation demonstrates that a satellite of this type severely affects the structural and dynamical properties of Sextans. Due to its high compactness, once the satellite reaches the central regions of the galaxy, these regions experience strong tidal forces. Initially, these forces disrupt the spherical symmetry of the system, which later reconfigures again into a spherical shape around the satellite. The latter, in the end, effectively acts as a dense, compact core. More importantly, the satellite remains almost intact throughout the simulation and, thus, does not reproduce any of the ring-like features.

For all these reasons, I concluded that the satellite halo, with the parameters outlined in Tab. 6.1, proved to be too massive and too compact. Consequently, in the next section, I will reduce the mass of the satellite while maintaining the same scale and truncation radius.

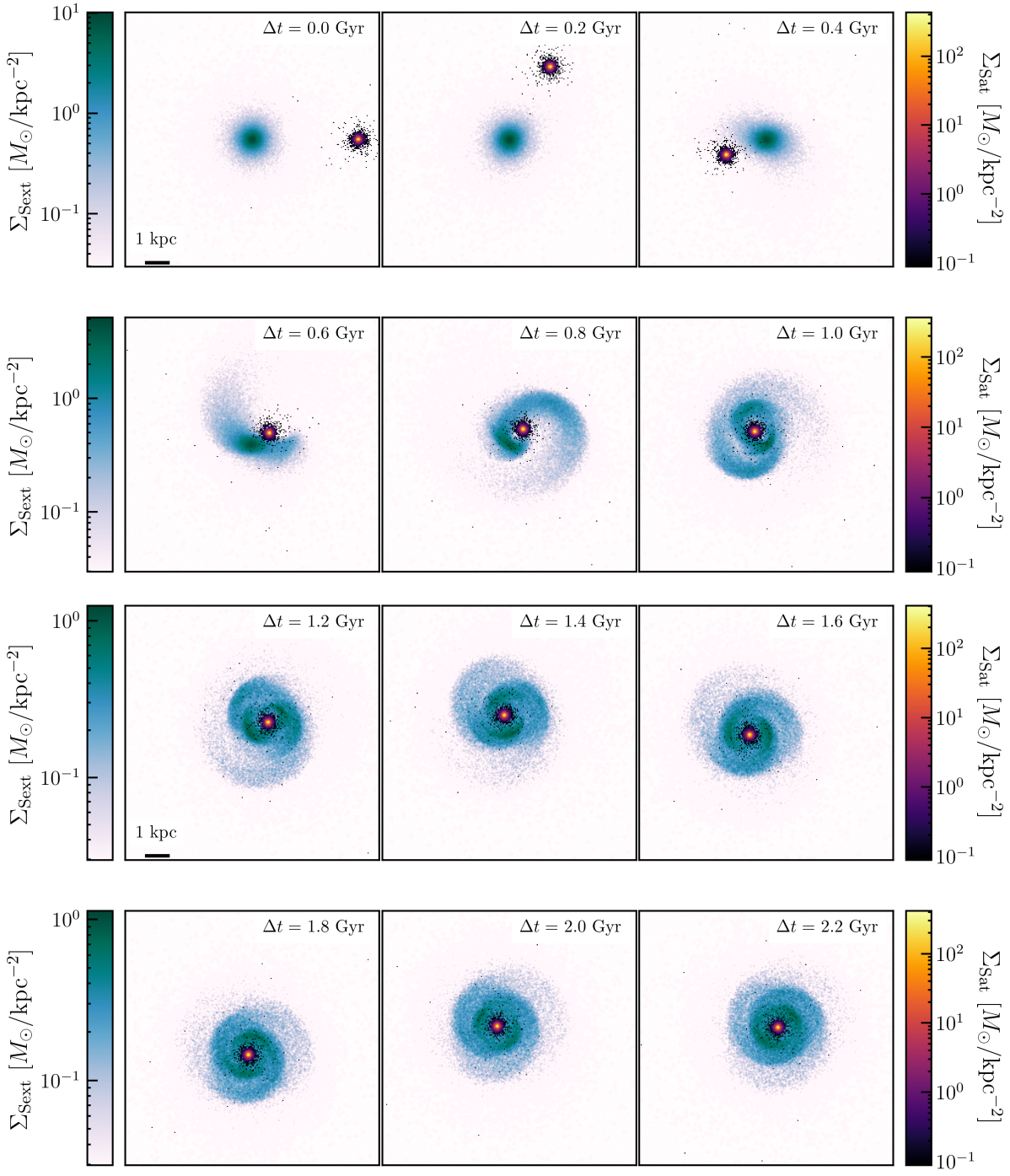

Fig. 6.3 – Case 3. 2D density maps of the Sextans+Satellite system at different times in the simulation, separated by 0.2 Gyr. Sextans and the satellite have different colour gradients to distinguish them visually.

6.3 Case 4: A satellite with $M_{\rm Sat} = 5\% M_{\rm vir}$

Since the halo in Case 3 was found to be too compact and massive to be disrupted while falling into Sextans' potential, in this section I will investigate the case of a satellite with a less dense and less massive halo. To achieve this, I reduced the mass of the halo to half that of Case 3, while maintaining the same scale and truncation radii. All parameters are reported in Tab. 6.2.

	Stars	DM
Model	Plummer	Truncated NFW
$M\ [M_\odot]$	1.2×10^5	1.3×10^8
R_s [kpc]	0.04	–
r_s [kpc]	–	0.7
r_t [kpc]	–	2
Npts	25000	1383702
$m_p\ [M_\odot]$	4.8	96
q	0.13	

Tab. 6.2 – Case 4. Structural parameters for each Satellite component. Stars follow a Plummer profile (Eq. 3.33), while the DM follows a truncated NFW profile (Eq. 4.3). From the top, the table lists the total mass M of the component, the Plummer scale radius R_s for the stars, and the scale radius r_s and truncation radius r_t for the DM halo, Npts the number of particles, and m_p the mass of each particle.

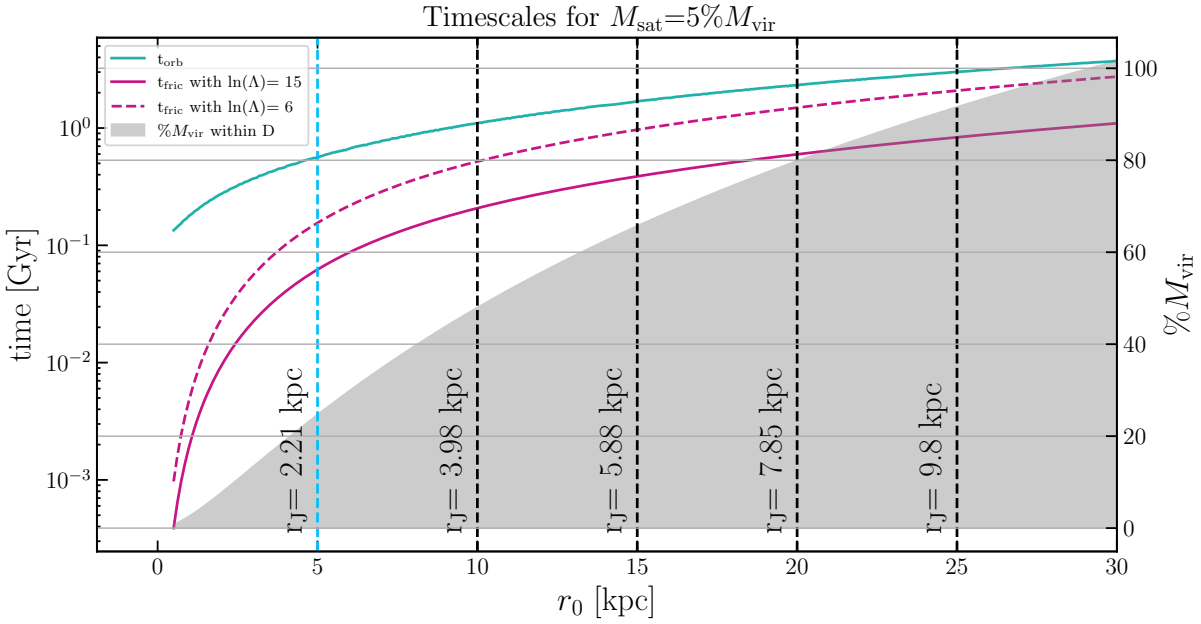

Fig. 6.4 – Case 4. Same as Figure 6.1 but for $M_{\rm Sat} = 5\% M_{\rm vir}$

By proceeding analogously to the previous case, I obtained Figure 6.7, which shows the typical timescales for the simulation in case of $M_{\rm sat} = 1.3 \times 10^8\, M_\odot$. For this mass q=0.13 in the simulation. In this case $M_{\rm Sat}$ corresponds to the ∼5% of Sextans virial mass.

The image shows similar trends to those in Figure 6.4, indicating that all considerations regarding the ICs for the simulation discussed in the previous case remain applicable. Specifically, to the satellite I assigned the same orbital ICs from Eq. 6.1 of Case 3, as illustrated in Figure 6.8. The evolution of the merger is displayed in Figure 6.6 up to 2.2 Gyr. The simulation shows that, despite the reduction of the satellite halo mass, the outcome is fairly similar to the previous case, with the only difference that the tidal forces that disrupt the Sextans in the early phases appear less intense.

As a result, this scenario was discarded. In the next section, I will further reduce the halo mass while maintaining the same scale and truncation radius, to explore whether an even less dense satellite, exerting minimal or no tidal forces on the host galaxy, could finally reproduce the target feature in Sextans.

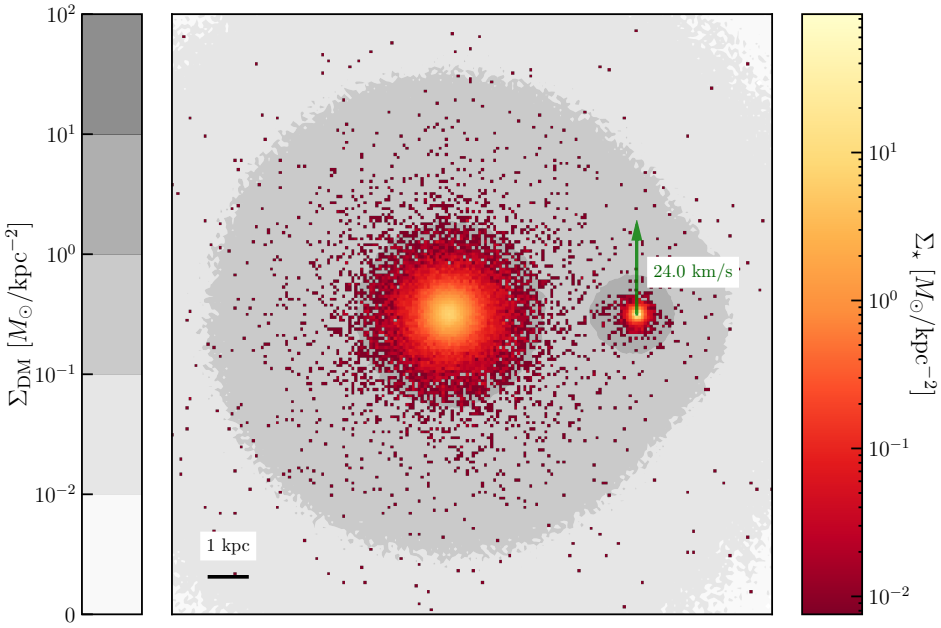

Fig. 6.5 – Case 4. Same as Figure 6.2, with the satellite in the same orbital ICs but a different DM halo (Tab. 6.2).

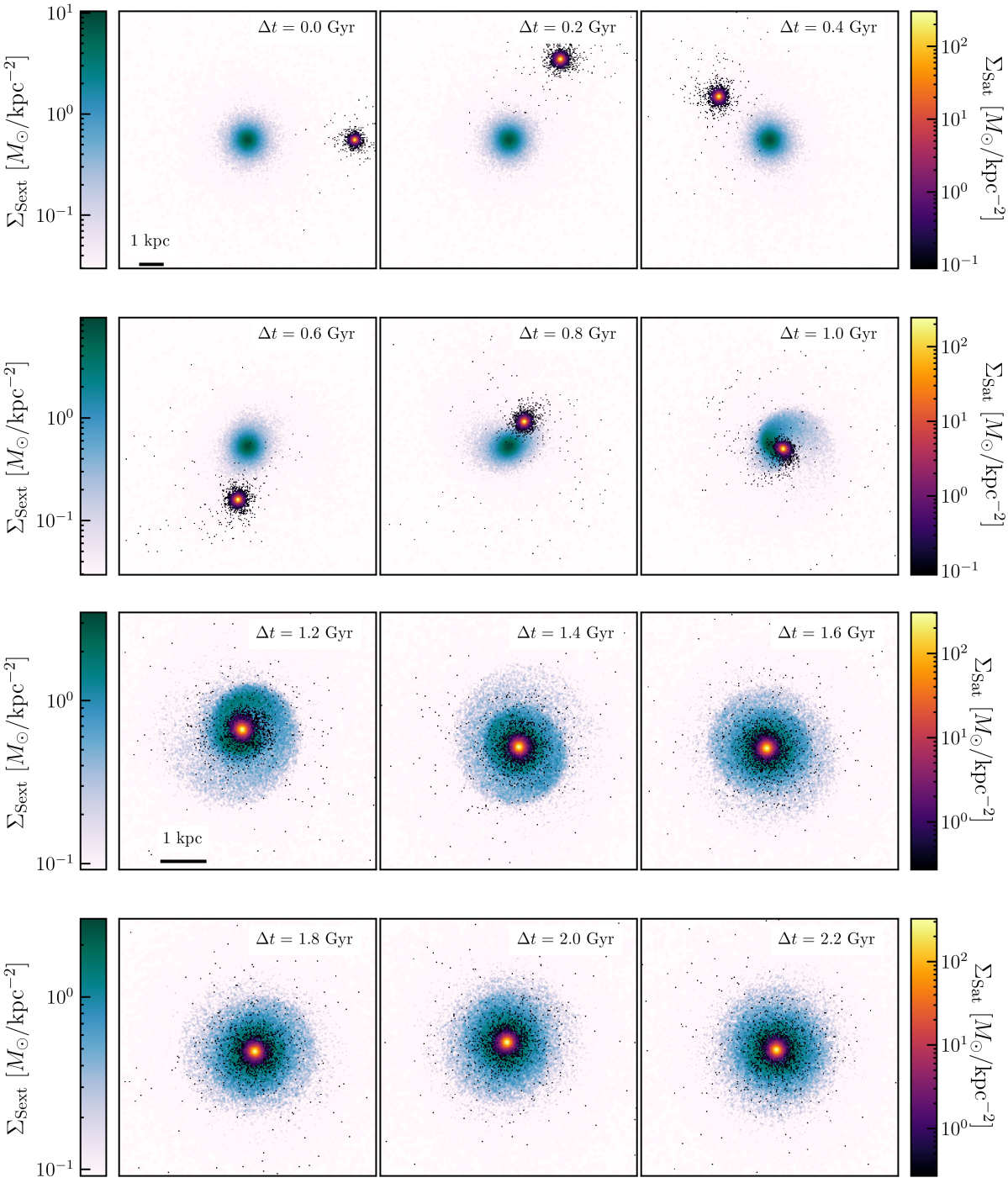

Fig. 6.6 – Case 4. 2D density maps of the Sextans+Satellite system at different times in the simulation, separated by 0.2 Gyr. Sextans and the satellite have different colour gradients to distinguish them visually.

6.4 Case 5: A satellite with $M_{\rm Sat} = 2\%M_{\rm vir}$

Proceeding with the trial-and-error approach, and given that the previous simulations suggested the need for an even less dense satellite halo, I further reduced the halo mass while maintaining the same scale and truncation radius. This adjustment was made to produce an even less compact object and evaluate whether this configuration could yield a more realistic interaction with Sextans. All parameters are reported in Tab. 6.3.

	Stars	DM
Model	Plummer	Truncated NFW
M $[M_\odot]$	1.2×10^5	7.4×10^7
R_s [kpc]	0.04	–
r_s [kpc]	–	0.7
r_t [kpc]	–	2
Npts	25000	760246
m_p $[M_\odot]$	4.8	96
q	0.08	

Tab. 6.3 – Case 5. Structural parameters for each Satellite component. Stars follow a Plummer profile (Eq. 3.33), while the DM follows a truncated NFW profile (Eq. 4.3). From the top, the table lists the total mass M of the component, the Plummer scale radius R_s for the stars, and the scale radius r_s and truncation radius r_t for the DM halo, Npts the number of particles, and m_p the mass of each particle.

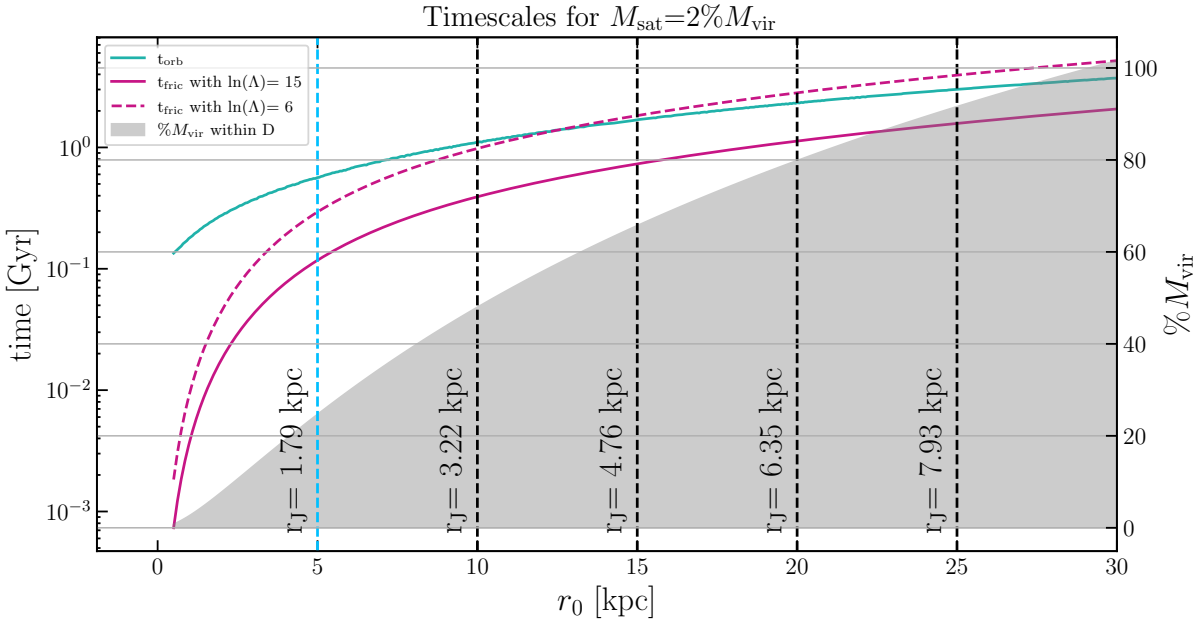

Fig. 6.7 – Case 5. Same as Figure 6.1 but for $M_{\rm Sat} = 2\%M_{\rm vir}$

As in the previous cases, I checked the timescales for the simulation, which in this case are calculated for $M_{\rm sat} \approx 2\%$ of Sextans virial mass. In this case $q = 0.08$. As indicated

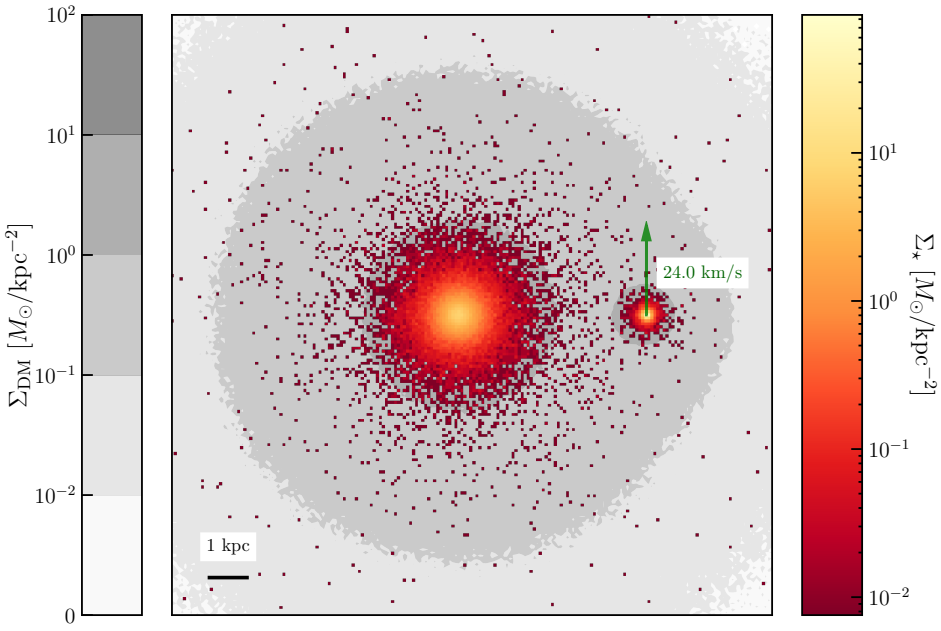

Fig. 6.8 – Case 5. Same as Figure 6.2, with the satellite in the same orbital ICs but a different DM halo (Tab. 6.3).

in Figure 6.7, these timescales are again similar to both the ones of Case 3 and Case 4, meaning that all considerations regarding the ICs for the simulation are still valid.

Therefore, I set the orbital ICs for the satellite in Eq. 6.1, as in the previous cases. As shown in Figure 6.9, the satellite does not disrupt Sextans' spherical symmetry. Within approximately 1.5 Gyr, tidal interactions with the galaxy gradually strip material from the satellite, leading to the formation of a spiralling structure, that over time, evolves into a ring.

Next, I compared the results of the simulation with the velocity map of Figure 2.4 by creating mock observations using the same method described in § 6.2. As in that case, I visually inspected a variety of points of view for different snapshots to find the one that best reproduces the observation. Some of these results are shown in Figure 6.10, while the best one is displayed separately in Figure 6.11. In that case, indeed, the mock velocity map shows a ring structure with a coherent positive velocity, as found by Cicuéndez and Battaglia (2018). Interestingly, the snapshot that best matches the observed velocity map corresponds to a phase where the ring structure is not yet completely formed but is still evolving, consistently with the results of Case 0.

The results of this simulation provide strong evidence that the ring-like feature observed by Cicuéndez and Battaglia (2018) in the velocity map of Sextans' inner regions can be explained by an ongoing accretion event involving a satellite galaxy. The dynamics of this interaction suggest that the satellite's infall is responsible for creating the distinctive structure seen in the velocity field.

Ultimately, I verified that the satellite halo modelled with the parameter in Tab. 6.3 could be compatible with a halo that one would expect from cosmological considerations. The virial mass $M_{\rm vir}$ of the halo could be estimated by extrapolating to the lower limit the stellar-to-halo mass relation found by Read et al. (2017) for DGs. Adopting the

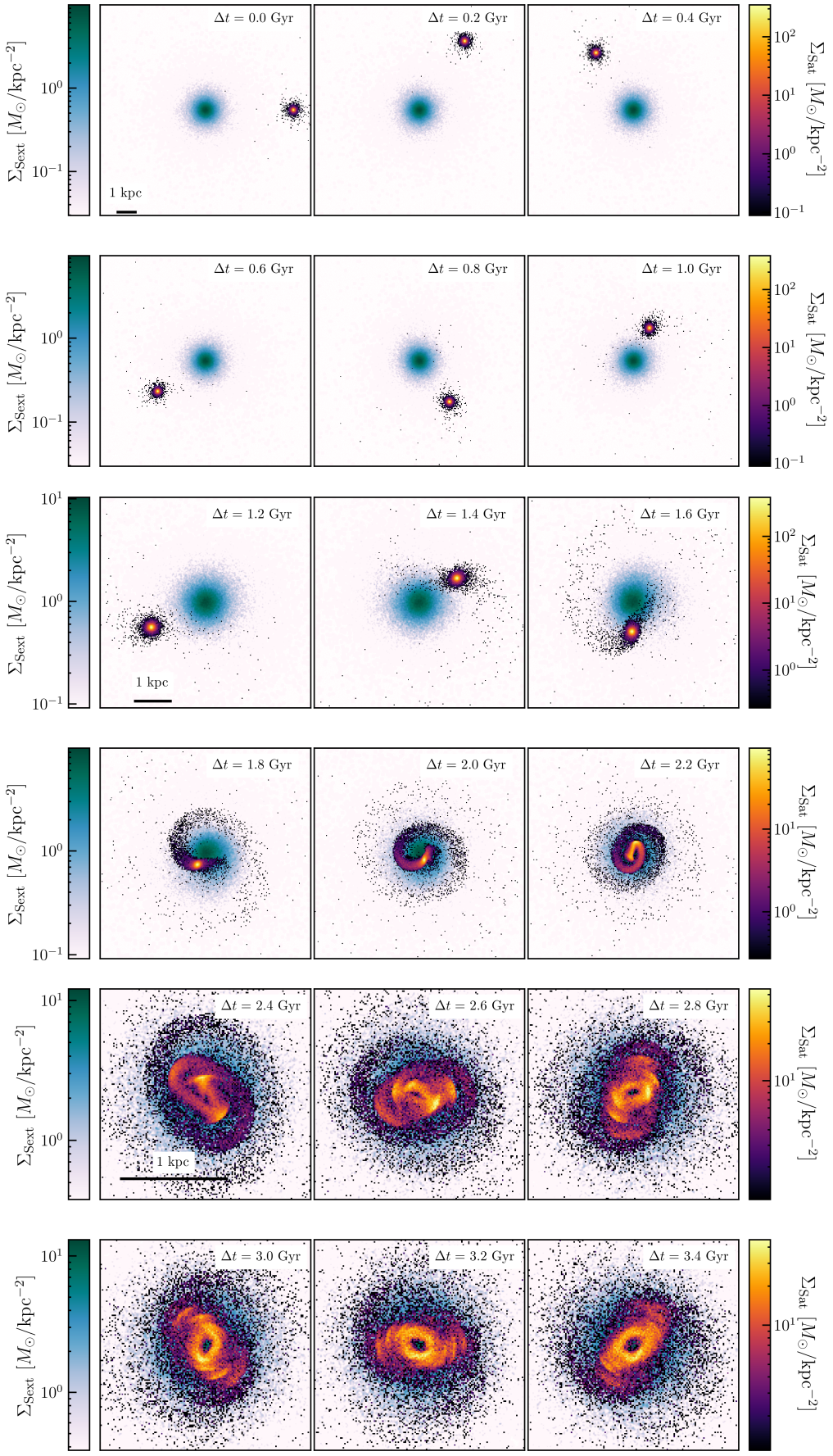

Fig. 6.9 – Case 5. 2D density maps of the Sextans+Satellite system at different times in the simulation, separated by 0.2 Gyr. Sextans and the satellite have different colour gradients to distinguish them visually.

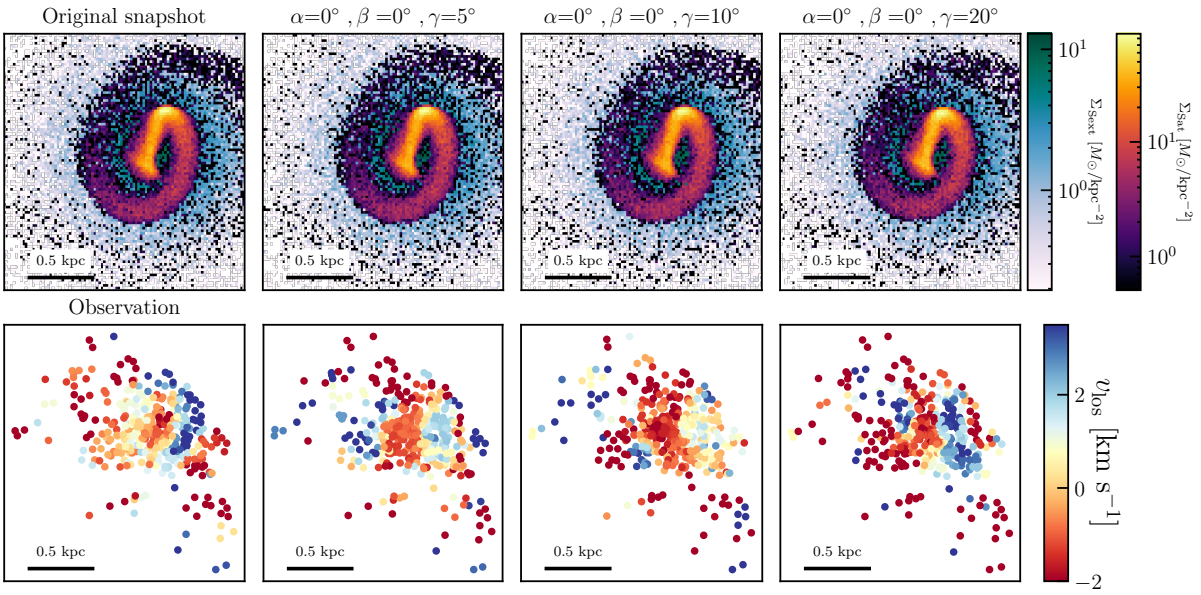

Fig. 6.10 – Case 5. Upper row: 2D density maps of the Sextans+Satellite system at 2.2 Gyr. Sextans and the satellite are shown with different colour gradients to distinguish them visually. The first image on the left shows the original line of sight from Figure 6.9, while the subsequent columns display the system viewed at different rotational angles. Lower row: Smoothed l.o.s. velocity maps. The first image on the left represents the observed dataset, while the remaining images show the mock datasets corresponding to the panels above them, with each map using the same rotational angles as the density maps in the upper row.

halo mass–concentration relation from Muñoz-Cuartas et al. (2011), I could then get an estimate for the concentration of the halo. From this estimate and for a satellite of $M_\star = 1.2 \times 10^5\, M_\odot$, the expected parameters for the halo are:

$$\begin{aligned} M_{\rm vir} &= 3 \times 10^8\, M_\odot, \\ c &= 20.39. \end{aligned} \tag{6.2}$$

These parameters are fairly compatible with the one adopted for the simulation. This appears clearly in Figure 6.12, which shows the density profile for both the cosmological motivated NFW and for the truncated NFW used in the simulation. The first one was obtained using Eq. 2.3, with the parameters in Eq. 6.2, while the truncated NFW was calculated using Eq. 4.3 and the parameters in Tab. 6.3. Indeed, up to the truncation radius, the two density profiles have very similar values, within less than a factor of two. Such a factor could be easily accounted for if one would include the typical large scatter of the stellar-to-halo mass relation.

Therefore, I have proved that a minor merger with the ICs shown in Figure 6.8 not only is able to reproduce the peculiar ring-like feature observed by Cicuéndez and Battaglia (2018) in the kinematics of Sextans, but also that such a configuration is allowed by cosmological considerations.

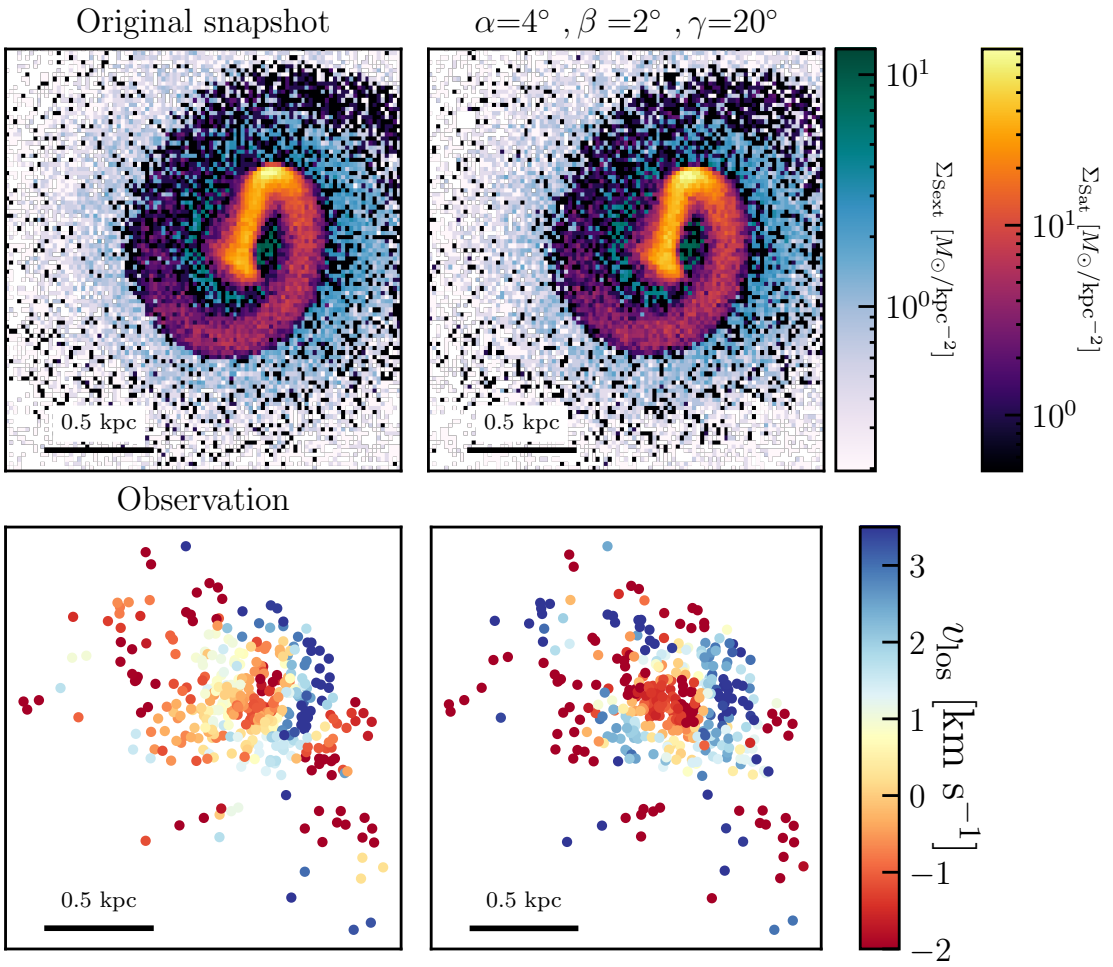

Fig. 6.11 – Case 5. Upper row: 2D density maps of the Sextans+Satellite system at 2.2 Gyr. Sextans and the satellite are shown with different colour gradients to distinguish them visually. The image on the left shows the original line of sight from Figure 6.9, while the one on the right display the rotated system. Lower row: Smoothed l.o.s. velocity maps. The image on the left represents the observed dataset, while the one on the right show the mock datasets corresponding to the panel above

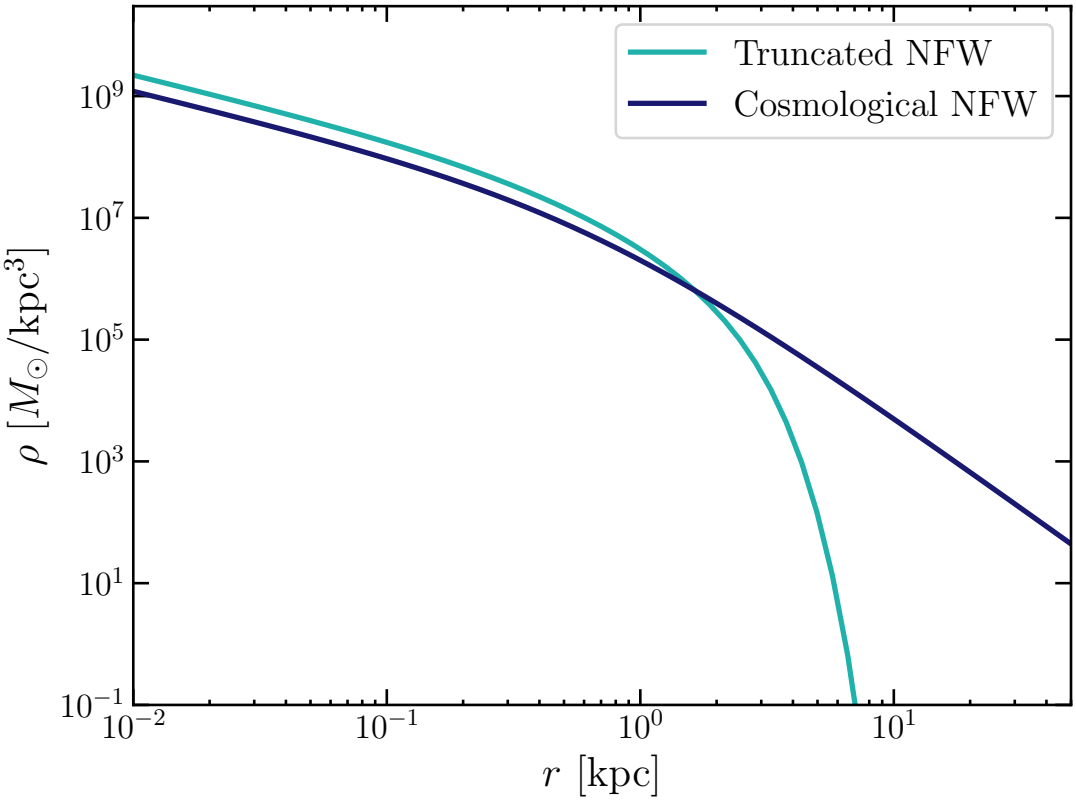

Fig. 6.12 – Mass density profile for the truncated NFW DM halo of the Case 5 satellite (light blue curve) compared to the cosmologically motivated NFW profile (dark blue line).

Conclusions and future prospects

This thesis explores whether the observed ring-like feature in the l.o.s. velocity map of the Sextans dSph o Sextans (Cicuéndez and Battaglia, 2018), obtained from state-of-the-art spectroscopic measurements of Sextans most probable members, could be due to a minor merger. Through a series of N-body simulations, I test the hypothesis that a satellite, composed either solely of stars or of both stars and DM, might have been accreted by Sextans, leading to the formation of such a feature in its inner regions.

A significant part of this project involves the generation of realistic N-body realisations for Sextans and its satellite. This process requires sample ICs that accurately represent the dynamical and structural properties of these systems. To this scope, I develop a Python code to generate spherically symmetric, steady-state samples of N particles using methods based on the DF of equilibrium models. The method is then validated by checking that the mass density and velocity dispersion profiles of the generated samples match the theoretical ones and remain stable over time. In order to do so, the systems are evolved in isolation using the N-body code Arepo and I demonstrate that the profiles of the generated samples remain consistent with the theoretical ones over time.

Employing the Arepo code, I explore two types of simulations, one where the satellite is solely composed of stars, and one where stars are embedded in a dominant DM halo. To compare the outcomes of the simulations with the observations, I create mock datasets by selecting stars in the simulations closer to the position of the observed one and smoothing the l.o.s. velocity with the same technique adopted by Cicuéndez and Battaglia (2018). Additionally, for each simulation, I inspect different timesteps and a variety of different orientations of the Sextans+Satellite system.

The satellite in the DM-free case is intended to reproduce a disrupted nuclear star cluster or a globular cluster. In this scenario, the only simulation that produces a l.o.s. velocity map comparable to the observed one is the one in which the satellite is placed on a circular orbit within the inner region of the galaxy. However, this scenario poses a challenge for the physical interpretation, as all simulations involving a DM-free satellite initially positioned at the outskirts of Sextans fail to reproduce the target ring-like structure. As a matter of fact, the simulations show that when the satellite is set on an eccentric orbit, even though the stars of the satellite lost due to tidal interactions produce a ring-like feature in the surface density map of Sextans, the resulting l.o.s. velocity maps have amplitudes at least one order of magnitude larger than the observed one. These outcomes suggest that the satellite must have a DM component to prevent its disruption during the early phases of infall and maintain relatively low velocities while passing at the pericentre.

Subsequently, I investigate scenarios where the satellite is embedded in a DM halo, in which the satellite is intended to resemble a dwarf satellite galaxy. I investigate different scenarios characterised by varying DM halo mass of the satellite and I demonstrate that a

satellite with a stellar-to-dynamical mass ratio $\sim 10^2$ can reproduce the ring-like velocity structure seen in Sextans, once suitable orbital ICs are chosen. The value for the DM halo allows the satellite to be tidally disrupted only when it reaches the inner regions of the galaxy, producing a kinematic feature consistent with observations.

The results of this thesis demonstrate that the velocity ring-like structure in Sextans can indeed be attributed to an accretion event involving a satellite with a DM halo. This brings evidence to support the hypothesis of hierarchical merging at the scale of DGs.

The work presented in this thesis is expected to be expanded in future research by exploring three different directions.

Automating the comparison process. The best matching configuration was found by visually inspecting a wide range of l.o.s., i.e. by rotating the simulated system for many different combinations of the rotation angles (α, β, γ). However, with this approach, the procedure results to be extremely time consuming, thus limiting the range of inspected angles. By automating this method, one could achieve a more efficient, less time-consuming, and objective analysis across multiple simulations. To achieve this, the idea is to employ the χ^2-fit. When comparing the observed velocity map with mock datasets, the χ^2 can be calculated as follows:

$$\chi^2 = \sum_{i=1}^{k} \frac{(v_{i,\mathrm{sim}} - v_{i,\mathrm{obs}})^2}{(\Delta v_{i,\mathrm{obs}})^2}, \tag{6.3}$$

where k is the total number of stars in the observations, and the index i denotes the i-th observed star. In this formula, $v_{i,\mathrm{obs}}$ is the measured l.o.s. velocity, $\Delta v_{i,\mathrm{obs}}$ is the uncertainty on the $v_{i,\mathrm{obs}}$ and $v_{i,\mathrm{sim}}$ is the l.o.s. velocity of the selected star in the simulation. Since the χ^2 quantifies the difference between the observed and simulated data, minimising the χ^2 value identifies the simulation configuration whose velocity distribution most closely resembles the observed one.

Varying the stars selection In this thesis, to create the mock dataset from the simulations, I first aligned the centre of mass of the simulated system with the inferred centre of Sextans. Then, I selected the simulated stars that were closest to the positions of the observed ones.

A novel approach, based on random selections, could be examined in a future work. In particular, for each observed star located at a position x_i, it can be defined a region around x_i with a size corresponding to the positional uncertainty. Then, within this region, one could randomly select stars from the simulation and study how the mock l.o.s. velocity map changes for different random selections of stars within each area.

Reproduce the metallicity structure The observed metallicity distribution in Sextans shows an intriguing pattern that complements the velocity ring (Cicuéndez and Battaglia, 2018). A future extension of this thesis project aims to jointly replicate the observed ring-like features in the observed velocity and metallicity spatial distributions.

In practice, this could be achieved by assigning metallicity values to each star in the simulation *a posteriori*. These values would be sampled separately for the stars in Sextans

and those in the satellite, based on the two Gaussian metallicity distributions found by Cicuéndez and Battaglia (2018). With this approach, mock metallicity maps, to compare with observations, could be generated without needing to run additional simulations. This method is justified by the fact that the Sextans stellar population consists entirely of very old, metal-poor stars, and no detectable gas has been found in the galaxy. Therefore, gas processes and stellar feedback during the satellite's accretion are likely negligible, meaning that the metallicity of each star in the simulation remains constant over time.

These improvements could unveil more intricate details of the system's dynamical evolution and provide a more comprehensive understanding of the merger history of the galaxy.

I

Appendix A

1.1 Eulerian angles

The matrix A describing a rotation by an angle α about the z-axis is given by

$$A = \begin{pmatrix} \cos\alpha & -\sin\alpha & 0 \\ \sin\alpha & \cos\alpha & 0 \\ 0 & 0 & 1 \end{pmatrix} \tag{A.1}$$

Similarly, the rotation matrices B and C, for rotations by angle β about the x-axis and γ about the y-axis, are

$$B = \begin{pmatrix} 1 & 0 & 0 \\ 0 & \cos\beta & -\sin\beta \\ 0 & \sin\beta & \cos\beta \end{pmatrix} \tag{A.2}$$

$$C = \begin{pmatrix} \cos\gamma & 0 & \sin\gamma \\ 0 & 1 & 0 \\ -\sin\gamma & 0 & \cos\gamma \end{pmatrix} \tag{A.3}$$

To rotate a vector by the Eulerian angles (α, β, γ), it is necessary to apply the transformation:

$$\begin{pmatrix} x' \\ y' \\ z' \end{pmatrix} = ABC \begin{pmatrix} x \\ y \\ z \end{pmatrix}, \tag{A.4}$$

where the product ABC represents the combined rotation by the three Euler angles. Since matrix multiplication is not commutative, changing the order of the rotations will lead to a different final orientation.

Bibliography

N. C. Amorisco and N. W. Evans. Dark matter cores and cusps: the case of multiple stellar populations in dwarf spheroidals. MNRAS, 419(1):184–196, Jan. 2012. doi:10.1111/j.1365-2966.2011.19684.x.

N. C. Amorisco, N. W. Evans, and G. van de Ven. The remnant of a merger between two dwarf galaxies in Andromeda II. Nature, 507(7492):335–337, Mar. 2014. doi:10.1038/nature12995.

B. J. Anthony-Twarog, J. B. Laird, D. Payne, and B. A. Twarog. CA II H and K Filter Photometry on the UVBY System. I. The Standard System. AJ, 101:1902, May 1991. doi:10.1086/115815.

J. Barnes and P. Hut. A hierarchical O(N log N) force-calculation algorithm. Nature, 324(6096):446–449, Dec. 1986. doi:10.1038/324446a0.

G. Battaglia and C. Nipoti. Publisher Correction: Stellar dynamics and dark matter in Local Group dwarf galaxies. *Nature Astronomy*, 6:1492–1492, Dec. 2022. doi:10.1038/s41550-022-01829-2.

G. Battaglia, E. Tolstoy, A. Helmi, M. J. Irwin, B. Letarte, P. Jablonka, V. Hill, K. A. Venn, M. D. Shetrone, N. Arimoto, F. Primas, A. Kaufer, P. Francois, T. Szeifert, T. Abel, and K. Sadakane. The DART imaging and CaT survey of the Fornax dwarf spheroidal galaxy. A&A, 459(2):423–440, Nov. 2006. doi:10.1051/0004-6361:20065720.

G. Battaglia, A. Helmi, E. Tolstoy, M. Irwin, V. Hill, and P. Jablonka. The Kinematic Status and Mass Content of the Sculptor Dwarf Spheroidal Galaxy. ApJ, 681(1):L13, July 2008. doi:10.1086/590179.

G. Battaglia, E. Tolstoy, A. Helmi, M. Irwin, P. Parisi, V. Hill, and P. Jablonka. Study of the Sextans dwarf spheroidal galaxy from the DART Ca II triplet survey. MNRAS, 411(2):1013–1034, Feb. 2011. doi:10.1111/j.1365-2966.2010.17745.x.

G. Battaglia, A. Sollima, and C. Nipoti. The effect of tides on the Fornax dwarf spheroidal galaxy. MNRAS, 454(3):2401–2415, Dec. 2015. doi:10.1093/mnras/stv2096.

M. Bellazzini, F. R. Ferraro, and E. Pancino. Multiple stellar populations in the Sextans dwarf spheroidal galaxy? MNRAS, 327(1):L15–L20, Oct. 2001. doi:10.1046/j.1365-8711.2001.04889.x.

M. Bettinelli, S. L. Hidalgo, S. Cassisi, A. Aparicio, and G. Piotto. The star formation history of the Sextans dwarf spheroidal galaxy: a true fossil of the pre-reionization era. MNRAS, 476(1):71–79, May 2018. doi:10.1093/mnras/sty226.

B. Binggeli, A. Sandage, and G. A. Tammann. The luminosity function of galaxies. ARA&A, 26:509–560, Jan. 1988. doi:10.1146/annurev.aa.26.090188.002453.

J. Binney and S. Tremaine. *Galactic Dynamics: Second Edition*. 2008.

M. A. Breddels and A. Helmi. Complexity on Dwarf Galaxy Scales: A Bimodal Distribution Function in Sculptor. ApJ, 791(1):L3, Aug. 2014. doi:10.1088/2041-8205/791/1/L3.

T. M. Brown, J. Tumlinson, M. Geha, J. D. Simon, L. C. Vargas, D. A. VandenBerg, E. N. Kirby, J. S. Kalirai, R. J. Avila, M. Gennaro, H. C. Ferguson, R. R. Muñoz, P. Guhathakurta, and A. Renzini. The Quenching of the Ultra-faint Dwarf Galaxies in the Reionization Era. ApJ, 796(2):91, Dec. 2014. doi:10.1088/0004-637X/796/2/91.

W. R. Brown, M. G. Lattanzi, S. J. Kenyon, and M. J. Geller. Gaia and the Galactic Center Origin of Hypervelocity Stars. ApJ, 866(1):39, Oct. 2018. doi:10.3847/1538-4357/aadb8e.

J. S. Bullock and M. Boylan-Kolchin. Small-Scale Challenges to the ΛCDM Paradigm. ARA&A, 55(1): 343–387, Aug. 2017. doi:10.1146/annurev-astro-091916-055313.

J. S. Bullock, A. V. Kravtsov, and D. H. Weinberg. Reionization and the Abundance of Galactic Satellites. ApJ, 539(2):517–521, Aug. 2000. doi:10.1086/309279.

L. Cicuéndez and G. Battaglia. Appearances can be deceiving: clear signs of accretion in the seemingly ordinary Sextans dSph. MNRAS, 480(1):251–260, Oct. 2018. doi:10.1093/mnras/sty1748.

L. Cicuéndez, G. Battaglia, M. Irwin, J. R. Bermejo-Climent, B. McMonigal, N. F. Bate, G. F. Lewis, A. R. Conn, T. J. L. de Boer, C. Gallart, M. Guglielmo, R. Ibata, A. McConnachie, E. Tolstoy, and N. Fernando. Tracing the stellar component of low surface brightness Milky Way dwarf galaxies to their outskirts. I. Sextans. A&A, 609:A53, Jan. 2018. doi:10.1051/0004-6361/201731450.

L. Ciotti and G. Bertin. Analytical properties of the $R^{1/m}$ law. A&A, 352:447–451, Dec. 1999. doi:10.48550/arXiv.astro-ph/9911078.

M. Coleman, G. S. Da Costa, J. Bland-Hawthorn, D. Martínez-Delgado, K. C. Freeman, and D. Malin. Shell Structure in the Fornax Dwarf Spheroidal Galaxy. AJ, 127(2):832–839, Feb. 2004. doi:10.1086/381298.

J. W. Cooley and J. W. Tukey. An algorithm for the machine calculation of complex fourier series. *Mathematics of Computation*, 19(90):297–301, 1965. doi:10.1090/S0025-5718-1965-0178586-1.

T. Costa, R. Pakmor, and V. Springel. Powering galactic superwinds with small-scale AGN winds. MNRAS, 497(4):5229–5255, Oct. 2020. doi:10.1093/mnras/staa2321.

de Boer, T. J. L., Tolstoy, E., Lemasle, B., Saha, A., Olszewski, E. W., Mateo, M., Irwin, M. J., and Battaglia, G. The episodic star formation history of the carina dwarf spheroidal galaxy. A&A, 572:A10, 2014. doi:10.1051/0004-6361/201424119. URL https://doi.org/10.1051/0004-6361/201424119.

G. de Vaucouleurs. Recherches sur les Nebuleuses Extragalactiques. *Annales d'Astrophysique*, 11:247, Jan. 1948.

A. Deason, A. Wetzel, and S. Garrison-Kimmel. Satellite Dwarf Galaxies in a Hierarchical Universe: The Prevalence of Dwarf-Dwarf Major Mergers. ApJ, 794(2):115, Oct. 2014. doi:10.1088/0004-637X/794/2/115.

W. Dehnen. A Family of Potential-Density Pairs for Spherical Galaxies and Bulges. MNRAS, 265:250, Nov. 1993. doi:10.1093/mnras/265.1.250.

A. del Pino, A. Aparicio, and S. L. Hidalgo. Merger traces in the spatial distribution of stellar populations in the Fornax dSph galaxy. MNRAS, 454(4):3996–4012, Dec. 2015. doi:10.1093/mnras/stv2174.

A. Drlica-Wagner, K. Bechtol, E. S. Rykoff, E. Luque, A. Queiroz, Y. Y. Mao, R. H. Wechsler, J. D. Simon, B. Santiago, B. Yanny, E. Balbinot, S. Dodelson, A. Fausti Neto, D. J. James, T. S. Li, M. A. G. Maia, J. L. Marshall, A. Pieres, K. Stringer, A. R. Walker, T. M. C. Abbott, F. B. Abdalla, S. Allam, A. Benoit-Lévy, G. M. Bernstein, E. Bertin, D. Brooks, E. Buckley-Geer, D. L. Burke, A. Carnero Rosell, M. Carrasco Kind, J. Carretero, M. Crocce, L. N. da Costa, S. Desai, H. T. Diehl, J. P. Dietrich, P. Doel, T. F. Eifler, A. E. Evrard, D. A. Finley, B. Flaugher, P. Fosalba, J. Frieman, E. Gaztanaga, D. W. Gerdes, D. Gruen, R. A. Gruendl, G. Gutierrez, K. Honscheid, K. Kuehn, N. Kuropatkin, O. Lahav, P. Martini, R. Miquel, B. Nord, R. Ogando, A. A. Plazas, K. Reil, A. Roodman, M. Sako, E. Sanchez, V. Scarpine, M. Schubnell, I. Sevilla-Noarbe, R. C. Smith, M. Soares-Santos, F. Sobreira,

E. Suchyta, M. E. C. Swanson, G. Tarle, D. Tucker, V. Vikram, W. Wester, Y. Zhang, J. Zuntz, and DES Collaboration. Eight Ultra-faint Galaxy Candidates Discovered in Year Two of the Dark Energy Survey. ApJ, 813(2):109, Nov. 2015. doi:10.1088/0004-637X/813/2/109.

G. Efstathiou. Suppressing the formation of dwarf galaxies via photoionization. MNRAS, 256(2):43P–47P, May 1992. doi:10.1093/mnras/256.1.43P.

R. Errani, J. Peñarrubia, and M. G. Walker. Systematics in virial mass estimators for pressure-supported systems. MNRAS, 481(4):5073–5090, Dec. 2018. doi:10.1093/mnras/sty2505.

M. Fabrizio, G. Bono, M. Nonino, E. L. Łokas, I. Ferraro, G. Iannicola, R. Buonanno, S. Cassisi, G. Coppola, M. Dall'Ora, R. Gilmozzi, M. Marconi, M. Monelli, M. Romaniello, P. B. Stetson, F. Thévenin, and A. R. Walker. The Carina Project. X. On the Kinematics of Old and Intermediate-age Stellar Populations1,2. ApJ, 830(2):126, Oct. 2016. doi:10.3847/0004-637X/830/2/126.

O. Fakhouri, C.-P. Ma, and M. Boylan-Kolchin. The merger rates and mass assembly histories of dark matter haloes in the two Millennium simulations. MNRAS, 406(4):2267–2278, Aug. 2010. doi:10.1111/j.1365-2966.2010.16859.x.

S. P. Fillingham, M. C. Cooper, C. Wheeler, S. Garrison-Kimmel, M. Boylan-Kolchin, and J. S. Bullock. Taking care of business in a flash: constraining the time-scale for low-mass satellite quenching with ELVIS. MNRAS, 454(2):2039–2049, Dec. 2015. doi:10.1093/mnras/stv2058.

S. P. Fillingham, M. C. Cooper, A. B. Pace, M. Boylan-Kolchin, J. S. Bullock, S. Garrison-Kimmel, and C. Wheeler. Under pressure: quenching star formation in low-mass satellite galaxies via stripping. MNRAS, 463(2):1916–1928, Dec. 2016. doi:10.1093/mnras/stw2131.

S. P. Fillingham, M. C. Cooper, M. Boylan-Kolchin, J. S. Bullock, S. Garrison-Kimmel, and C. Wheeler. Environmental quenching of low-mass field galaxies. MNRAS, 477(4):4491–4498, July 2018. doi:10.1093/mnras/sty958.

F. Fraternali, E. Tolstoy, M. J. Irwin, and A. A. Cole. Life at the periphery of the Local Group: the kinematics of the Tucana dwarf galaxy. A&A, 499(1):121–128, May 2009. doi:10.1051/0004-6361/200810830.

C. S. Frenk, S. D. M. White, and M. Davis. Nonlinear evolution of large-scale structure in the universe. ApJ, 271:417–430, Aug. 1983. doi:10.1086/161209.

Gaia Collaboration, T. Prusti, J. H. J. de Bruijne, A. G. A. Brown, A. Vallenari, C. Babusiaux, C. A. L. Bailer-Jones, U. Bastian, M. Biermann, D. W. Evans, L. Eyer, F. Jansen, C. Jordi, S. A. Klioner, U. Lammers, L. Lindegren, X. Luri, F. Mignard, D. J. Milligan, C. Panem, V. Poinsignon, D. Pourbaix, S. Randich, G. Sarri, P. Sartoretti, H. I. Siddiqui, C. Soubiran, V. Valette, F. van Leeuwen, N. A. Walton, C. Aerts, F. Arenou, M. Cropper, R. Drimmel, E. Høg, D. Katz, M. G. Lattanzi, W. O'Mullane, E. K. Grebel, A. D. Holland, C. Huc, X. Passot, L. Bramante, C. Cacciari, J. Castañeda, L. Chaoul, N. Cheek, F. De Angeli, C. Fabricius, R. Guerra, J. Hernández, A. Jean-Antoine-Piccolo, E. Masana, R. Messineo, N. Mowlavi, K. Nienartowicz, D. Ordóñez-Blanco, P. Panuzzo, J. Portell, P. J. Richards, M. Riello, G. M. Seabroke, P. Tanga, F. Thévenin, J. Torra, S. G. Els, G. Gracia-Abril, G. Comoretto, M. Garcia-Reinaldos, T. Lock, E. Mercier, M. Altmann, R. Andrae, T. L. Astraatmadja, I. Bellas-Velidis, K. Benson, J. Berthier, R. Blomme, G. Busso, B. Carry, A. Cellino, G. Clementini, S. Cowell, O. Creevey, J. Cuypers, M. Davidson, J. De Ridder, A. de Torres, L. Delchambre, A. Dell'Oro, C. Ducourant, Y. Frémat, M. García-Torres, E. Gosset, J. L. Halbwachs, N. C. Hambly, D. L. Harrison, M. Hauser, D. Hestroffer, S. T. Hodgkin, H. E. Huckle, A. Hutton, G. Jasniewicz, S. Jordan, M. Kontizas, A. J. Korn, A. C. Lanzafame, M. Manteiga, A. Moitinho, K. Muinonen, J. Osinde, E. Pancino, T. Pauwels, J. M. Petit, A. Recio-Blanco, A. C. Robin, L. M. Sarro, C. Siopis, M. Smith, K. W. Smith, A. Sozzetti, W. Thuillot, W. van Reeven, Y. Viala, U. Abbas, A. Abreu Aramburu,

S. Accart, J. J. Aguado, P. M. Allan, W. Allasia, G. Altavilla, M. A. Álvarez, J. Alves, R. I. Anderson, A. H. Andrei, E. Anglada Varela, E. Antiche, T. Antoja, S. Antón, B. Arcay, A. Atzei, L. Ayache, N. Bach, S. G. Baker, L. Balaguer-Núñez, C. Barache, C. Barata, A. Barbier, F. Barblan, M. Baroni, D. Barrado y Navascués, M. Barros, M. A. Barstow, U. Becciani, M. Bellazzini, G. Bellei, A. Bello García, V. Belokurov, P. Bendjoya, A. Berihuete, L. Bianchi, O. Bienaymé, F. Billebaud, N. Blagorodnova, S. Blanco-Cuaresma, T. Boch, A. Bombrun, R. Borrachero, S. Bouquillon, G. Bourda, H. Bouy, A. Bragaglia, M. A. Breddels, N. Brouillet, T. Brüsemeister, B. Bucciarelli, F. Budnik, P. Burgess, R. Burgon, A. Burlacu, D. Busonero, R. Buzzi, E. Caffau, J. Cambras, H. Campbell, R. Cancelliere, T. Cantat-Gaudin, T. Carlucci, J. M. Carrasco, M. Castellani, P. Charlot, J. Charnas, P. Charvet, F. Chassat, A. Chiavassa, M. Clotet, G. Cocozza, R. S. Collins, P. Collins, G. Costigan, F. Crifo, N. J. G. Cross, M. Crosta, C. Crowley, C. Dafonte, Y. Damerdji, A. Dapergolas, P. David, M. David, P. De Cat, F. de Felice, P. de Laverny, F. De Luise, R. De March, D. de Martino, R. de Souza, J. Debosscher, E. del Pozo, M. Delbo, A. Delgado, H. E. Delgado, F. di Marco, P. Di Matteo, S. Diakite, E. Distefano, C. Dolding, S. Dos Anjos, P. Drazinos, J. Durán, Y. Dzigan, E. Ecale, B. Edvardsson, H. Enke, M. Erdmann, D. Escolar, M. Espina, N. W. Evans, G. Eynard Bontemps, C. Fabre, M. Fabrizio, S. Faigler, A. J. Falcão, M. Farràs Casas, F. Faye, L. Federici, G. Fedorets, J. Fernández-Hernández, P. Fernique, A. Fienga, F. Figueras, F. Filippi, K. Findeisen, A. Fonti, M. Fouesneau, E. Fraile, M. Fraser, J. Fuchs, R. Furnell, M. Gai, S. Galleti, L. Galluccio, D. Garabato, F. García-Sedano, P. Garé, A. Garofalo, N. Garralda, P. Gavras, J. Gerssen, R. Geyer, G. Gilmore, S. Girona, G. Giuffrida, M. Gomes, A. González-Marcos, J. González-Núñez, J. J. González-Vidal, M. Granvik, A. Guerrier, P. Guillout, J. Guiraud, A. Gúrpide, R. Gutiérrez-Sánchez, L. P. Guy, R. Haigron, D. Hatzidimitriou, M. Haywood, U. Heiter, A. Helmi, D. Hobbs, W. Hofmann, B. Holl, G. Holland, J. A. S. Hunt, A. Hypki, V. Icardi, M. Irwin, G. Jevardat de Fombelle, P. Jofré, P. G. Jonker, A. Jorissen, F. Julbe, A. Karampelas, A. Kochoska, R. Kohley, K. Kolenberg, E. Kontizas, S. E. Koposov, G. Kordopatis, P. Koubsky, A. Kowalczyk, A. Krone-Martins, M. Kudryashova, I. Kull, R. K. Bachchan, F. Lacoste-Seris, A. F. Lanza, J. B. Lavigne, C. Le Poncin-Lafitte, Y. Lebreton, T. Lebzelter, S. Leccia, N. Leclerc, I. Lecoeur-Taibi, V. Lemaitre, H. Lenhardt, F. Leroux, S. Liao, E. Licata, H. E. P. Lindstrøm, T. A. Lister, E. Livanou, A. Lobel, W. Löffler, M. López, A. Lopez-Lozano, D. Lorenz, T. Loureiro, I. MacDonald, T. Magalhães Fernandes, S. Managau, R. G. Mann, G. Mantelet, O. Marchal, J. M. Marchant, M. Marconi, J. Marie, S. Marinoni, P. M. Marrese, G. Marschalkó, D. J. Marshall, J. M. Martín-Fleitas, M. Martino, N. Mary, G. Matijevič, T. Mazeh, P. J. McMillan, S. Messina, A. Mestre, D. Michalik, N. R. Millar, B. M. H. Miranda, D. Molina, R. Molinaro, M. Molinaro, L. Molnár, M. Moniez, P. Montegriffo, D. Monteiro, R. Mor, A. Mora, R. Morbidelli, T. Morel, S. Morgenthaler, T. Morley, D. Morris, A. F. Mulone, T. Muraveva, I. Musella, J. Narbonne, G. Nelemans, L. Nicastro, L. Noval, C. Ordénovic, J. Ordieres-Meré, P. Osborne, C. Pagani, I. Pagano, F. Pailler, H. Palacin, L. Palaversa, P. Parsons, T. Paulsen, M. Pecoraro, R. Pedrosa, H. Pentikäinen, J. Pereira, B. Pichon, A. M. Piersimoni, F. X. Pineau, E. Plachy, G. Plum, E. Poujoulet, A. Prša, L. Pulone, S. Ragaini, S. Rago, N. Rambaux, M. Ramos-Lerate, P. Ranalli, G. Rauw, A. Read, S. Regibo, F. Renk, C. Reylé, R. A. Ribeiro, L. Rimoldini, V. Ripepi, A. Riva, G. Rixon, M. Roelens, M. Romero-Gómez, N. Rowell, F. Royer, A. Rudolph, L. Ruiz-Dern, G. Sadowski, T. Sagristà Sellés, J. Sahlmann, J. Salgado, E. Salguero, M. Sarasso, H. Savietto, A. Schnorhk, M. Schultheis, E. Sciacca, M. Segol, J. C. Segovia, D. Segransan, E. Serpell, I. C. Shih, R. Smareglia, R. L. Smart, C. Smith, E. Solano, F. Solitro, R. Sordo, S. Soria Nieto, J. Souchay, A. Spagna, F. Spoto, U. Stampa, I. A. Steele, H. Steidelmüller, C. A. Stephenson, H. Stoev, F. F. Suess, M. Süveges, J. Surdej, L. Szabados, E. Szegedi-Elek, D. Tapiador, F. Taris, G. Tauran, M. B. Taylor, R. Teixeira, D. Terrett, B. Tingley, S. C. Trager, C. Turon, A. Ulla, E. Utrilla, G. Valentini, A. van Elteren, E. Van Hemelryck, M. van Leeuwen, M. Varadi, A. Vecchiato, J. Veljanoski, T. Via, D. Vicente, S. Vogt, H. Voss, V. Votruba, S. Voutsinas, G. Walmsley, M. Weiler, K. Weingrill, D. Werner, T. Wevers, G. Whitehead, Ł. Wyrzykowski, A. Yoldas, M. Žerjal, S. Zucker, C. Zurbach, T. Zwitter, A. Alecu, M. Allen, C. Allende Prieto, A. Amorim, G. Anglada-Escudé, V. Arsenijevic, S. Azaz, P. Balm, M. Beck, H. H. Bernstein, L. Bigot, A. Bijaoui, C. Blasco, M. Bonfigli, G. Bono, S. Boudreault, A. Bressan, S. Brown, P. M. Brunet, P. Bunclark, R. Buonanno, A. G. Butkevich, C. Carret, C. Carrion, L. Chemin, F. Chéreau, L. Corcione, E. Darmigny, K. S. de Boer, P. de Teodoro, P. T. de Zeeuw, C. Delle Luche, C. D.

Domingues, P. Dubath, F. Fodor, B. Frézouls, A. Fries, D. Fustes, D. Fyfe, E. Gallardo, J. Gallegos, D. Gardiol, M. Gebran, A. Gomboc, A. Gómez, E. Grux, A. Gueguen, A. Heyrovsky, J. Hoar, G. Iannicola, Y. Isasi Parache, A. M. Janotto, E. Joliet, A. Jonckheere, R. Keil, D. W. Kim, P. Klagyivik, J. Klar, J. Knude, O. Kochukhov, I. Kolka, J. Kos, A. Kutka, V. Lainey, D. LeBouquin, C. Liu, D. Loreggia, V. V. Makarov, M. G. Marseille, C. Martayan, O. Martinez-Rubi, B. Massart, F. Meynadier, S. Mignot, U. Munari, A. T. Nguyen, T. Nordlander, P. Ocvirk, K. S. O'Flaherty, A. Olias Sanz, P. Ortiz, J. Osorio, D. Oszkiewicz, A. Ouzounis, M. Palmer, P. Park, E. Pasquato, C. Peltzer, J. Peralta, F. Péturaud, T. Pieniluoma, E. Pigozzi, J. Poels, G. Prat, T. Prod'homme, F. Raison, J. M. Rebordao, D. Risquez, B. Rocca-Volmerange, S. Rosen, M. I. Ruiz-Fuertes, F. Russo, S. Sembay, I. Serraller Vizcaino, A. Short, A. Siebert, H. Silva, D. Sinachopoulos, E. Slezak, M. Soffel, D. Sosnowska, V. Straižys, M. ter Linden, D. Terrell, S. Theil, C. Tiede, L. Troisi, P. Tsalmantza, D. Tur, M. Vaccari, F. Vachier, P. Valles, W. Van Hamme, L. Veltz, J. Virtanen, J. M. Wallut, R. Wichmann, M. I. Wilkinson, H. Ziaeepour, and S. Zschocke. The Gaia mission. A&A, 595:A1, Nov. 2016. doi:10.1051/0004-6361/201629272.

M. Goon Lee, H. S. Park, J.-H. Park, Y.-J. Sohn, S. J. Oh, I.-S. Yuk, S.-C. Rey, S.-G. Lee, Y.-W. Lee, H.-I. Kim, W. Han, W.-K. Park, J. Hyeop Lee, Y. B. Jeon, and S. C. Kim. Deep Wide Field BVI CCD Photometry of the Sextans Dwarf Spheroidal Galaxy. *arXiv e-prints*, art. astro-ph/0308469, Aug. 2003. doi:10.48550/arXiv.astro-ph/0308469.

R. J. J. Grand, F. A. Gómez, F. Marinacci, R. Pakmor, V. Springel, D. J. R. Campbell, C. S. Frenk, A. Jenkins, and S. D. M. White. The Auriga Project: the properties and formation mechanisms of disc galaxies across cosmic time. MNRAS, 467(1):179–207, May 2017. doi:10.1093/mnras/stx071.

B. F. Griffen, A. P. Ji, G. A. Dooley, F. A. Gómez, M. Vogelsberger, B. W. O'Shea, and A. Frebel. The Caterpillar Project: A Large Suite of Milky Way Sized Halos. ApJ, 818(1):10, Feb. 2016. doi:10.3847/0004-637X/818/1/10.

D. Harbeck, E. K. Grebel, J. Holtzman, P. Guhathakurta, W. Brandner, D. Geisler, A. Sarajedini, A. Dolphin, D. Hurley-Keller, and M. Mateo. Population Gradients in Local Group Dwarf Spheroidal Galaxies. AJ, 122(6):3092–3105, Dec. 2001. doi:10.1086/324232.

K. Hayashi, M. Chiba, and T. Ishiyama. Diversity of Dark Matter Density Profiles in the Galactic Dwarf Spheroidal Satellites. ApJ, 904(1):45, Nov. 2020. doi:10.3847/1538-4357/abbe0a.

A. Helmi, L. V. Sales, E. Starkenburg, T. K. Starkenburg, C. A. Vera-Ciro, G. De Lucia, and Y. S. Li. Dark Satellites and the Morphology of Dwarf Galaxies. ApJ, 758(1):L5, Oct. 2012. doi:10.1088/2041-8205/758/1/L5.

L. Hernquist. An Analytical Model for Spherical Galaxies and Bulges. ApJ, 356:359, June 1990. doi:10.1086/168845.

L. Hernquist and P. J. Quinn. Formation of Shell Galaxies. I. Spherical Potentials. ApJ, 331:682, Aug. 1988. doi:10.1086/166592.

P. W. Hodge. The Fornax dwarf galaxy. II. The distribution of stars. AJ, 66:249, Aug. 1961. doi:10.1086/108404.

P. W. Hodge. Distribution of stars in the Draco dwarf galaxy. AJ, 69:853, Dec. 1964. doi:10.1086/109360.

G. Iorio, C. Nipoti, G. Battaglia, and A. Sollima. The effect of tides on the Sculptor dwarf spheroidal galaxy. MNRAS, 487(4):5692–5710, Aug. 2019. doi:10.1093/mnras/stz1342.

M. Irwin and D. Hatzidimitriou. Structural parameters for the Galactic dwarf spheroidals. *Monthly Notices of the Royal Astronomical Society*, 277(4):1354–1378, 12 1995. ISSN 0035-8711. doi:10.1093/mnras/277.4.1354. URL https://doi.org/10.1093/mnras/277.4.1354.

M. J. Irwin, P. S. Bunclark, M. T. Bridgeland, and R. G. McMahon. A new satellite galaxy of the Milky Way in the constellation of Sextans. MNRAS, 244:16P–19, May 1990.

H.-S. Kim, S.-I. Han, S.-J. Joo, H. Jeong, and S.-J. Yoon. A Possible Relic Star Cluster in the Sextans Dwarf Galaxy. ApJ, 870(1):L8, Jan. 2019. doi:10.3847/2041-8213/aaf885.

I. King. The structure of star clusters. I. an empirical density law. AJ, 67:471, Oct. 1962. doi:10.1086/108756.

E. N. Kirby, J. S. Bullock, M. Boylan-Kolchin, M. Kaplinghat, and J. G. Cohen. The dynamics of isolated Local Group galaxies. MNRAS, 439(1):1015–1027, Mar. 2014. doi:10.1093/mnras/stu025.

A. A. Klypin and S. F. Shandarin. Three-dimensional numerical model of the formation of large-scale structure in the Universe. MNRAS, 204:891–907, Sept. 1983. doi:10.1093/mnras/204.3.891.

G. Kordopatis, N. C. Amorisco, N. W. Evans, G. Gilmore, and S. E. Koposov. Chemodynamic subpopulations of the Carina dwarf galaxy. MNRAS, 457(2):1299–1307, Apr. 2016. doi:10.1093/mnras/stw073.

E. L. Łokas. The mass and velocity anisotropy of the Carina, Fornax, Sculptor and Sextans dwarf spheroidal galaxies. MNRAS, 394(1):L102–L106, Mar. 2009. doi:10.1111/j.1745-3933.2009.00620.x.

D. Marchesini, E. D'Onghia, G. Chincarini, C. Firmani, P. Conconi, E. Molinari, and A. Zacchei. Hα Rotation Curves: The Soft Core Question. ApJ, 575(2):801–813, Aug. 2002. doi:10.1086/341475.

F. Marinacci, M. Vogelsberger, R. Pakmor, P. Torrey, V. Springel, L. Hernquist, D. Nelson, R. Weinberger, A. Pillepich, J. Naiman, and S. Genel. First results from the IllustrisTNG simulations: radio haloes and magnetic fields. MNRAS, 480(4):5113–5139, Nov. 2018. doi:10.1093/mnras/sty2206.

D. Massari, M. A. Breddels, A. Helmi, L. Posti, A. G. A. Brown, and E. Tolstoy. Three-dimensional motions in the Sculptor dwarf galaxy as a glimpse of a new era. *Nature Astronomy*, 2:156–161, Nov. 2018. doi:10.1038/s41550-017-0322-y.

D. Massari, A. Helmi, A. Mucciarelli, L. V. Sales, L. Spina, and E. Tolstoy. Stellar 3D kinematics in the Draco dwarf spheroidal galaxy. A&A, 633:A36, Jan. 2020. doi:10.1051/0004-6361/201935613.

M. Mateo, J. Nemec, M. Irwin, and R. McMahon. Deep CCD Photometry of the Sextans Dwarf Spheroidal Galaxy. AJ, 101:892, Mar. 1991. doi:10.1086/115734.

M. Mateo, P. Fischer, and W. Krzeminski. Variable Stars in the Sextans Dwarf Spheroidal Galaxy. AJ, 110:2166, Nov. 1995. doi:10.1086/117676.

A. W. McConnachie. The Observed Properties of Dwarf Galaxies in and around the Local Group. AJ, 144(1):4, July 2012. doi:10.1088/0004-6256/144/1/4.

S. S. McGaugh, V. C. Rubin, and W. J. G. de Blok. High-Resolution Rotation Curves of Low Surface Brightness Galaxies. I. Data. AJ, 122(5):2381–2395, Nov. 2001. doi:10.1086/323448.

D. Merritt. Distribution functions for spherical galaxies. MNRAS, 214:25P–28P, June 1985. doi:10.1093/mnras/214.1.25P.

D. Merritt. Optimal Smoothing for N-Body Codes. AJ, 111:2462, June 1996. doi:10.1086/117980.

J. C. Muñoz-Cuartas, A. V. Macciò, S. Gottlöber, and A. A. Dutton. The redshift evolution of Λ cold dark matter halo parameters: concentration, spin and shape. MNRAS, 411(1):584–594, Feb. 2011. doi:10.1111/j.1365-2966.2010.17704.x.

T. Muraveva, G. Clementini, A. Garofalo, and F. Cusano. A fresh look at the RR Lyrae population in the Draco dwarf spheroidal galaxy with Gaia. MNRAS, 499(3):4040–4053, Dec. 2020. doi:10.1093/mnras/staa2984.

J. P. Naiman, A. Pillepich, V. Springel, E. Ramirez-Ruiz, P. Torrey, M. Vogelsberger, R. Pakmor, D. Nelson, F. Marinacci, L. Hernquist, R. Weinberger, and S. Genel. First results from the IllustrisTNG simulations: a tale of two elements - chemical evolution of magnesium and europium. MNRAS, 477 (1):1206–1224, June 2018. doi:10.1093/mnras/sty618.

J. F. Navarro, C. S. Frenk, and S. D. M. White. The Structure of Cold Dark Matter Halos. *The Astrophysical Journal*, 462:563, May 1996. doi:10.1086/177173.

J. F. Navarro, A. Ludlow, V. Springel, J. Wang, M. Vogelsberger, S. D. M. White, A. Jenkins, C. S. Frenk, and A. Helmi. The diversity and similarity of simulated cold dark matter haloes. MNRAS, 402 (1):21–34, Feb. 2010. doi:10.1111/j.1365-2966.2009.15878.x.

D. Nelson, A. Pillepich, V. Springel, R. Weinberger, L. Hernquist, R. Pakmor, S. Genel, P. Torrey, M. Vogelsberger, G. Kauffmann, F. Marinacci, and J. Naiman. First results from the IllustrisTNG simulations: the galaxy colour bimodality. MNRAS, 475(1):624–647, Mar. 2018. doi:10.1093/mnras/stx3040.

C. Nipoti and J. Binney. Early flattening of dark matter cusps in dwarf spheroidal galaxies. MNRAS, 446(2):1820–1828, Jan. 2015. doi:10.1093/mnras/stu2217.

M. A. Norris, S. J. Kannappan, D. A. Forbes, A. J. Romanowsky, J. P. Brodie, F. R. Faifer, A. Huxor, C. Maraston, A. J. Moffett, S. J. Penny, V. Pota, A. Smith-Castelli, J. Strader, D. Bradley, K. D. Eckert, D. Fohring, J. McBride, D. V. Stark, and O. Vaduvescu. The AIMSS Project - I. Bridging the star cluster-galaxy divide⋆†‡§¶. MNRAS, 443(2):1151–1172, Sept. 2014. doi:10.1093/mnras/stu1186.

S. Okamoto, N. Arimoto, E. Tolstoy, P. Jablonka, M. J. Irwin, Y. Komiyama, Y. Yamada, and M. Onodera. Population gradient in the Sextans dSph: comprehensive mapping of a dwarf galaxy by Suprime-Cam. MNRAS, 467(1):208–217, May 2017. doi:10.1093/mnras/stx086.

L. P. Osipkov. Spherical systems of gravitating bodies with an ellipsoidal velocity distribution. *Soviet Astronomy Letters*, 5:42–44, Jan. 1979.

A. B. Pace, M. Kaplinghat, E. Kirby, J. D. Simon, E. Tollerud, R. R. Muñoz, P. Côté, S. G. Djorgovski, and M. Geha. Multiple chemodynamic stellar populations of the Ursa Minor dwarf spheroidal galaxy. MNRAS, 495(3):3022–3040, July 2020. doi:10.1093/mnras/staa1419.

R. Pascale, L. Posti, C. Nipoti, and J. Binney. Action-based dynamical models of dwarf spheroidal galaxies: application to Fornax. MNRAS, 480(1):927–946, Oct. 2018. doi:10.1093/mnras/sty1860.

R. Pascale, M. Bellazzini, M. Tosi, F. Annibali, F. Marinacci, and C. Nipoti. An off-centred bulge or a satellite? Hydrodynamical N-body simulations of the disc galaxy NGC 5474. MNRAS, 501(2): 2091–2111, Feb. 2021. doi:10.1093/mnras/staa3699.

R. Pascale, F. Annibali, M. Tosi, F. Marinacci, C. Nipoti, M. Bellazzini, D. Romano, E. Sacchi, A. Aloisi, and M. Cignoni. Dancing in the void: hydrodynamical N-body simulations of the extremely metal-poor galaxy DDO 68. MNRAS, 509(2):2940–2956, Jan. 2022. doi:10.1093/mnras/stab3054.

R. Pascale, F. Annibali, M. Tosi, C. Nipoti, F. Marinacci, M. Bellazzini, J. M. Cannon, L. Schisgal, E. Sacchi, and F. Calura. Beyond the surface: Hydrodynamical N-body simulations of the interacting dwarf galaxies NGC 5238 and UGC 8760. A&A, 688:A144, Aug. 2024. doi:10.1051/0004-6361/202348991.

PASTA Collaboration, N. Borghi, E. Ceccarelli, A. D. Croce, L. Leuzzi, L. Rosignoli, and A. Traina. pastamarkers: astrophysical data visualization with pasta-like markers, 2024. URL https://arxiv.org/abs/2403.20314.

P. J. E. Peebles. *The large-scale structure of the universe*. 1980.

A. Pillepich, V. Springel, D. Nelson, S. Genel, J. Naiman, R. Pakmor, L. Hernquist, P. Torrey, M. Vogelsberger, R. Weinberger, and F. Marinacci. Simulating galaxy formation with the illustristng model. *Monthly Notices of the Royal Astronomical Society*, 473(3):4077–4106, Oct. 2017. ISSN 1365-2966. doi:10.1093/mnras/stx2656. URL http://dx.doi.org/10.1093/mnras/stx2656.

H. C. Plummer. On the problem of distribution in globular star clusters. *Monthly Notices of the Royal Astronomical Society*, 71:460–470, Mar. 1911. doi:10.1093/mnras/71.5.460.

A. Pontzen and F. Governato. Cold dark matter heats up. Nature, 506(7487):171–178, Feb. 2014. doi:10.1038/nature12953.

M. E. Putman, Y. Zheng, A. M. Price-Whelan, J. Grcevich, A. C. Johnson, E. Tollerud, and J. E. G. Peek. The Gas Content and Stripping of Local Group Dwarf Galaxies. ApJ, 913(1):53, May 2021. doi:10.3847/1538-4357/abe391.

J. I. Read, M. I. Wilkinson, N. W. Evans, G. Gilmore, and J. T. Kleyna. The tidal stripping of satellites. MNRAS, 366(2):429–437, Feb. 2006. doi:10.1111/j.1365-2966.2005.09861.x.

J. I. Read, G. Iorio, O. Agertz, and F. Fraternali. The stellar mass-halo mass relation of isolated field dwarfs: a critical test of ΛCDM at the edge of galaxy formation. MNRAS, 467(2):2019–2038, May 2017. doi:10.1093/mnras/stx147.

Y. Revaz and P. Jablonka. Pushing back the limits: detailed properties of dwarf galaxies in a ΛCDM universe. A&A, 616:A96, Aug. 2018. doi:10.1051/0004-6361/201832669.

T. Ruiz-Lara, C. Gallart, M. Monelli, T. K. Fritz, G. Battaglia, S. Cassisi, M. L. Aznar, A. V. Russo Cabrera, I. Rodríguez-Martín, and J. J. Salazar-González. Dissecting the stellar content of Leo I: a dwarf irregular caught in transition. MNRAS, 501(3):3962–3980, Mar. 2021. doi:10.1093/mnras/staa3871.

J. Sérsic. Influence of the atmospheric and instrumental dispersion on the brightness distribution in a galaxy. *Boletin de la Asociacion Argentina de Astronomia La Plata Argentina*, 6:41–43, Feb. 1963.

J. D. Simon. The Faintest Dwarf Galaxies. ARA&A, 57:375–415, Aug. 2019. doi:10.1146/annurev-astro-091918-104453.

M. E. Spencer, M. Mateo, M. G. Walker, E. W. Olszewski, A. W. McConnachie, E. N. Kirby, and A. Koch. The Binary Fraction of Stars in Dwarf Galaxies: The Case of Leo II. AJ, 153(6):254, June 2017. doi:10.3847/1538-3881/aa6d51.

V. Springel. E pur si muove: Galilean-invariant cosmological hydrodynamical simulations on a moving mesh. *Monthly Notices of the Royal Astronomical Society*, 401(2):791–851, Jan. 2010. doi:10.1111/j.1365-2966.2009.15715.x.

V. Springel. High Performance Computing and Numerical Modelling. *Saas-Fee Advanced Course*, 43: 251, Jan. 2016. doi:10.1007/978-3-662-47890-5_3.

V. Springel, J. Wang, M. Vogelsberger, A. Ludlow, A. Jenkins, A. Helmi, J. F. Navarro, C. S. Frenk, and S. D. M. White. The Aquarius Project: the subhaloes of galactic haloes. MNRAS, 391(4):1685–1711, Dec. 2008. doi:10.1111/j.1365-2966.2008.14066.x.

V. Springel, R. Pakmor, A. Pillepich, R. Weinberger, D. Nelson, L. Hernquist, M. Vogelsberger, S. Genel, P. Torrey, F. Marinacci, and J. Naiman. First results from the IllustrisTNG simulations: matter and galaxy clustering. MNRAS, 475(1):676–698, Mar. 2018. doi:10.1093/mnras/stx3304.

J. Stadel, D. Potter, B. Moore, J. Diemand, P. Madau, M. Zemp, M. Kuhlen, and V. Quilis. Quantifying the heart of darkness with GHALO - a multibillion particle simulation of a galactic halo. MNRAS, 398(1):L21–L25, Sept. 2009. doi:10.1111/j.1745-3933.2009.00699.x.

B. Strömgren. Spectral Classification Through Photoelectric Narrow-Band Photometry. ARA&A, 4:433, Jan. 1966. doi:10.1146/annurev.aa.04.090166.002245.

R. Theler, P. Jablonka, R. Lucchesi, C. Lardo, P. North, M. Irwin, G. Battaglia, V. Hill, E. Tolstoy, K. Venn, A. Helmi, A. Kaufer, F. Primas, and M. Shetrone. The chemical evolution of the dwarf spheroidal galaxy Sextans. A&A, 642:A176, Oct. 2020. doi:10.1051/0004-6361/201937146.

A. Tokiwa, M. Takada, T. Qiu, N. Yasuda, Y. Komiyama, M. Chiba, and K. Hayashi. Study of structural parameters and systemic proper motion of Sextans dwarf spheroidal galaxy with Subaru Hyper Suprime-Cam data. MNRAS, 526(1):1310–1323, Nov. 2023. doi:10.1093/mnras/stad2422.

E. Tolstoy, M. J. Irwin, A. Helmi, G. Battaglia, P. Jablonka, V. Hill, K. A. Venn, M. D. Shetrone, B. Letarte, A. A. Cole, F. Primas, P. Francois, N. Arimoto, K. Sadakane, A. Kaufer, T. Szeifert, and T. Abel. Two Distinct Ancient Components in the Sculptor Dwarf Spheroidal Galaxy: First Results from the Dwarf Abundances and Radial Velocities Team. ApJ, 617(2):L119–L122, Dec. 2004. doi:10.1086/427388.

M. G. Walker and J. Peñarrubia. A Method for Measuring (Slopes of) the Mass Profiles of Dwarf Spheroidal Galaxies. ApJ, 742(1):20, Nov. 2011. doi:10.1088/0004-637X/742/1/20.

M. G. Walker, M. Mateo, E. W. Olszewski, J. K. Pal, B. Sen, and M. Woodroofe. On Kinematic Substructure in the Sextans Dwarf Spheroidal Galaxy. ApJ, 642(1):L41–L44, May 2006. doi:10.1086/504522.

M. G. Walker, M. Mateo, and E. W. Olszewski. Systemic Proper Motions of Milky Way Satellites from Stellar Redshifts: The Carina, Fornax, Sculptor, and Sextans Dwarf Spheroidals. ApJ, 688(2):L75, Dec. 2008. doi:10.1086/595586.

M. G. Walker, M. Mateo, E. W. Olszewski, J. Peñarrubia, N. W. Evans, and G. Gilmore. A Universal Mass Profile for Dwarf Spheroidal Galaxies? ApJ, 704(2):1274–1287, Oct. 2009a. doi:10.1088/0004-637X/704/2/1274.

M. G. Walker, M. Mateo, E. W. Olszewski, B. Sen, and M. Woodroofe. Clean Kinematic Samples in Dwarf Spheroidals: An Algorithm for Evaluating Membership and Estimating Distribution Parameters When Contamination is Present. AJ, 137(2):3109–3138, Feb. 2009b. doi:10.1088/0004-6256/137/2/3109.

R. Weinberger, V. Springel, and R. Pakmor. The arepo public code release. *The Astrophysical Journal Supplement Series*, 248(2):32, jun 2020. doi:10.3847/1538-4365/ab908c. URL https://dx.doi.org/10.3847/1538-4365/ab908c.

A. R. Wetzel, E. J. Tollerud, and D. R. Weisz. Rapid Environmental Quenching of Satellite Dwarf Galaxies in the Local Group. ApJ, 808(1):L27, July 2015. doi:10.1088/2041-8205/808/1/L27.

C. Wheeler, A. B. Pace, J. S. Bullock, M. Boylan-Kolchin, J. Oñorbe, O. D. Elbert, A. Fitts, P. F. Hopkins, and D. Kereš. The no-spin zone: rotation versus dispersion support in observed and simulated dwarf galaxies. MNRAS, 465(2):2420–2431, Feb. 2017. doi:10.1093/mnras/stw2583.

J. Wolf, G. D. Martinez, J. S. Bullock, M. Kaplinghat, M. Geha, R. R. Muñoz, J. D. Simon, and F. F. Avedo. Accurate masses for dispersion-supported galaxies. MNRAS, 406(2):1220–1237, Aug. 2010. doi:10.1111/j.1365-2966.2010.16753.x.

J. Woo, S. Courteau, and A. Dekel. Scaling relations and the fundamental line of the local group dwarf galaxies. MNRAS, 390(4):1453–1469, Nov. 2008. doi:10.1111/j.1365-2966.2008.13770.x.